PROTON EXCHANGE MEMBRANE FUEL CELLS: WATER PERMEATION THROUGH NAFION® MEMBRANES

by

Makoto Adachi
B.Eng., Shinshu University, 2004

THESIS SUBMITTED IN PARTIAL FULFILLMENT OF
THE REQUIREMENTS FOR THE DEGREE OF

DOCTOR OF PHILOSOPHY

In the
Department
of
Chemistry

SIMON FRASER UNIVERSITY

Spring 2010

APPROVAL

Name: **Makoto Adachi**
Degree: **Doctor of Philosophy**
Title of Thesis: **Proton exchange membrane fuel cells: water permeation through Nafion® membranes**

Examining Committee:
Chair: **Dr. E. Plettner (Associate Professor)**

_____
Dr. S. Holdcroft
Senior Supervisor
Professor – Department of Chemistry

_____
Dr. M. H. Eikerling
Supervisor
Associate Professor – Department of Chemistry

_____
Dr. P. C. H. Li
Supervisor
Associate Professor – Department of Chemistry

_____
Dr. H. Z. Yu
Internal Examiner
Professor – Department of Chemistry

_____
Dr. B. A. Peppley
External Examiner
Professor – Department of Chemical Engineering
Queen's University

Date Defended/Approved: March 19, 2010

Declaration of Partial Copyright Licence

ABSTRACT

Water permeation through Nafion® membranes and catalyst-coated membranes are measured. Three types of water permeability measurements are conducted in order to systematically study the effect of the phase of water in contact with the membrane: vapour permeation (termed vapour-vapour permeation), pervaporation (termed liquid-vapour permeation) and hydraulic permeation (termed liquid-liquid permeation). Measurements are taken at 70°C. The largest water permeation flux was observed when the membrane was exposed to liquid water on one side and water vapour at the other, *i.e.*, liquid-vapour permeation. Water permeabilities were found to increase: with increasing differential chemical potential developed across the membrane; with progressive hydration of the membrane; and when the membrane is in contact with liquid water.

Water permeability measurements obtained *ex-situ* are correlated to *in-situ* fuel cell water balance measurements at 70°C. The back permeation (*i.e.*, water transport from cathode to anode), is largely driven by liquid-vapour permeation, and is sufficient to offset the electro-osmotic drag flux (*i.e.*, proton-driven water transport towards the cathode).

Ex-situ and *in-situ* water transport measurements were extended to membranes with thicknesses ranging 6 to 201 μm. Under liquid-liquid permeation condition, water permeation fluxes increased with reduction in

membrane thickness; under liquid-vapour and vapour-vapour permeation conditions, water permeation fluxes increased with reduction in membrane thickness but changed little for thickness below 56 μm.

Estimation of *internal* and *interfacial* water transport resistances revealed that *interfacial* water transport resistance is dominant for thin membranes – explaining why further increases in liquid-vapour and vapour-vapour permeation fluxes are not observed with decreasing membrane thicknesses below 56 μm.

Water permeabilities of catalyst-coated membranes and pristine membranes are found to be similar under all three modes of water permeation. The effect of catalyst layer on membrane water permeation is negligible.

In summary, the formation of a membrane/liquid interface is found to enhance the permeability of water through Nafion® membranes. In contrast, presence of a membrane/vapour interface diminishes the rate of water permeation. Under fuel cell operating conditions, when the membrane/liquid interface is formed at the cathode, it is found that a sufficient rate of back permeation effectively regulates the water balance within the fuel cell.

Keywords: Water permeation, Nafion®, proton exchange membrane fuel cells, water management, water transport

DEDICATION

To the Adachis and the Tamuras

ACKNOWLEDGEMENTS

I would like to thank my senior supervisor Prof. S. Holdcroft for supervision, support, and guidance at Simon Fraser University (SFU). I also extend my thanks and gratitude to my supervisory committee members, Profs. M. Eikerling, P. C. H. Li and J. Clyburne for supervising this thesis research, and to my internal and external examiners, Profs. H. Z. Yu (SFU) and B. Peppley (Queen's University, ON) for thoroughly reviewing this thesis.

My gratitude and appreciation are extended to the following people for their support:

Members of the MEA team and the modelling team of Institute for Fuel Cell Innovation - National Research Council (NRC-IFCI), Drs. T. Navessin, Z. Xie, K. Shi, X. Zhao, J. Peron, T. Astill, M. Rodgers, K. Malek, X. Zhang, M. Secanell, J. Gazzarri, S. Liu, Ms. T. Soboleva, Mr. R. Chow, Mr. P. Le Marquand, Mr. D. Edwards and Mr. J. Roller for support and technical guidance during this joint SFU-NRC collaborative research project.

Prof. W. Mérida and Dr. T. Romero of Clean Energy Research Centre (CERC), University of British Columbia, Prof. B. Frisken and Drs. L. Rubatat and D. Lee of Department of Physics, SFU, for the fruitful discussion and the collaborative research.

Dr. H. Hasegwa, Mr. S. Sekiguchi, Mr. Y. Yamamoto, Dr. J. Miyamoto and the members of AIST – Polymer Electrolyte Fuel Cell Cutting-Edge Research Centre (FC-CUBIC) for giving me the opportunities to work at their institute during my graduate program.

Drs. K. Shinohara, A. Ohma, Mr. S. Tanaka and Mr. T. Mashio of Nissan Motor Co., Ltd. for the meaningful discussion throughout the collaborative research and for supplying the ultra-thin membrane samples used in this thesis research.

SFU machine shop and IFCI design studio for fabricating the water permeation cells.

Drs. K. Shi, R. Neagu, K. Fatih and Mr. M. Dinu for the TEM, SEM images and the help on drawing the schematics of the measurement setups.

Prof. R. Kiyono, Mr. T. Adachi and Dr. A. Siu, who introduced me to fuel cells.

Drs. J. Peron, T. Navessin, T. Peckham, T. Astill, Mr. D. Edwards, and Mr. O. Thomas for proofreading this thesis.

Past and present members of the Holdcroft group and the IFCI-coffee club for their valuable friendship, useful discussions and support throughout my graduate program.

My roommates (Peter, Brad, Coleman, Olivier, Charlot, Tanya) and friends in Vancouver for making my Canadian student-life, GREAT!

My family for supporting me throughout my studies.

Ms. K. Hayashi for her encouragement in completion of this thesis.

SFU, NRC-IFCI, New Energy and Industrial Technology Development Organization (NEDO), and the Ministry of Economy, Trade and Industry (METI) of Japan for financial support.

TABLE OF CONTENTS

LIST OF FIGURES

LIST OF TABLES

LIST OF ABBREVIATIONS

AC	Alternative Current
CCM	Catalyst-Coated Membrane
CL	Catalyst Layer
EIS	Electrochemical Impedance Spectroscopy
EOD	Electro-Osmotic Drag
GDL	Gas Diffusion Layer
$hCCM_d$	Half Catalyst-Coated Membrane, CL placed on the desorption side
$hCCM_s$	Half Catalyst-Coated Membrane, CL placed on the sorption side
HOR	Hydrogen Oxidation Reaction
IEC	Ion Exchange Capacity
LDP	Liquid-Dry Permeation
LLP	Liquid-Liquid Permeation
LVP	Liquid-Vapour Permeation
MEA	Membrane Electrode Assembly
MPL	Micro Porous Layer
OCV	Open Circuit Voltage
ORR	Oxygen Reduction Reaction
PEM	Proton Exchange Membrane
PFSI	Perfluorosulfonated Ionomer
PTFE	Polytetrafluoroethylene
RH	Relative Humidity
r.t.	Room temperature
VDP	Vapour-Dry Permeation
VVP	Vapour-Vapour Permeation

LIST OF SYMBOLS

A	Arrhenius constant / dimensionless
A	Geometrical active area of water permeation / m^2
b_i	Empirical coefficient in Wexler-Hyland equation / dimensionless
c_{H_2O}	Concentration of water in the membrane / mol m^{-3}
$\Delta C_{H_2O}^{internal}$	Apparent water concentration difference within the membrane / mol m^{-3}
$\Delta C_{H_2O}^{interface}$	Apparent water concentration difference at the membrane interface / mol m^{-3}
c_j	Empirical coefficient in Wexler-Hyland equation / dimensionless
$D_{internal}$	Diffusion coefficient of water within the membrane / m^2 s^{-1}
E^0	Standard electrochemical potential / V
E_a	Arrhenius activation energy / kJ mol^{-1}
E^{anode}	Anode potential / V
$E^{cathode}$	Cathode potential / V
E^{cell}	Cell potential / V
E^{OCV}	Cell potential at open circuit voltage / V
EW	Equivalent weight of Nafion® / kg (mol-SO_3H)$^{-1}$
F	Faraday's constant / C mol^{-1}
ΔG	Gibb's free energy / kJ mol^{-1}
I	Total generated current / A
iR-corrected E^{cell}	Ohmic resistance compensated cell potential / V
j	Current density / A cm^{-2}
j_{MAX}	Maximum current density / A cm^{-2}
j_v	Volumetric flow rate of water / m^3 s^{-1}
j_m	Molar flow rate of water / mol s^{-1}
$j_{a\text{-}in}$	Flow rate of water introduced to the cell at anode / mol s^{-1}
$j_{a\text{-}out}$	Flow rate of water exhausted at anode / mol s^{-1}
$j_{c\text{-}in}$	Flow rate of water introduced to the cell at cathode / mol s^{-1}
$j_{c\text{-}out}$	Flow rate of water exhausted at cathode / mol s^{-1}
J_{EOD}	Electro-osmotic drag flux / mol m^{-2} s^{-1}
J_{NET}	*In-situ* net water flux through the MEA / mol m^{-2} s^{-1}
J^a_{NET}	*In-situ* net water flux derived from the anode stream / mol m^{-2} s^{-1}

J^{c}_{NET}	*In-situ* net water flux derived from the cathode stream / mol m^{-2} s^{-1}
J_{H}^{+}	Proton flux through the MEA / mol m^{-2} s^{-1}
J_{LDP}	Liquid-dry permeation flux / mol m^{-2} s^{-1}
J_{LLP}	Liquid-liquid permeation flux / mol m^{-2} s^{-1}
J_{LVP}	Liquid-vapour permeation flux / mol m^{-2} s^{-1}
J_{ORR}	Areal rate of water generation due to ORR / mol m^{-2} s^{-1}
J_{VDP}	Vapour-dry permeation flux / mol m^{-2} s^{-1}
J_{VVP}	Vapour-vapour permeation flux / mol m^{-2} sec^{-1}
J_{WP}	*Ex-situ* and *in-situ* water permeation flux / mol m^{-2} s^{-1}
$k_{background}$	Water evaporation rate of the “background cell” / mol s^{-1}
k_{egress}	Water transport coefficient at the egressing interface of the membrane / mol^2 m^{-2} s^{-1} kJ^{-1}
k_{eff}	Effective water permeation coefficient / mol^2 m^{-2} s^{-1} kJ^{-1}
$k_{ingress}$	Water transport coefficient at the ingressing interface of the membrane / mol^2 m^{-2} s^{-1} kJ^{-1}
$k_{\textit{interface}}$	*Interfacial* water transport coefficient / mol^2 m^{-2} s^{-1} kJ^{-1} or m s^{-1}
$k_{\textit{internal}}$	*Internal* water transport coefficient / mol^2 m^{-1} s^{-1} kJ^{-1}
k^{LLP}	Water permeance under LLP condition / mol^2 m^{-1} s^{-1} kJ^{-1}
M_{ini}	Mass of the cell or the water collecting bottle, before the measurement / g
M_{fin}	Mass of the cell or the water collecting bottle, after the measurement / g
ΔM and ΔM’	Mass change of the cell or the water collecting bottle / g
M_{H_2O}	Molecular weight of water / g mol^{-1}
M_{vp}	Molar concentration of water vapour / mol L^{-1}
n	Number of electrons associated in the reaction / mol
N_d	Electro-osmotic drag coefficient / dimensionless
p_c	Capillary pressure / atm
$p_{sat\text{-}vap}$	Saturated vapour pressure at 343K / atm
p_{STD}	Standard pressure (1 atm) / atm
p_{tot}	Total pressure / atm
p_{vp}	Vapour pressure / atm or hPa
p(z)	Pressure, z / atm
R	Universal gas constant / J K^{-1} mol^{-1} or atm L K^{-1} mol^{-1}
r_c	Capillary radius / m
R_{cell}	Cell resistance / mΩ cm^2
R_{egress}	Water transport resistance at the egressing membrane interface / kJ m^2 s mol^{-2}

$R_{ingress}$	Water transport resistance at the ingressing membrane interface / kJ m^2 s mol^{-2}
$R_{interface}$	*Interface* water transport resistance / kJ m^2 s mol^{-2}
$R_{internal}$	*Internal* water transport resistance / kJ m^2 s mol^{-2}
R_{LLP}	Water transport resistance of LLP / kJ m^2 s mol^{-2}
R_{LVP}	Water transport resistance of LVP / kJ m^2 s mol^{-2}
R_{VVP}	Water transport resistance of VVP / kJ m^2 s mol^{-2}
T	Temperature / K or ^oC
t	Membrane thickness / m
$t(\lambda)$	Membrane thickness at water content λ / m
$t_{wet/dry}$	Wet/dry membrane thickness / m
Δt	Duration of the experiment / s
T_{dp}	Dew point temperature / K or ^oC
T_{STD}	Standard temperature (289K) / K
$T(x)$	Temperature, x / K
$w_{e,max}$	Maximum electrical work / kJ

Greek

β	Net water transport coefficient / dimensionless
γ	Surface tension of water / N m^{-1}
γ_{liq}	Temperature coefficient for determining the chemical potential of liquid water / J mol^{-1} K^{-1}
γ_{vap}	Temperature coefficient for determining the chemical potential of water vapour / J mol^{-1} K^{-1}
δ	Pressure coefficient for determining the chemical potential of liquid water / J mol^{-1} atm^{-1}
θ	Contact angle / ^{o}
λ	Water content of the membrane – number of water molecules per sulfonic site (H_2O/SO_3H) / dimensionless
$\lambda_{average}$	Average water content of the membrane – number of water molecules per sulfonic site (H_2O/SO_3H) / dimensionless
λ_{egress}	Apparent water content of the egressing interface of the membrane during water permeation – number of water molecules per sulfonic site (H_2O/SO_3H) / dimensionless
$\lambda_{ingress}$	Apparent water content of the ingressing interface of the membrane during water permeation – number of water molecules per sulfonic site (H_2O/SO_3H) / dimensionless
$\Delta\mu_{interface}$	Apparent chemical potential drop at the membrane interface / kJ mol^{-1}
$\Delta\mu_{internal}$	Difference in chemical potential within the membrane / kJ mol^{-1}

$\Delta\mu_{LLP\_p(z)}$	Difference in chemical potential between liquid water at 1 atm and liquid water at *z* atm at 343K / kJ mol^{-1}
$\Delta\mu_{LVP\_RH(y)}$	Difference in chemical potential between vapour at relative humidity y% and liquid water at 343K, 1atm / kJ mol^{-1}
$\Delta\mu_{VVP\_RH(y)}$	Difference in chemical potential between vapour at relative humidity y% and 96% RH water vapour at 343K, 1atm / kJ mol^{-1}
μ_{H_2O}	Chemical potential of water / kJ mol^{-1}
μ^0_{liq}	Standard chemical potential of liquid water at 278K, 1 atm / kJ mol^{-1}
$\mu^0_{liq\_T(x)}$	Chemical potential of liquid water at temperature x, 1 atm / kJ mol^{-1}
μ^0_{vap}	Standard chemical potential of water vapour at 278K, 1 atm / kJ mol^{-1}
$\mu^0_{vap\_T(x)}$	Chemical potential of water vapour at temperature x, 1 atm / kJ mol^{-1}
$\mu^0_{vap\_343K}$	Chemical potential of water vapour at infinitely diluted concentration, 343K, 1 atm / kJ mol^{-1}
$\mu^0_{liq\_343K}$	Chemical potential of liquid water at 343K, 1 atm / kJ mol^{-1}
$\mu_{vap\_RH(y)}$	Chemical potential of water vapour at y% RH, 343K, 1 atm / kJ mol^{-1}
$\mu_{liq\_P(z)}$	Chemical potential of liquid water at 343K, z atm / kJ mol^{-1}
v	Flow rate of the carrier gas / mL min^{-1}
ρ	Density of Nafion® membrane / kg m^{-3}

CHAPTER 1 INTRODUCTION

1.1 Proton exchange membrane (PEM) fuel cells

1.1.1 Application of PEMFCs

In the past few decades, increasing concerns regarding growing power demands and global environmental issues have attracted the use of alternative energy conversion devices that are energy efficient, sustainable and environmentally-friendly.

Of these devices, fuel cells are promising candidates that have the capability of replacing conventional energy conversion devices. Similar to batteries, fuel cells convert chemical energy directly into electrical energy.[1,2] One difference to batteries is that fuel cells are open systems; that is, they are capable of continuously producing electrical power as long as the reactants are supplied, whereas in the case of batteries, the total amount of electrical energy produced is determined by the amount of reactant stored in the device. (Figure 1-1) Conventional engine/turbine-generator systems also convert chemical energy to electrical energy. In these systems, energy conversion undergoes two steps: engines and turbines convert chemical energy to mechanical energy via heat, and the generators convert the mechanical energy to produce electrical power. (Figure 1-1) However, the power conversion efficiency of this two-step process is lower than that of fuel cells.

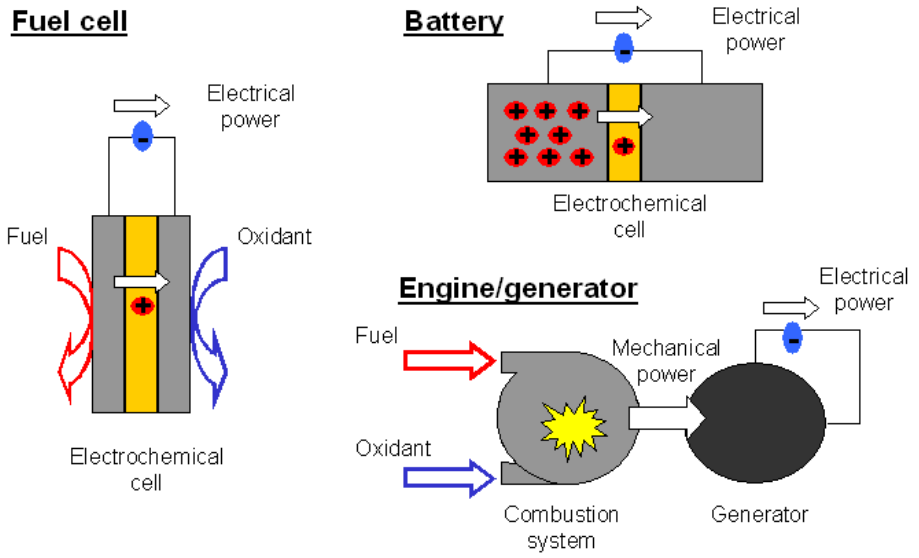

Figure 1-1 Comparison of the energy conversion devices: fuel cell, battery and engine/generator systems.[2]

Fuel cells are also environmentally-friendly: fuel cells generate electrical power while producing zero or near-zero greenhouse gas emissions. These characteristics of fuel cells make them strong candidates to replace the on-demand types of conventional energy conversion technologies. However, it also has to be noted that fuel cells are energy conversion devices. Fuel cells do not attain sustainable overall energy conversion if the fuel is not produced in a sustainable manner. Establishment of the sustainable methods of hydrogen production is one of the challenges that has to be overcome for the commercial adoption of fuel cell technology.[3,4]

There are several types of fuel cells, which can be categorized according to the type of ion-conductor (*i.e.*, electrolyte) used in the device. The most extensively studied fuel cells today are proton exchange membrane fuel cells

(PEMFC), direct alcohol fuel cells (DAFC) and solid oxide fuel cells (SOFC). PEMFCs and SOFCs have proton exchange membranes and oxygen-ion conducting ceramic membranes as the electrolytes, respectively. The construction of DAFC is similar to PEMFC except liquid alcohol is supplied as the fuel. Other fuel cells such as alkaline fuel cells (AFC), phosphoric acid fuel cells (PAFC) and molten carbonate fuel cells (MCFC) have also been studied. In these fuel cells, the electrolytes are: typically liquid potassium hydroxide for AFCs; liquid phosphoric acid for PAFCs; and carbonates of alkali metals (*e.g.*, Na^+, K^+ and Li^+) for MCFCs. The operating temperature range for each type of fuel cells varies in wide range due to differences in the reactivity of the electrochemical reactions and the ionic conductivity of the electrolytes. Types of fuel cells are summarized in Table 1-1.

Table 1-1 Types of electrolytes, conducting ions and the operating temperature ranges of various types of fuel cells.[1,2]

Type of fuel cells	Acronyms	Electrolyte	Ions conducted	Operating temperare range (^oC)
Proton exchange membrane fuel cells	**PEMFC**	Proton exchange membrane	H^+	r.t.* - 180
Direct alcohol fuel cells	**DAFC**	Proton exchange membrane	H^+	r.t.* - 100
Solid oxide fuel cells	**SOFC**	O^{2-}-conducting ceramic membranes	O^{2-}	400 - 1000
Alkaline fuel cells	**AFC**	Base solution (*e.g.*, KOH_{aq})	OH^-	r.t.* - 250
Phosphoric acid fuel cells	**PAFC**	Liquid phosphoric acid	H^+	150 - 220
Molten carbonate fuel cells	**MCFC**	Carbonate of K^+, Na^+, Li^+	CO_3^{2-}	620 - 660

* r.t.: room temperature.

In comparison to other types of fuel cells, PEMFCs have large specific power and the flexibility to scale the power output over a wide range, *i.e.*, few watts to few hundred kilowatts. Thus, PEMFCs are ideally suited for powering a large number of applications, such as cell phones, laptop computers, forklifts, automobiles, and houses.[1,2]

The main challenge of PEMFC commercialization is the reduction of the system cost. With the leading technology today, the cost of a mass-produced (*i.e.*, ≥500,000 systems) PEM fuel cell system is predicted to be ~70 US$/kW, while, as an example, the equivalent for the current automobile internal combustion engine is ~30 US$/kW.[5] Reduction in cost is approached by aspects such as: optimization of operating conditions to improve the specific power of the PEMFC, *i.e.*, water and thermal management; development of enhanced and cost-effective component materials; and reduction of the amount of noble-metal catalyst used.

1.1.2 Electrochemical reactions related to PEMFCs

A PEMFC is an electrochemical cell in which electrical current is generated from a pair of redox reactions: the oxidation of hydrogen at the anode, *i.e.*, hydrogen oxidation reaction, termed HOR; and the reduction of the oxygen at the cathode, *i.e.*, oxygen reduction reaction, termed ORR. (Equation 1-1 and 1-2)

$$H_2 \rightarrow 2H^+ + 2e^- \quad \text{Equation 1-1}$$

$$2H^+ + \frac{1}{2}O_2 + 2e^- \rightarrow H_2O_{(liq)}$$ **Equation 1-2**

The overall reaction (Equation 1-3) generates water and heat, and has a negative Gibb's free energy change (ΔG = -237.3 kJ mol^{-1} at 298K, 1.0 atm).[6]

$$H_2(g) + \frac{1}{2}O_2(g) \rightarrow H_2O(l)$$ **Equation 1-3**

According to thermodynamics principles, a negative differential Gibb's free energy implies the reaction occurs spontaneously, whereas the magnitude of the Gibb's free energy determines the maximum electrical work that can be extracted from the electrochemical cell.[7](Equation 1-4)

$$w_{e,\max} = -\Delta G$$ **Equation 1-4**

Thus, the standard electrochemical potential (E^0) of a fuel cell can be estimated according to the differential Gibb's energy.[7,8](Equation 1-5)

$$E^0 = \frac{-\Delta G}{nF}$$ **Equation 1-5**

where, F and n respectively represent Faraday's constant and number of electrons required (in this case, n = 2) to generate 1 mole of water. The electrochemical potential (E^0) under standard conditions (298K, 1.0 atm) of a hydrogen-oxygen fuel cell is 1.229 V.

The cell potential-current curve, often called the polarization curve, is commonly employed to illustrate the performance of the fuel cell. A typical polarization curve is schematically shown in Figure 1-2. The cell potential (E^{cell}), shown on the y-axis, is the potential difference between the anode and the cathode of an operating fuel cell.

$$E^{cell} = E^{cathode} - E^{anode}$$ .....**Equation 1-6**

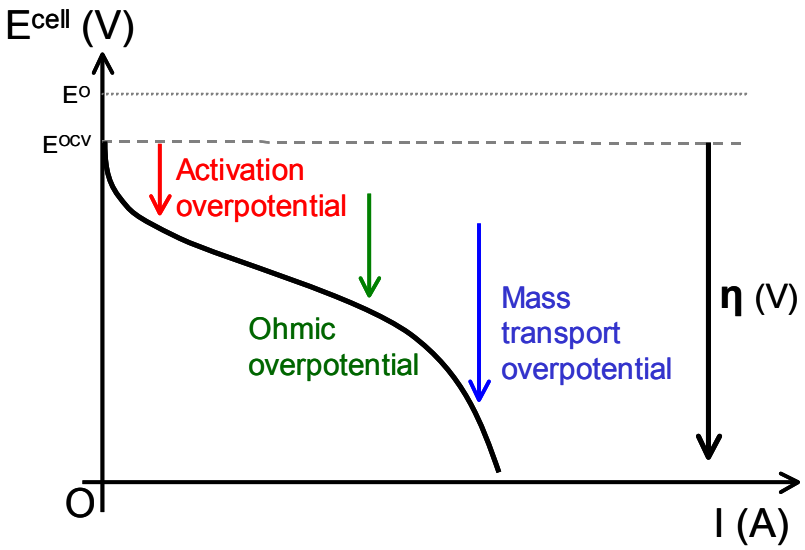

Figure 1-2 Typical polarization curve of a PEMFC. The curve is segmented into three parts according to the different contributors of the loss in E^{cell}.

Generally, E^{cell} is found to be lower than the standard electrochemical potential (E^0). This is attributed to such factors as: deviation from the standard temperature, lower partial pressure of oxygen by using air instead of pure oxygen, and the presence of impurities in the reactants and at the electrode surface.[9] The E^{cell} at zero-current is called the open circuit voltage (E^{OCV}). As shown in Figure 1-2, with increase in electrical current (I), E^{cell} decreases. The difference between the E^{OCV} and E^{cell} during current generation is called the overpotential (η).[8] In PEMFCs, the overpotential can be categorized into three types according to its dominant cause.

a) The steep increase in overpotential in the low current density regime is predominantly due to the activation of the electrochemical reactions. Particularly, ORR is largely responsible for this activation

overpotential. This is evident by comparing the exchange current density of each redox reaction, which describes the intrinsic rates of electron transfer between the electrode and the reactant. The values are ~10^{-10} A cm^{-2} for ORR and ~10^{-3} A cm^{-2} for HOR.[10]

b) The gradual increasing overpotential in the intermediate current density regime is mostly due to the Ohmic resistance of the fuel cell, of which resistance to proton transport through the PEM is the main cause.[9]

c) The steep increase in overpotential in the high current density regime is due to mass transport limitations. Typically, the limiting mass transport species in this regime is oxygen at the cathode reactive sites, due in part to the slow diffusivity of bulk oxygen. (*c.f.,* diffusivity of oxygen in nitrogen and in liquid water are approximately 1/4 and 1/2 that of hydrogen, respectively.)[6]

Overall, the electrical current of PEMFCs thus depends on the rates of HOR, H^+ transport, O_2 transport and ORR. Therefore, efficient fuel cell operation requires enhanced rates of redox reactions and H^+ transport with resultant small overpotentials.

1.2 Membrane electrode assembly

In a modern PEMFC, the anode, cathode and the PEM are bonded together to form the membrane-electrode assembly (MEA), which is the core of the PEMFC. The construction of the MEA is designed in order to obtain a robust

and versatile system with the required performance. The typical seven-layered MEA consists of: a proton exchange membrane; a pair of catalyst layers; a pair of microporous layers; and a pair of gas diffusion layers. The schematic of the MEA is shown in Figure 1-3.

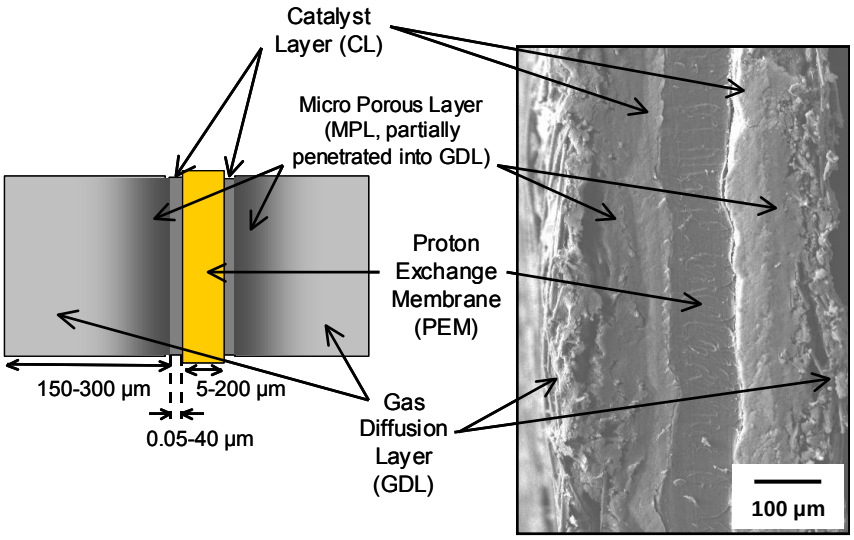

Figure 1-3 Schematic and a SEM image of a seven-layered membrane electrode assembly (MEA).

1.2.1 Single cell assembly and PEMFC stack

A typical single cell consists of a membrane-electrode-assembly (MEA) between a pair of flow-field plates, which consist of electron conducting (*e.g.*, graphite) blocks with engraved channels for gaseous reactants to flow and to serve as the current collector, *i.e.*, flow-field plates. The patterns and architectures of the flow-field plates have been studied for optimal supply of reactants, removal of product water and electrical conduction.[1,2,11] A series of single cells can be combined to form a fuel cell stack as shown in Figure 1-4.

The number of cells and the area of each single cell are adjusted according to the required power output of the PEM fuel cell stack.

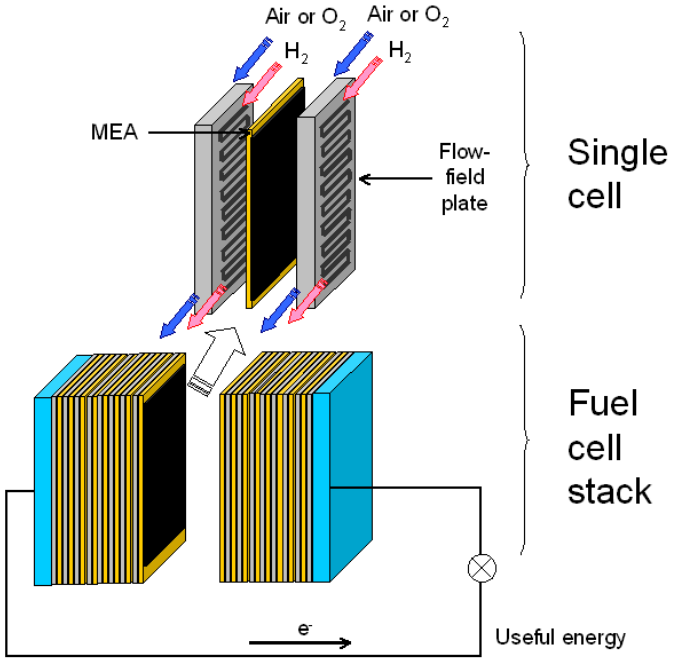

Figure 1-4 Schematic of a single cell and a stack of PEMFC.

1.2.2 Gas diffusion layer (GDL) and microporous layer (MPL)

The outer layers of the MEA are the two gas diffusion layers (GDL). Carbon papers and carbon cloths, prepared from fibrous graphite, are the often-employed materials for gas diffusion layers. The role of the gas diffusion layer is to transport gaseous reactants and electrons effectively to reach the reaction sites. It has become common practice to incorporate a microporous layer (MPL) as part of the gas diffusion layer (*c.f.*,Figure 1-3). A microporous layer is typically prepared from a mixture of high-surface area carbon particles and hydrophobic reagents; the latter is typically an emulsion of polytetrafluoroethylene (PTFE).

The carbon particles conduct electrons, while the hydrophobic reagents are added to bind the carbon particles and to control the water transport properties though the layer (*c.f.*, section 1.3.4.2). The mixture is typically deposited on the carbon paper/cloth to form a layer facing the catalyst layer (CL). Microporous layers create good electric contact between the catalyst layer and the gas diffusion layer, where the average pore-sizes of the two layers differ by 2 to 3 orders in magnitude. The microporous layer also protects the delicate catalyst layers and membranes from the stiff and rigid graphite fibres.

1.2.3 Catalyst layer

The interface where protons, electrons and the reactant gas react has been described as the triple-phase-boundary.[12] Typically, a porous catalyst layer is prepared from an alcohol-water-based catalyst dispersion of proton exchange ionomers and carbon-supported, Pt particles.[13] The ionomer allows proton transport and also acts as a binder for the catalyst layer. The nm-sized particles of Pt are deposited on 10 to 30 nm carbon particles that provide a high surface area (*i.e.*, *primary* particles, surface area to weight ratio: 10^2 – 10^3 m^2 g^{-1}). Agglomeration of these primary particles constitutes the electron-conducting phase of the catalyst layer. A TEM image and a schematic of the catalyst layer are shown in Figure 1-5. To date, several preparation methods of the catalyst layer have been reported.[12,14-18] The methods are developed in order to obtain the maximum number of triple-phase-contacts, percolated phases for electrons and protons to conduct, and void spaces for reactant gas to transport.[19-24]. Due

to their simplicity, spray deposition and screen-printing methods are commonly employed techniques.[15,23,25-29]

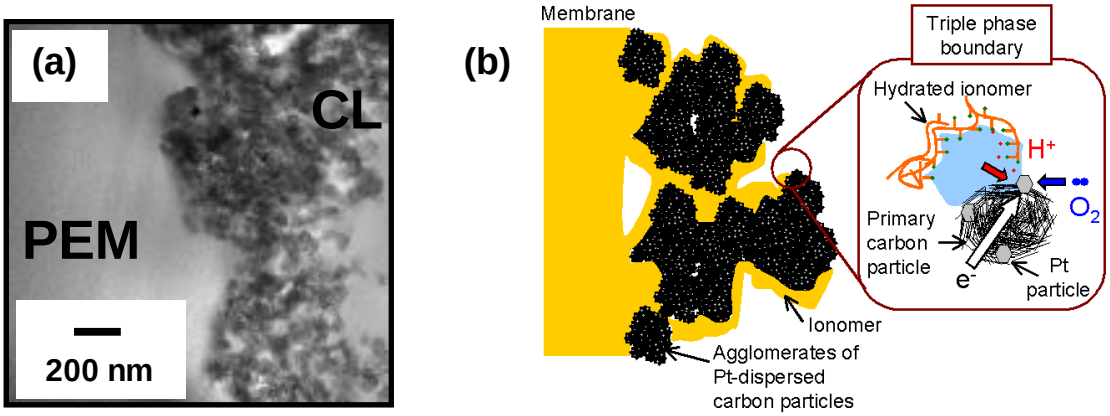

Figure 1-5 (a) TEM image of a PEM/CL interface. (b) Schematic of the PEM/CL interface and the triple-phase-boundary (*e.g.*, cathode).

1.2.4 Nafion® membrane

In the MEA, the proton exchange membrane (PEM) serves both as the electrolyte and the separator for the reactants. Perfluorosulfonated ionomer (PFSI) membranes are commonly employed as the PEM. Within PFSI-based PEMs, DuPont's Nafion® membranes have been the most extensively studied, with more than 20,000 references available in the literature. As shown in Figure 1-6, Nafion® is a copolymer comprising of a hydrophobic polytetrafluoroethylene (PTFE) backbone and pendant perfluorinated vinyl ether side chains, terminated by sulfonic acid groups. The ratio of the hydrophobic backbone to the hydrophilic side chain determines the equivalent weight (EW) of the polymer membrane.[30-32] The EW is defined as grams of dry polymer per mole of sulfonic acid groups (*i.e.*,

units in g/mol-SO_3H). The sulfonic acid groups in the membrane are responsible for the proton conducting and hydration properties of the membrane.[33-36]

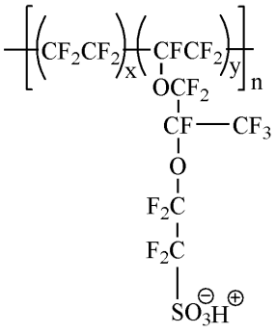

Figure 1-6 Chemical structure of Nafion®. Typically x = 6 - 10 and y = 1.

1.2.5 Nafion® membrane morphology

Due to the opposing properties of the hydrophobic backbone and the hydrophilic sidechain, nano-phase-separation within the Nafion® membrane occurs. As the Nafion® membrane swells in the presence of water, phase-separation evolves in order to minimize the unfavourable interaction between water and the fluorocarbon matrix. Nano-structural evolution has been discussed and investigated extensively in the past decades.[30,37-42] As an example, Gierke et al. investigated the *internal* structure of Nafion® membranes using small-angle x-ray scattering (SAXS) and wide-angle x-ray scattering (WAXS).[30] Numerous SAXS spectra of Nafion® membranes with various counter cations and water contents are presented in their work. A signal in the SAXS spectrum, that corresponds to the nm-range Bragg spacing, was found to increase with the water content of the membrane. According to this observation, they have proposed a spherical ionic cluster model and estimated the mean diameter of the

spherical clusters to be in the range of 2 – 4 nm, depending on the degree of hydration. (Figure 1-7)

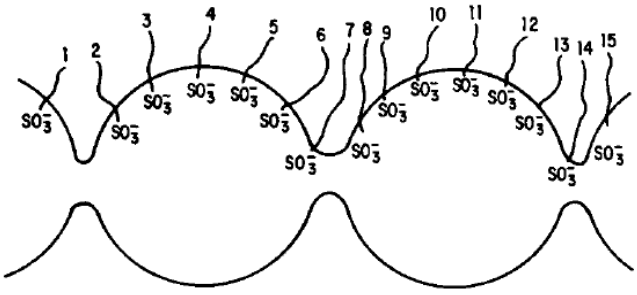

Figure 1-7 Schematic representation of distribution of the ion exchange sites in Nafion®, proposed by Gierke et al.[30] Copyright (1981) with permission from Wiley.

Further study using SAXS and small-angle neutron scattering (SANS) by Gebel et al., revealed detailed changes in morphology during the hydration of Nafion®.[37,43] In addition to Gierke's predicted percolating cluster model at a volume fraction of water of 0.29 (water content ~0.2 g-H_2O/g-dry Nafion®), a further evolution of Nafion® morphology was predicted at higher water/Nafion® ratios. As shown in Figure 1-8, structural inversion is proposed to occur for water volume fractions of ≥0.5, followed by the formation of elongated, rod-like polymer aggregates for higher water contents. Further experimental work by Rubatat et al. confirmed the presence of this elongated rod-like network structure at high water content.[39,41]

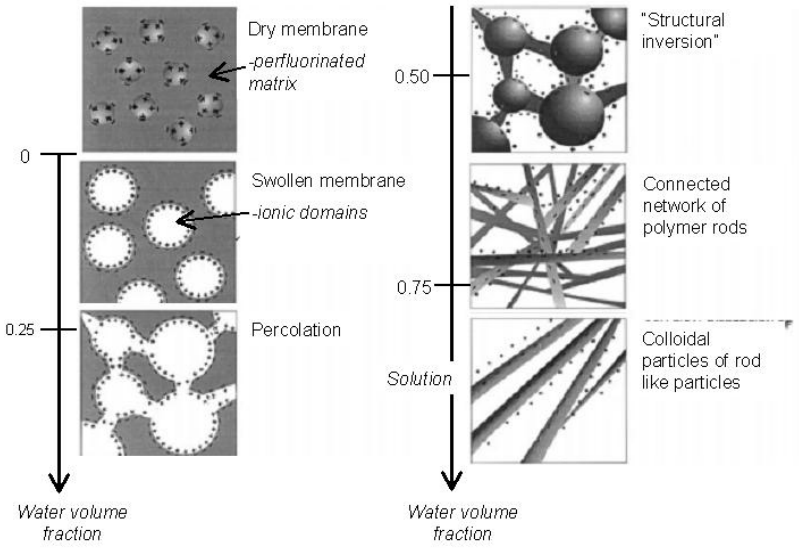

Figure 1-8 Schematic representation of the structural evolution depending on the water content, proposed by Gebel et al.[37] Copyright (2000) with permission from Elsevier.

Schmidt-Rohr and Chen proposed a further development of Gierke's model to explain the small angle scattering results of swollen Nafion® membranes.[42] According to their model, Nafion® consists of parallel, cylindrical nano-channels filled with liquid water. The cylindrical nano-channels are constructed from elongated, rod-like aggregates of Nafion® polymers forming hydrophilic tunnels, as shown in Figure 1-9. Their model described the cylindrical channels as being conserved at any hydration state, and even at ambient temperature, due to the rigidity of the Nafion® "rods".

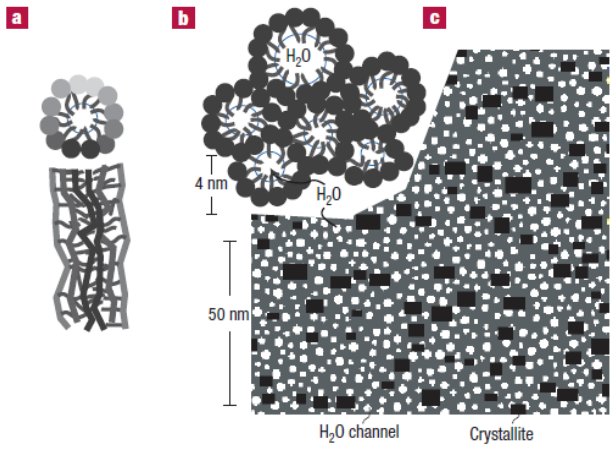

Figure 1-9 Parallel water-channel model of Nafion®, proposed by Schmidt-Rohr et al. (a) Schematic diagram of an inverted-micelle cylinder. (b) The cylinders are approximately packed in hexagonal order. (c) Cross-section image of the Nafion® matrix. The cylindrical water channels are shown in white; the Nafion® crystallites are shown in black; and the non-crystalline Nafion® matrix is shown in dark grey.[42] Copyright (2008) with permission from Elsevier.

Although various models have been proposed to explain the morphology of the swollen Nafion® membranes, no single model has been unanimously recognized as the standard in the field. Nevertheless, the following trends are common to each of the models:[30,37,39,40,42]

i. Hydrophilic/hydrophobic phase-separation is present within the Nafion® membrane.

ii. The hydrophilic phase forms a percolating network at some level of hydration.

iii. The hydrophilic phase, in which water is transported, increases in volume as the membrane swells. Average diameters of these domains are in the order of few nano-meters.

1.3 Water transport in/through the MEA

1.3.1 Proton transport and electro-osmotic drag

During PEMFC operation, protons are transported though the PEM in order to generate electric current. Proton conductivity of a fully hydrated Nafion® membrane is ~0.1 S cm^{-1} between the temperature range of 30 to 80°C.[33,35,36,44,45] However, this conductivity decreases significantly with dehydration of the membrane. As seen in Figure 1-10, the proton conductivity at 30% RH is nearly an order of magnitude smaller than that of the fully hydrated membrane. This change in proton conductivity contributes to the Ohmic loss in the polarization curves of a PEMFC (*c.f.,* Figure 1-2).

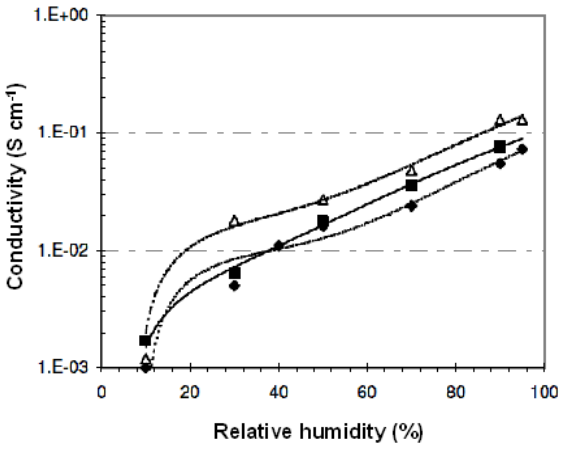

Figure 1-10 In-plane conductivity of Nafion® membranes at 30°C (♦), 50°C (■) and 80°C (△).[35]

The reason for the decrease in conductivity under reduced RH is attributed to the decrease in water content, which consequently decreases the diameter of the hydrophilic pores and the connectivity of the proton conducting channels.[36,46,47] Two mechanisms are known for proton transport in acidic

aqueous environments, as schematically shown in Figure 1-11.[48-51] One is the physical transport mechanism for solvated protons, *i.e.*, vehicular mechanism. Solvated protons are believed to be transported in clusters of water, *e.g.*, hydronium (H_3O^+) and Zundel ions ($H_5O_2^+$). The other transport mechanism is the Grotthuss mechanism, in which the formation and breaking of O-H bonds in water molecules leads to the rapid, net transport of protons through the membrane.[52,53]

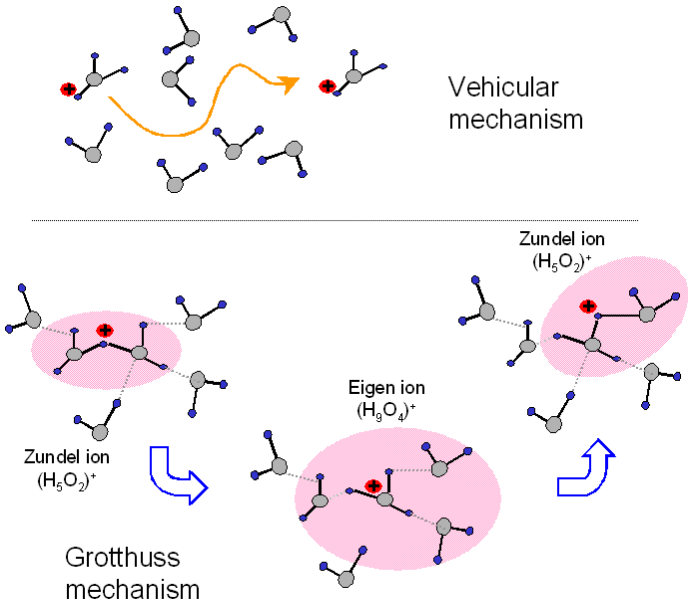

Figure 1-11 Schematic representation of the two proton transport mechanisms, *i.e.*, Vehicular and Grotthuss mechanisms.

Kreuer et al. reported that the chain mechanism for rapid transformation (~10^{-12} s) between the Zundel ion ($H_5O_2^+$) and the Eigen ion ($H_9O_4^+$) is the cause of rapid proton transport in PEM, and thus proton conduction via the Grotthuss mechanism is faster than the vehicular transport of protons.[49] They also reported that the existence of the Grotthuss mechanism in addition to vehicular transport

is required in order to explain the high proton conductivity of Nafion® membranes, since the mobility of protons is reported to be higher than the self-diffusivity of water (transported only via the vehicular mechanism) in hydrated Nafion® membranes.[36]

The transport of water associated with the transport of protons is termed the electro-osmotic drag (EOD).[54-57] The number of water molecules carried per proton is defined as the electro-osmotic drag coefficient (N_d). Various values for the EOD coefficients have been reported for Nafion® membranes.[58-64] As summarized in Table 1-2, EOD coefficients are strongly affected by the hydration state of the Nafion® membrane. In most cases, EOD coefficients are found to increase with the hydration state of the membrane.[58-62,64] However, Aotani et al. reported the reverse trend, *i.e.,* an increase in EOD coefficients with a decrease in membrane hydration level.[63] Since the dominant mechanisms of proton transport and EOD of water in Nafion® membranes are not clearly identified, the precise relationship between the EOD coefficient and the hydration state remains unclear.

Table 1-2 Comparison of the reported electro-osmotic drag coefficient (N_d) for Nafion® membranes.

	T (°C)	Hydration state	N_d (H_2O/H^+)	PEM
Zawodzinski et al.[58]	30	22 (H_2O/SO_3H)	**~2.5**	Nafion® 117
Zawodzinski et al.[58]	30	1 –14 (H_2O/SO_3H)	**~0.9**	Nafion® 117
Fuller and Newman[59]	25	1 –14 (H_2O/SO_3H)	**0.2 - 1.4**	Nafion® 117
Ise et al.[60]	27	11 –20 (H_2O/SO_3H)	**1.5 - 3.4**	Nafion® 117
Xie and Okada[61]	Ambient	22 (H_2O/SO_3H)	**~2.6**	Nafion® 117
Ge et al.[62]	30-80	0.2-0.95 (activity)	**0.3 - 1.0**	Nafion® 117
Ge et al.[62]	30-80	Contact with liquid water	**1.8 - 2.6**	Nafion® 117
Aotani et al.[63]	70	2 – 6 (H_2O/SO_3H)	**2.0 - 1.1**	Nafion® 115
Ye et al.[64]	80	3 – 13 (H_2O/SO_3H)	**~1.0**	Layered Nafion® 115

1.3.2 Water transport within an operating MEA

Water transport to, through, and from, the membrane involves a complex interplay of processes, as illustrated in Figure 1-12. Included in these processes are the rates of transport of water from the anode to the cathode by electro-osmotic drag (J_{EOD}), and the generation of water at the cathode as the product of the oxygen reduction reaction at a rate (J_{ORR}) that increases with current density.

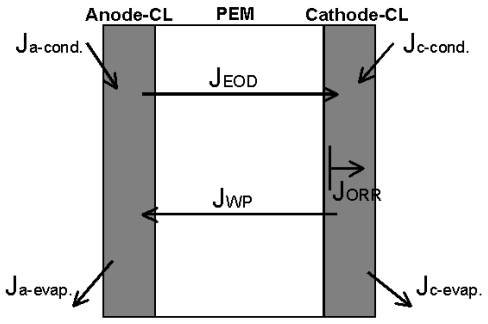

Figure 1-12 Water transport within an operating MEA.

For instance, the rate of water generation at 1 A cm^{-2}, can be calculated from the Faradaic current to be 0.052 mol m^{-2} s^{-1}. The EOD flux (J_{EOD}) at 1 A cm^{-2} with an EOD coefficient of 0.5, for example, the J_{EOD} is estimated to be 0.052 mol m^{-2} s^{-1}. Thus, the overall rate of water transport to and generation at the cathode is calculated to be 0.10 mol m^{-2} s^{-1}. Both these processes lead to an unfavourable, unbalanced distribution of water within the MEA. EOD has the potential to dehydrate the ionomer near, and in, the anode catalyst layer, whereas the accumulation of liquid water in the pores of the cathode impedes oxygen from reaching the reaction sites. The latter is mitigated if the rate of water evaporation at the cathode ($J_{c\text{-}evap.}$) offsets its accumulation, while the effect of the former may be reduced if water is able to permeate from the cathode to the anode (J_{WP}).

A large water permeation flux should also be promoted for the following reasons: (i) a large $J_{c\text{-}evap.}$ may impede the incoming oxygen;[65] and (ii) in practical applications of PEMFCs, the use of humidifiers is undesirable due to the detrimental impact upon the overall space and cost efficiency of the PEMFC system.[1,2] In this scenario, it is logical to make use of the accumulating water at the cathode to hydrate the electrolyte at the anode.[66,67]

During the past decade, a number of water balance experiments have been performed on fuel cells that refer to the direction and the magnitude of the net flux of water, *i.e.*, the sum of J_{WP} and J_{EOD}. The water fluxes obtained from these experiments are useful for discerning the net flux of water under steady state conditions. The next level of sophistication requires deconvolution of the

net water flux to obtain water permeation and EOD fluxes, but this is considerably more difficult.

1.3.3 Theoretical studies of water transport in full MEAs and components

In order to understand and to correlate these individually explored *ex-situ* and *in-situ* experimental studies, numerical modelling of the water transport processes has been undertaken. Concepts underpinning the modelling of heat and mass transport within a fuel cell have been extensively reviewed.[68] Springer et al., in a highly cited piece of work, proposed a model for water transport through a PEM,[69] in which they took the state of hydration of the membrane into account in order to predict the rates of water transport across the PEM. Despite the material properties of the components not being particularly well understood at the time, their empirical and systematic application of physical chemistry principles to fuel cell operation enabled them to construct a simplistic model that has guided many recent studies in this area. Together with other studies, a generalized understanding of water transport processes in an operating fuel cell has emerged, as illustrated in Figure 1-12. Different models are often distinguished in the way they describe each of the water fluxes. Eikerling et al., for example, proposed hydraulic permeation to be a significant factor determining J_{WP},[66] whereas Weber et al. combined hydraulic permeation and diffusive permeation in the J_{WP} term.[70] The nature and magnitude of J_{WP} is clearly an important factor in any realistic model. Thus, a requirement of implementing numerical models to explain and predict actual permeation fluxes is the availability of accurate values of water transport parameters. However, the

extracted experimental parameters are often technique-sensitive and may not always be transferable to the simulation of fuel cell polarization data, thereby leading to inaccurate conclusions.

1.3.4 *Ex-situ* and *in-situ* experimental studies of Nafion® water permeation

1.3.4.1 *Ex-situ* measurement techniques

While the body of work on measurements of net water transport through an operating fuel cell is quite large, relatively few studies have attempted to deconvolute the net water flux into its components (J_{EOD} and J_{WP}), and nor do they provide data to indicate conditions that promote net transport of water to the anode, which may offset the deleterious effects of dehydration of the anode and flooding of the cathode.[71-74]

For this reason, studies on water permeation (J_{WP}) through PEMs are drawing increasing interest as part of a general strategy for mitigating issues associated with water management and improving the performance of PEMFCs.

The permeation of water through a membrane is the transport of water from one side of a membrane to the other.[75,76] The process consists of water sorption, diffusive or convective transport within the membrane, and desorption. Studies of water transport through Nafion® can be categorized as one of three types: (1) measurements of rates of water transport into, within, and from, the membrane; (2) studies of the distribution of water within the membrane; and (3) the molecular mobility of water within the membrane. Information on water transport can be extracted by observing the rate of swelling and deswelling of the

membrane upon exposure to water vapour.[77-81] In these experiments, transient rates of water ingressing or egressing the membrane can be derived. Alternatively, the permeability of a membrane to water can be determined by applying a chemical potential gradient,[25,82-87] induced by a concentration or pressure gradient, and measuring the flux of water. For example, Majsztrik et al. determined the water permeation flux through Nafion® 115 membrane to be 0.03 g min^{-1} cm^{-2} (equivalent to 0.28 mol m^{-2} s^{-1}) under a liquid water/PEM/dry nitrogen flow (0.8 L min^{-1}) at 70°C.[88] From these measurements, information such as permeability of the membranes and activation energy of water permeation can be extracted.

1.3.4.2 *In-situ* measurements

When comparing net water fluxes of fuel cell systems, it is often convenient to normalize the data to obtain the value, β, which is the ratio of the net water flux to proton flux, as defined by Springer and Zawodzinski et al.[69,89,90] When β is positive, the direction of the net water flux is towards the cathode; when negative, it is towards the anode. Zawodzinski et al. were among the first to report β-values, reporting values of 0.2 at current densities of 0.5 A cm^{-2} for MEAs containing Nafion® 117 membrane operated with fully humidified gases.[89] Choi et al. report values in the range of 0.55 – 0.31 with increasing current density values of 0 - 0.4 A cm^{-2} for Nafion® 117-based MEAs under fully humidified conditions.[91] They also report a large increase in β-values under dry operating conditions. Janssen et al. conducted a systematic evaluation of β using Nafion® 105 under combinations of wet, dry and differential pressure.[71]

Negative β-values were observed when the anode was dry, whereas positive β-values were observed for other operating conditions. Ren et al. operated a Nafion® 117-based MEA with oversaturated hydrogen and dry oxygen at 80°C, and observed positive net water fluxes equivalent to β-values between 3.0 and 0.6 in the current density range of 0 – 0.7 A cm^{-2}.[57] Yan et al. observed that β-values increased in value when the cathode humidity decreased while maintaining the anode gases saturated.[72] Negative β-values were recorded when the cathode gases were saturated and the flow rate of the relatively drier hydrogen gas (20% RH) at the anode was increased. They also report on the effect of modifying the relative humidification of the gas streams, applying differential gas pressures, to determine the fluxes of water across MEAs driven by water concentration or pressure gradients in order to deconvolute J_{EOD} and J_{WP} from the net water flux. Murahashi et al. followed a similar approach of investigating β-values for combinations of differential humidity at the electrodes.[92] A general trend of decreasing β-values with an increase in cathode humidity and a positive shift in β-values with increased cell temperature has been reported. Cai et al. conducted a water balance study of Nafion® 112-based MEAs under dry hydrogen and moderately-humidified air, and report that β-values are negative, increasing in magnitude from -0.06 to -0.18 as the current density is increased from 0.1 to 0.6 A cm^{-2}.[73] Liu et al. monitored the variance of β-values along the flow channel using a unique setup that incorporated a gas chromatograph.[74] They operate a rectangular cell with a 30 μm Gore-select membrane in combination with moderately-humidified and dry gases and

observed a significant change in β-values along the gas flow channel. Ye et al. reported the EOD coefficient (N_d) values of ~1.1 for both layered Nafion® and Gore composite membranes. They have also reported their measurements of β-values for MEAs, consisting of Gore's 18 μm-thick composite PEM. They obtained β-values ranged from 0.5 – 0.1, for various humidities of gases (95 – 35% RH) at current densities up to 1.2 A cm^{-2}.[64,64]

Advantages of employing a microporous layer on water management of the MEA have been reported.[93-95] Karan et al. report a correlation between the PTFE content in microporous layers and the retention or removal of water produced during operation.[94] Understanding the characteristics of the microporous layer is one aspect of managing water within the MEA.

More sophisticated techniques reveal detailed information on the in-plane and through-plane distribution of water in an operational fuel cell. A 1-D distribution of water in an operating cell was observed by employing magnetic resonance imaging (MRI)[96-98]. The various degrees of hydration of operational MEA component materials were determined by electrochemical impedance spectroscopy (EIS).[99-101] EIS was also used to report on water distribution across the MEA.[102,103] Gas chromatography was used to observe the in-plane water distribution along the gas flow channel, and estimate the ratio of liquid water, water vapour and reactant gases along the flow channel from the inlet to the outlet.[74,104] Neutron imaging has been used to visualize the in-plane and through-plane water distribution of a PEMFC.[105,107] The pulse-field gradient NMR (PFG-

NMR) has been used to determine the self diffusion coefficient of water within the membrane.[107-110]

1.4 Thesis objectives

Understanding water permeation phenomena through PEMs and analyzing the correlation to other water transport processes within an operating MEA is extremely important in order to predict the water distribution within an operating MEA. Because of the coupling with the electrochemical performance, understanding the water balance is critical to the advancement of PEMFC technology. Although many studies on water permeation through PEMs and overall water balance in an operating PEMFC have been conducted, the correlation between these phenomena has largely been studied using a theoretical approach. A comprehensive experimental study that correlates and validates *ex-situ* and *in-situ* PEM water permeation phenomena has not been reported yet.

In this thesis work, water fluxes in Nafion® membranes and water transport within an operating fuel cell are systematically investigated under comparable *ex-situ* and *in-situ* conditions of temperature, pressure and relative humidity. The correlation between the *ex-situ* and *in-situ* water transport phenomena is studied with the specific objective of revealing the role of back permeation on fuel cell performance. More specifically, influential key parameters for back permeation in the operating fuel cell are identified. The

examined parameters include: the type of driving force, the phases of water at the membrane interfaces, membrane thickness and the presence of catalyst layers at the membrane interfaces. This study is driven by a motivation of obtaining a better fundamental understanding of water transport phenomena in operating PEMFC. Insights would be useful for selectingoperating conditions for improved fuel cell operation. From the view of designing novel PEMs, this knowledge should provide a baseline for the water transport properties of the current standard PEM, Nafion®. Moreover, parameters found could be employed in systematic modelling studies to simulate PEM with varying transport properties.

In order to approach these objectives, several experimental setups and schemes were designed and implemented. Chapter 2 describes *ex-situ* and *in-situ* experimental methods and apparatus used in this work. This description includes the preparation and assembly of membrane samples, five types of *ex-situ* water permeation measurement setups, and experimental setups for *in-situ* fuel cell testing and water balance studies.

In Chapter 3, the correlation between *ex-situ* and *in-situ* water transport properties for a particular Nafion® membrane, NRE211, is analyzed and discussed. Parameters such as the type of driving force and the phases of water at the membrane interfaces are investigated. *In-situ* net water balance measurements on fuel cells and *ex-situ* permeability data are used to determine which *ex-situ* permeation measurement best resembles water transport in an operational PEM for a given set of conditions.

In Chapter 4, *ex-situ* and *in-situ* water transport measurements were extended to Nafion® membranes with different thicknesses. *Ex-situ* water permeability measurements reveal the impact of the membrane thickness under three modes of water permeation conditions. *In-situ* water balance studies confirm the advantages of thin PEMs on regulating the water balance of an operating MEA.

In Chapter 5, the water permeabilities of catalyst-coated Nafion® membranes are studied. The effect of the catalyst layer on membrane water permeation is systematically investigated as in Chapter 3.

Chapter 6 summarizes this thesis' work and proposes future studies based on the findings of this research.

CHAPTER 2 MATERIALS AND EXPERIMENTAL METHODS*

2.1 Overview

Water permeabilities through Nafion® membranes are described by conducting: (a) *ex-situ* water permeation measurements; (b) *in-situ* measurements of water transport through membranes, assembled in an operating fuel cell. Both *ex-situ* and *in-situ* measurements are conducted under comparable temperature and RH conditions, in order to study the correlation between the membrane water permeability and the water transport of an operating MEA. The membrane water permeation measurements were designed to systematically study the effects of the following parameters: (i) type of driving force, (ii) phases of water contact with the membrane, (iii) membrane thickness, and (iv) presence of catalyst layer at the membrane/water interface.

Two types of driving forces were applied to induce the water permeation through membranes: difference in concentration or pressure across the membranes. The magnitudes of driving forces were selected to lie in the range applicable to PEM fuel cell operation. The phases of water in contact with the membrane were considered: viz liquid water and vapour. *Ex-situ* water

*Sections of this work have been published in:
Journal of the Electrochemical Society, M. Adachi, T. Navessin, Z. Xie, B. Frisken
Journal of the Electrochemical Society, M. Adachi, T. Navessin, Z. Xie, B. Frisken
and S. Holdcroft, 156, 6 (2009)

permeability measurements were conducted at 70°C, which is comparable to the practical operation of PEMFCs; which are 60 - 80°C.[1,2,111-113] *In-situ* water transport within the fuel cell was measured by operating a 25 cm^2 single cell at 70°C, with hydrogen and air. The RH and pressures of the supplied gases were manipulated to systematically study their correlation to the membrane water permeability obtained *ex-situ* and to the resulting fuel cell performance.

2.1.1 Membrane samples

Seven Nafion® membranes were prepared for *ex-situ* and *in-situ* water transport measurements. The thickness and the equivalent weight (EW) of the membranes are summarized in Table 2-1. Nafion® membranes (NRE211, N112, N115 and N117) were purchased from DuPont. The purchased membranes were prepared as follows: three membranes, N112, N115 and N117 were extruded; NRE211 was cast from a Nafion® dispersion.[31,32] NRE211 is the standard membrane for modern PEMFC studies, thus it was used to establish the *ex-situ* and *in-situ* measurement methods described in Chapter 3. A series of ultra-thin membranes (6 – 11 μm-thick, dispersion-cast membranes) were provided by Nissan Motor Co., Ltd. The membranes were prepared by casting Nafion® ionomer dispersion (DE2021CS, DuPont) on a PET film, dried at 80°C for 2 hr and annealed at 120°C for 10 min. The dependence of water permeation on membrane thickness is studied in Chapter 4.

Table 2-1 Thickness and equivalent weight (EW) of Nafion® membranes.

	Product name	Dry thickness / μm	Wet thickness / μm	EW / g mol-$_{SO_3H}^{-1}$
Dispersion -cast membranes	Provided by Nissan Motor Co., Ltd.	5	6 ± 1	1100
		10	11 ± 1	1100
		25	28 ± 2	1100
	NRE211	25	28 ± 2	990 - 1090
Extruded membranes	N112	51	56 ± 4	1100
	N115	127	140 ± 10	1100
	N117	184	201 ± 13	1100

2.2 Sample preparation

2.2.1 Pretreatment of Nafion® membranes

Nafion® membranes were pre-treated in the following manner - boiled at 80^{o}C in 3 wt% peroxide solution for 2 h, boiled at 80^{o}C in 1 M sulphuric acid solution for 2 h, rinsed in de-ionized Milli-Q water (Millipore) at r.t., and stored in de-ionized water for 24 h prior to use. All membranes were used in their H^{+}-form.

2.2.2 Preparation of catalyst-coated membranes (CCM)

CCMs: Carbon-supported Pt (46.5 wt% Pt, TEC10E50E, Tanaka Kikinzoku Kogyo) was dispersed in 50 wt% methanol in water by sonication for 30 min. 5 wt% Nafion® ionomer solution (DE2020CS, DuPont) was added to provide 30 wt% Nafion® content based on the solids content, and the mixture was homogenized by sonication for a further 1 h. This catalyst ink was spray-deposited using an automated spray coater (EFD, Nordson Company) on one side or both sides of the membrane, mounted on a vacuum table. The vacuum table was heated up to 95^{o}C to dry the catalyst layer between each pass of

spray-deposition. The deposition was controlled to yield 0.35 - 0.40 mg cm^{-2} Pt on each side of the membrane.[15,25] *Note*: membranes annealed for 6 hr at 95^{o}C on a vacuum table prior to use were found to exhibit identical hydration and permeability characteristics of as-received membranes.

In Chapter 3 and Chapter 4, the catalyst-coated membranes were assembled into MEAs and *in-situ* water balance measurements were conducted (*c.f.,* section 2.2.3). Water permeation through catalyst-coated membranes is studied and described in Chapter 5. Water permeabilities are examined through pristine membranes (PEM); half catalyst-coated membranes, for which CL is deposited on the sorption side ($hCCM_s$); half catalyst-coated membranes, for which CL is deposited on the desorption side ($hCCM_d$); and catalyst coated membranes (CCM) with a CL on both sides.

2.2.3 Membrane electrode assemblies (MEA)

Sheets of two-layer gas diffusion layer (GDL) possessing a microporous layer (MPL) (SIGRACET 24BC, SGL Carbon group) were used to sandwich the CCMs for all MEAs used. The GDL/CCM/GDL was assembled into a 25 cm^2 triple serpentine flow field design cell (Fuel Cell Technologies) without hot-pressing. Compressible silicone gaskets, 125 μm thick, were used on both sides of the MEA to seal the reactant gases and to provide uniform compression, which was confirmed using pressure sensitive paper (Pressurex, super-low, Sensor Products Inc.).

2.3 *Ex-situ* measurement of water permeation through Nafion® membranes

2.3.1 Measurement of vapour-vapour permeation (VVP) and liquid-vapour permeation (LVP)

Membranes were sandwiched between two polyethylene (PE) sheets with thermal adhesives (HeatSeal, 1.5 mil, GBC). The PE sheets had a punched hole through which the membrane was exposed. The exposed area was, 34.9 – 37.1 cm^2, except for the measurements of ultra-thin membranes (*i.e.*, 6 - 28 μm), which was 25.0 cm^2. The PE sheets sealed the perimeter of the membrane in order to allow water permeation to occur only through the punched hole. In the case of VVP experiments, the PE/membrane/PE assembly was placed in a leak-free sample holder, as illustrated in Figure 2-1(a), and docked to a polypropylene container filled with water. The container was placed in an environmental chamber so that the RH of the head space between the water and membrane was at a saturated point, whereas the RH above the membrane was controlled by the environmental chamber in an isothermal environment. For measurements of LVP, a PE/membrane/PE assembly was floated on the surface of the water in a stainless steel container and placed in the environmental chamber, so that one side of the membrane was exposed to liquid water, while the other side was exposed to a RH controlled by the environmental chamber, as illustrated in Figure 2-1(b). All measurements were performed at 70^oC.

An Espec Model SH-241 environmental chamber was used for VVP and LVP measurements. The temperature and humidity of this chamber were measured with a calibrated dew point meter (HMT337, Vaisala Inc.) to confirm its

humidity controlling capability. The temperature was controlled to ±0.5^{o}C according to a calibrated K-type thermocouple and digital thermometer (Omega). Initial LVP and VVP experiments revealed that the water in the container cooled during water permeation due to the endothermicity of water evaporation. In the case of VVP measurements, the temperature of the liquid water dropped by ~ 1^{o}C from its initial set temperature of 70^{o}C, which lowered the RH in the head-space between the water and the membrane to ~96% RH from 100%. Since 1^{o}C is similar in magnitude to the error of the digital thermocouple, rather than attempting to maintain the VVP cell at the required temperature through external heating, the 1^{o}C difference was accounted for in the calculated chemical potential gradients as discussed later. In the case of LVP measurements, where rates of water permeation were found to be much greater, and consequently rates of evaporation were much greater, the temperature of the liquid water dropped by up to ten degrees from its initial temperature of 70^{o}C, which significantly affected the measured rates of water permeation. Hence, the stainless steel container was externally heated to maintain a constant temperature of 70^{o}C using a 100 W flexible heater (Watlow electric Mfg. Co), thermocouple (K-type TC, Omega Engineering Inc.) and external temperature controller (Model 210, J-KEM Scientific Inc.).

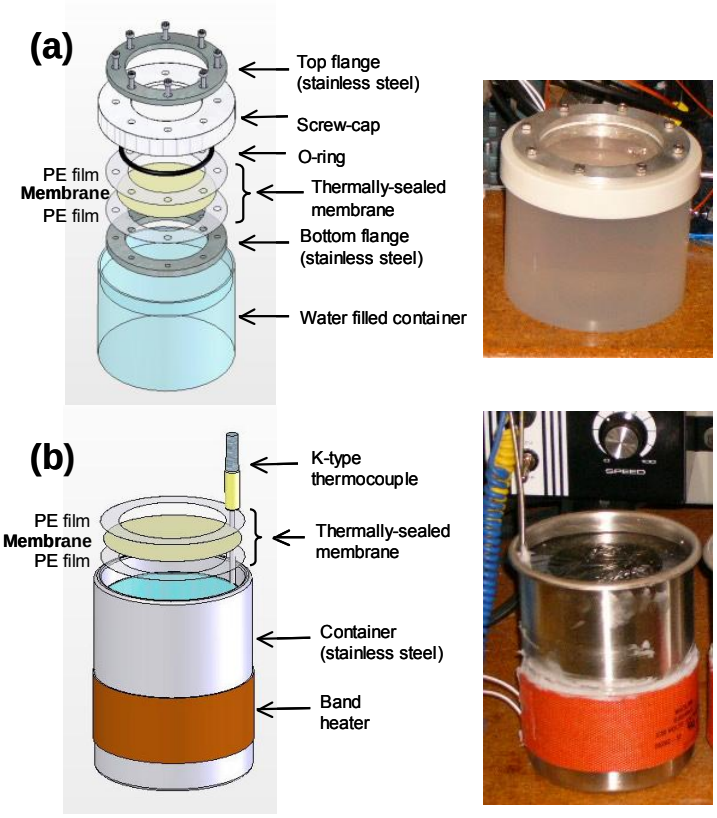

Figure 2-1 Schematic and photographs of the (a) vapour-vapour permeation (VVP) and (b) liquid-vapour permeation (LVP) cells.

As Majsztrik et al. and Romero at al. and others[84,86,87,114,115] have observed, the flow velocity of the carrier gas on the evaporation side of the membrane influences the rate of water permeation in both VVP and LVP measurements because the local concentration of water at the membrane/gas interface varies with flow velocity. In the present experimental setup, the convection fan in the environmental chamber was used to generate a constant gas flow of humidified air on the evaporation side of the membrane. The magnitude of this flow velocity at the membrane/gas interface was investigated by measuring the evaporation rate of water from the container. The obtained

data was then compared to the study by Hisatake et al. on the rate of water evaporation versus the convective flow velocity at the surface from which evaporation is taking place.[116,117] From this investigation, the gas flow velocities at the membrane surface in the setup used in this work were estimated to lie between 1.5 - 3.2 m s^{-1}, depending on where the container was placed in the environmental chamber. These values are much larger than those reported to be required to achieve gas flow-independent rates of water permeation.[84,86,87,115] For example, Majsztrik et al. observed maximum rates of water permeation when the flow velocity of the dry nitrogen gas at 70^{o}C is > ~0.17 m s^{-1} and at 0.37 m s^{-1} for vapour/N115/dry gas and liquid/N115/dry gas configurations, respectively.[115] Romero et al. reported helium gas flow velocities of > 0.008 m s^{-1} and > 0.025 m s^{-1} for flow-independent water permeation through vapour and liquid equilibrated N115 membranes at 70^{o}C.[87] Ge et al. observe the maximum flow-independent water permeation through a N112-based MEA to occur for nitrogen gas flow velocities of 0.13 m s^{-1} and 0.81 m s^{-1} for vapour/MEA/dry gas and liquid/MEA/dry gas configurations, respectively, at 80^{o}C.[84] Thus, the flow velocity at the evaporation interface of the membrane in the VVP and LVP setups used in this work are sufficiently high to observe the maximum flow-independent water transport rates, leading to the important assertion that water permeation is insensitive to variations in convective velocities that may be present in the environmental chamber.

For VVP and LVP measurements, the container with water and the PE/membrane/PE assembly was removed from the environmental chamber at

regular intervals and weighed. The initial mass of the container was determined after the temperature of the container was stabilized at 70^{o}C, which was typically 2 hours. The mass of the container was measured in a typical interval of 2 – 6 h for both VVP and LVP measurements. Rates of VVP and LVP are calculated as water fluxes through the membrane (J_{VVP} and J_{LVP}, respectively). For LVP measurements, the rate of evaporation from a water-filled container, which an identically-sized PE film without the punched hole and the membrane was floated, was measured. This was carried out in order to determine errors induced by direct evaporation of water from the small gap between the perimeter of the PE film and the wall of the container. This background rate of evaporation (0.13 – 0.03 mmol s^{-1} per container, depending on the RH) is <20 – 23% of the rate or permeation through the membrane and was subtracted from the measured weight loss of the container. For VVP measurements, the leak rate from the membrane holder and the polypropylene container was ~2.1x 10^{-4} mmol s^{-1} (<0.5% of the total rate of water permeation) at 70^{o}C and 40% RH condition, which can be considered negligible.

Water fluxes for VVP and LVP (J_{VVP}, J_{LVP}) are expressed below where $\Delta M/\Delta t$ represents the evaporation rate of water and M_{H2O} and A as the molar mass of water and the exposed area of the membrane.

$$J_{VVP} = \frac{\left(\frac{\Delta M}{M_{H_2O}\Delta t}\right)_{PEM}}{A} \quad \text{.....Equation 2-1}$$

$$J_{LVP} = \frac{\left(\frac{\Delta M}{M_{H_2O}\Delta t}\right)_{PEM} - \left(\frac{\Delta M}{M_{H_2O}\Delta t}\right)_{background}}{A} \quad \text{Equation 2-2}$$

VVP and LVP fluxes were determined from four series of measurements taken from two different pieces of membranes. Errors are defined as the standard deviation. The stability and reproducibility of this setup was found to be satisfactory. For example, the variation of the measured rates of water permeation through a NRE211 membrane for the largest RH differential (40% RH at 70^{o}C) was accurate to ±0.00051 mol m^{-2} s^{-1} for VVP measurements, corresponding to a ±5% variance with respect to the average value and ± 0.0079 mol m^{-2} s^{-1} (±6% range) for LVP. Sample data are shown in Appendix B.

2.3.2 Measurement of liquid-liquid permeation (LLP)

Water permeation through the membrane driven by a hydraulic pressure gradient was measured using the setup illustrated in Figure 2-2. A syringe (Gastight #1025, Hamilton Co. with PHD2000, Havard Apparatus) filled with deionized water, a mass flow meter (2.0 µL min^{-1} and 20 µL min^{-1}, µ-FLOW, Bronkhorst HI-TEC) and a pressure transducer (PX302-100GV, Omega Engineering Inc.) were connected in series with 1/8" OD PTFE tubing. The membrane was installed in a cell made in-house, consisting of a PTFE coated stainless steel screen to prevent rupture of the membrane and an O-ring. Measurements were typically conducted on a membrane area of 4.13 cm^2 except for 6 and 11 µm membranes, for which the area was reduced to 0.291 cm^2 and 0.193 cm^2, respectively, in order to avoid exceeding the maximum water flow rate

of the mass flow meter (*i.e.*, 20 µL min^{-1}). The cell was heated on a mantle and maintained at 70°C. A constant flow of water throughout the system was maintained until the desired temperature and pressure was reached. Measurements were taken when the upstream pressure indicated by the pressure transducer deviated by <1%. This was repeated at least 10 times in the pressure range of 0 - 1.2 atm. The apparatus was controlled and monitored using Labview software. Sample data are shown in Appendix B.

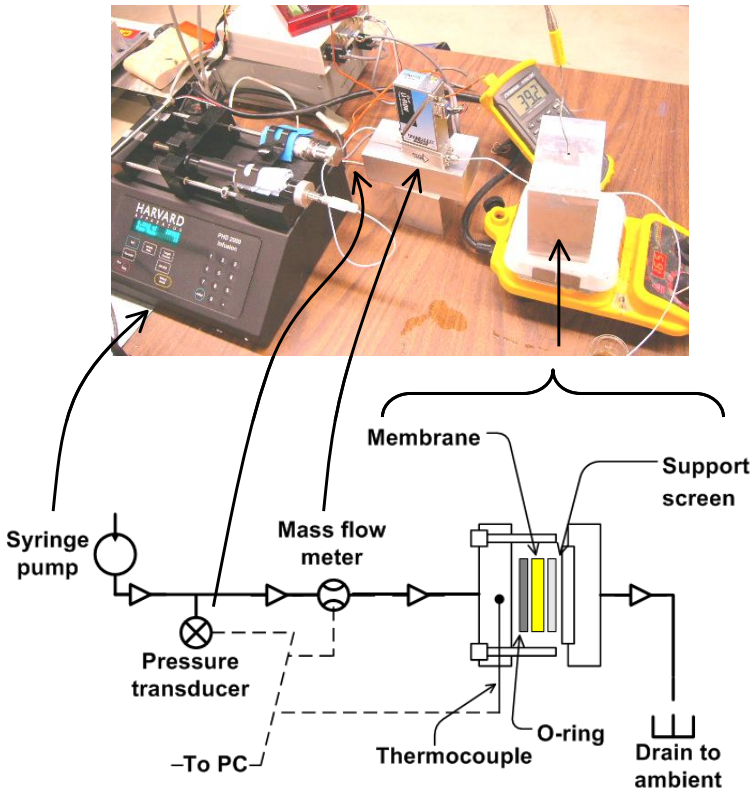

Figure 2-2 Photograph and schematic of the liquid-liquid permeation (LLP) setup. Syringe, mass flow meter, and the pressure transducer were placed in an isothermal environment of 20°C. The cell was heated independently to the rest of the setup.

2.3.3 Measurement of vapour-dry permeation (VDP) and liquid-dry permeation (LDP)

Vapour-dry permeation (VDP) and liquid-dry permeation (LDP) measurements were conducted exclusively to study the effect of catalyst layer on water permeation, discussed in Chapter 5.

The setups illustrated in Figure 2-3(a) and (b) were used for VDP and LDP measurements. Cylindrical chambers with volumes ~125 cm^3 were separated by a 2 cm^2 membrane. Hot water was circulated through double-walled stainless steel chambers to control the cell temperature. K-type thermocouples (Omega) and pressure transducers (Omega, 0 - 15 psig) were used to monitor temperature and pressure within the chambers. Dry helium gas was supplied to one chamber (dry side with the dew point sensor) as the carrier gas for the egressing water. The exhausts of both chambers were at ambient pressure. Two mass flow controllers (Alicat, 0 - 500 SCCM) were connected in parallel to supply up to 1000 mL min^{-1} (1000 SCCM) of dry gas.

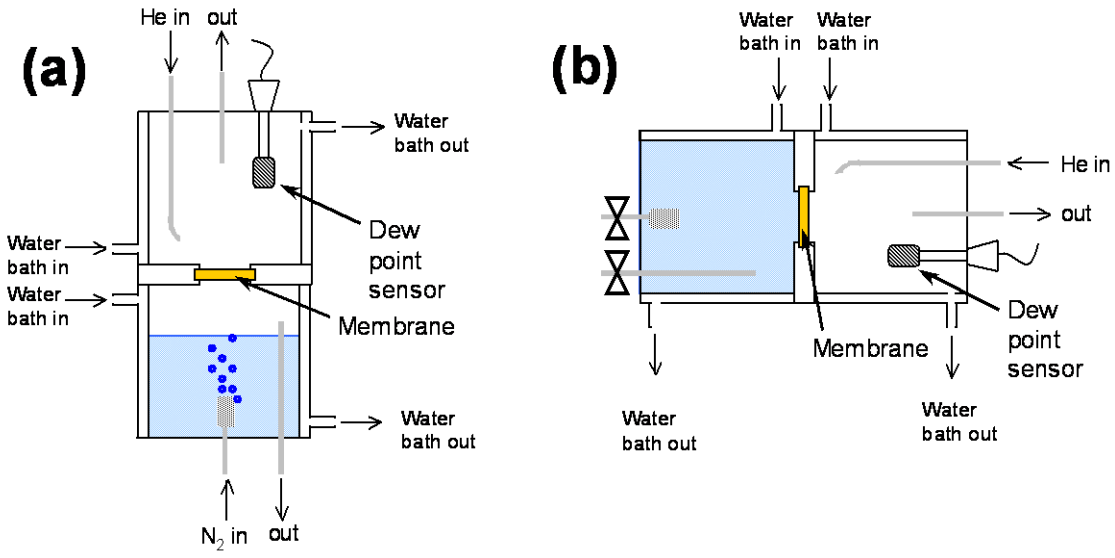

Figure 2-3 Schematics of the: (a) vapour-dry permeation (VDP) and (b) liquid-dry permeation (LDP) apparatuses.

For VDP measurements, 25 mL min^{-1} of dry nitrogen gas was bubbled through one of the chambers (wet side), which was half-filled with liquid water at 70°C. This ensured a homogeneous distribution of saturated water vapour at the "wet side" of the chamber. The flow rate of dry gas was varied while the dew point of the "dry side" of the chamber was monitored. The dew point meter was thermally controlled to prevent condensation within the probe (Vaisala, HMT 330). The flow rate of the dry carrier gas was increased in the sequence 30, 50, 100, 300 500, 700 and 1000 mL min^{-1}.[87]

Based on Wexler and Hyland's work,[118] the empirical constants and equations provided on the specification sheets[119] for the dew point meter (Vaisala), were used to estimate the vapour pressure of water at the "dry side".

$$\ln p_{vp} = \sum_{i=-1}^{3} b_i \Theta^i + b_4 \ln \Theta \quad \text{.....Equation 2-3}$$

where, p_{vp} (in hPa, explicitly for Equation 2-3) and b_i represent the vapour pressure of water and empirical constants, respectively. Θ is described as:

$$\Theta = T_{dp} - \sum_{j=0}^{3} c_j T_{dp}^{\ j} \quad \text{Equation 2-4}$$

where, T_{dp} (^oC) and c_j represent the dew point temperature and the empirical constants. The sets of constants are listed in Table 2-2.

Table 2-2 Empirical constants used for Equation 2-3 and Equation 2-4.[119]

c_0	0.493	b_{-1}	-0.580×10^{4}
c_1	-0.461×10^{-2}	b_0	0.139×10^{1}
c_2	0.137×10^{-4}	b_1	-0.486×10^{-1}
c_3	-0.127×10^{-7}	b_2	0.418×10^{-4}
		b_3	-0.145×10^{-7}
		b_4	6.55

The calculated vapour pressure was then used to calculate the molar concentration of water vapour in the gas stream using the ideal gas equation (*c.f.*, Equation 2-5).

$$M_{vp} = \frac{p_{vp}}{RT} \quad \text{Equation 2-5}$$

where, M_{vp}, p_{vp}, R and T are the molar concentration of water vapour (mol L^{-1}), vapour pressure of water (converted to atm), universal gas constant (0.082 L atm K^{-1} mol^{-1}), and temperature (K).

The gas supplied to the “dry side” of the chamber is assumed to contain a negligible amount of water, thus any water vapour exhausted from the cell is due to the amount permeated. The permeation flux is calculated from the molar concentration of water vapour at the outlet according to Equation 2-6.

$$J_{VDP} = \frac{M_{vp} v}{A(p_{tot} - p_{vp})} \quad \text{Equation 2-6}$$

where, J_{VDP}, v and A represent the VDP flux (mol m^{-2} s^{-1}), flow rate (L s^{-1}) of the carrier gas and the area of the membrane sample (2 cm^2). (p_{tot} - p_{vp}) represents the partial pressure of helium (where p_{tot} = 1.0 atm), which takes into account of the volume increase of the gas due to humidification.

For the LDP measurement, the apparatus is shown in Figure 2-3(b). The "wet side" of the chamber was filled with liquid water so that the membrane is contact with heated liquid water. The dew point of the "dry side" was monitored while the flow rate of the dry gas was varied in the same manner as for VDP. The LDP water flux through the membrane was calculated according to Equation 2-7:

$$J_{LDP} = \frac{p_{vp} v}{RTA(p_{tot} - p_{vp})} = \frac{M_{vp} v}{A(p_{tot} - p_{vp})} \quad \text{Equation 2-7}$$

Sample data are shown in Appendix B.

Similar to VVP and LVP, VDP and LDP are also types of water transport measurements under a concentration gradient for membranes, which are equilibrated with vapour and liquid, respectively. The differences between these two types of measurements are the range of differential concentration applied across the membrane. During VVP and LVP measurements, RH of the gas, downstream from water permeation were controlled by the environment chamber and limited in the relatively high range (38 to 84% RH); whereas, in the case of VDP and LDP the RH of the gas downstream from water permeation was relatively low compared to the cases of LVP and VVP since the supplied carrier

gas was dry. In the case of VDP and LDP, the water that permeated through the membrane, humidifies the dry gas, which determines the differential concentration of water across the membrane. During VDP and LDP measurements, the RH downstream from the membrane was found to vary in the range of 0 - 27%RH and 0 - 64%RH, respectively. Thus, in most part, a larger differential concentration of water is present across the membrane during VDP and LDP measurements compared to VVP and LVP, respectively. This is noted since not only the magnitude of concentration gradient but also the hydration state of Nafion® membranes are known to impact the water fluxes.[69,89] Another methodological differences between VDP/LDP measurements and VVP/LVP measurements are the way of quantifying the water permeation flux. The dew point temperature of the effluent dry gas determined the VDP and LDP fluxes; whereas the mass lost due to water evaporation was measured over time to determine the VVP and LVP fluxes. An advantage of the VDP and LDP measurement is the rapid data acquisition. In contrast, a drawback is the magnitude of experimental error (*i.e.*, ~15% and ~25%, respectively), which was found to be larger than that of measurements by LVP and VVP (*i.e.*, ~5% and ~6%, respectively).

2.4 *In-situ* measurement of water transport through the MEA

2.4.1 Fuel cell test station

A fuel cell test station (850C, Scribner Associates) was used to control and supply gases to the 25 cm^2 triple serpentine flow design, single cell (Fuel Cell Technologies). An integrated load bank was used to control the electrical

load of the test cell. The data was acquired by the Fuel Cell software (Scribner Assoc.). The test cell, gas inlets and outlets were thermally controlled to avoid temperature fluctuations, overheating of the cell, water condensation, and excess evaporation of water in the system. The relative humidity of the supplied gases was controlled by the set dew point of the humidifiers of the test station. Values of vapour pressure used to calculate the relative humidity were taken from the literature.[6] The inlet gas tubing was heated 5^{o}C above the set cell temperature to avoid water condensation. The cell temperature was maintained at 70^{o}C. Water-cooled condensers (~0.6 m long for the anode and ~1 m long for the cathode) were installed at the exhaust manifolds of the cell to collect the water as condensed liquid. The gas temperatures at the outlets of the water collecting bottles were found to be < 21^{o}C, which implies the gases that leave the bottles contains some moisture. This amount of water (< 8% of the initially introduced humidity at 70^{o}C.) is accounted for the prior calibration of gas humidity. The setup is shown in Figure 2-4.

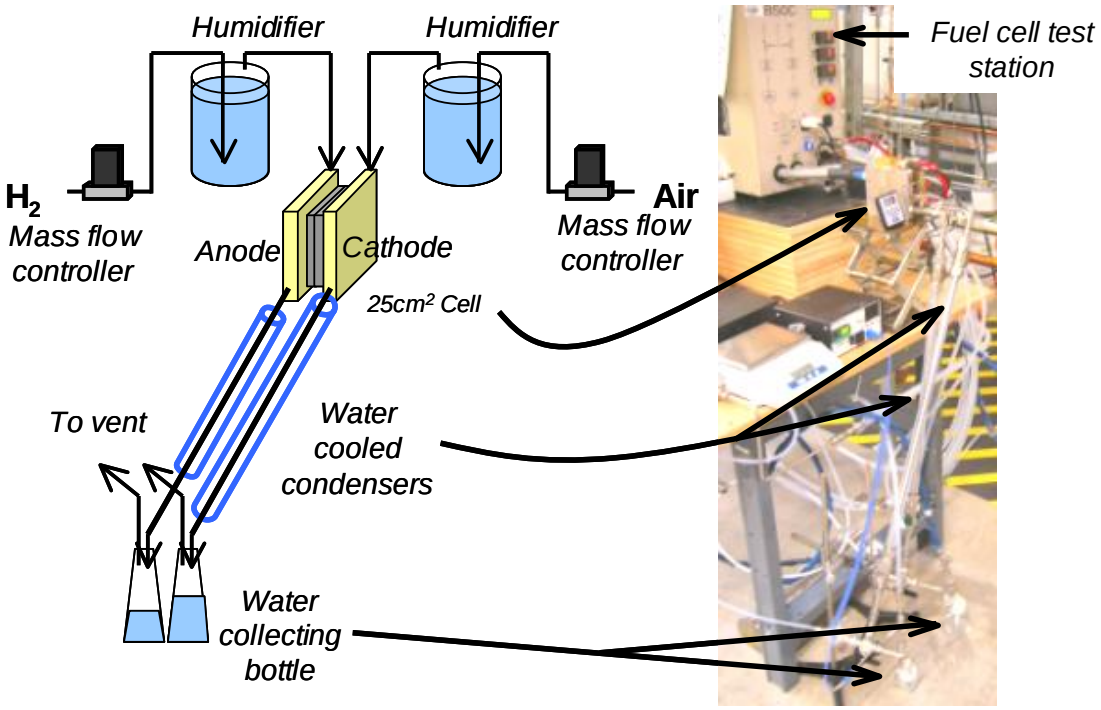

Figure 2-4 Schematic and a photograph of fuel cell testing setup. Water-cooled condensers and water collecting bottle were installed for *in-situ* net water transport measurement.

2.4.2 Conditioning of the MEA

To obtain reproducible and comparable water balances, a strict procedure of fuel cell testing was followed, which included precise and reproducible cell assembly, MEA conditioning, and water collection.

The humidifiers and gas tubing were heated to the set temperatures before gas was supplied to the cell. Fully humidified hydrogen and air were supplied to the cell when the cell temperature stabilized at 70°C. When the open circuit voltage (OCV) of 0.95 V was reached, 0.4 - 1.0 A cm^{-2} was applied to maintain a cell potential of 0.5 - 0.7 V. The flow rate of the hydrogen and air were supplied stoichiometrically, so that the molar ratio between the supplied

reactant and the required amount to generate a given current was constant. For instance, 0.007 L min^{-1} and 0.017 L min^{-1} of pure hydrogen and air corresponded to the constant generation of 1 A from the cell under standard conditions (273K, 1.0 atm). In this experiment, fuel gas (hydrogen) and oxidant gas (air) were supplied in the stoichiometric ratio of 2.0 and 3.0, respectively. However, severe reactant starvation may occur under low current density operation due to the low flow rate of the reactant gases supplied. To avoid this, a minimum flow rate of 0.25 L min^{-1} was set for both anode and cathode. This corresponds to the fuel cell operated at a constant flow rate mode up to 0.4 A cm^{-2} and 0.05 A cm^{-2} for anode and cathode, respectively.

2.4.3 Polarization curves and cell resistances

Polarization curves were obtained by recording the current density at set potentials. The cell potential was controlled from OCV to 0.4 V in 50 mV increments. The cell was maintained at each set potential for 3 min. before data collection, which was observed sufficient time to reach steady state. Eight polarization curves were taken for each set of operating conditions. Cell resistances were obtained by applying the current interruption method[120] using an integrated load bank (Scribner Associates). These resistances are confirmed to be identical to those obtained by an EIS measurement at 1 kHz using an AC m-Ohm tester (Model 3566, Tsuruga Electric Corp.) The pressure differences between the inlets and the outlets of the cell were measured using differential pressure transducers (Amplified transducer, Sensotec, Ohio); the average gas

pressure difference across the anode and cathode was defined as the average of the gas pressure differences at the inlets and the outlets.

2.4.4 Water transport through the operating MEA - net water flux coefficient (β-value)

β-values were calculated from the net water flux measured by collecting the water from both anode and cathode outlets, subtracting both the amount of (i) water generated electrochemically and (ii) water introduced as humidified gas. To estimate the latter, the flow rate of vapour supplied to the cell was measured by installing a polyethylene (PE) blocking film in the cell to separate the anode and cathode flow channels. Humidified hydrogen and air were then supplied to the heated assembled cell and water was collected by the water-cooled condensers at both the anode and cathode. The downstream gas temperatures were ensured to be at r.t. Values obtained here were used to determine the flow rate of water vapour introduced in the fuel cell ($j_{a\text{-}in}$, $j_{c\text{-}in}$). This procedure was performed at different flow rates in the range of 0.25 - 1.5 L min^{-1}. Results obtained here agreed well with the theoretically calculated values from the vapour pressure and the ideal gas law, indicating the proper functioning of the humidifier and the condensers.

The conditioned cell was operated at the desired constant current for at least 60 min before the first measurement and waited for 20 min for the subsequent measurements. After steady state was achieved, the three-way-valve installed at the outlets were switched to direct water to the condensers for collection. Each measurement produced >3.0 g of water. The accumulated

mass of water condensed was monitored. According to the mass of the water collected over time, the RH at the anode and cathode outlets were estimated. From the known RH of the gases introduced at the inlets, the average RH of the anode and cathode streams were estimated. As mentioned above, the amount of water collected at the cathode includes (i) electrochemically generated water, (ii) moisture carried by humidified air, (iii) and possibly water transported from the anode, the latter depending on the operating conditions. The water flux can be described by Equation 2-8.

$$J^{c}{}_{NET} = \frac{j_{c-out} - j_{c-in} - \frac{I}{2F}}{A} \quad \text{Equation 2-8}$$

where, I, A, F, and J^{c}_{NET} represent total current produced by the cell, geometrical active area of the cell, Faraday's constant and net water flux towards the cathode, respectively. $j_{c\text{-}in}$ and $j_{c\text{-}out}$ indicate flux of water introduced and exhausted from the cell's cathode stream. $j_{c\text{-}in}$ is determined from calibration measurements described above, while $j_{c\text{-}out}$ is the measured flux of water collected from the cathode exhaust.

The net water flux through the PEM was also determined from the amount of water collected at the anode. In this case, the loss or gain of water at the anode outlet was normalized to the MEA's geometrical active area to determine the flux. In this case, J^{a}_{NET} is given by:

$$J^{a}{}_{NET} = \frac{j_{a-out} - j_{a-in}}{A} \quad \text{Equation 2-9}$$

where, $j_{a\text{-}in}$ and $j_{a\text{-}out}$ is the flux of water introduced and determined from calibration measurements, while $j_{a\text{-}out}$ is the measured amount of water collected

from the anode. Mass fluxes are converted to molar fluxes. β, calculated by normalizing the net molar flux of water (J^a_{NET}) to the molar flux of protons (J_{H^+}), which was derived from the current density, is expressed as Equation 2-10.

$$\beta = \frac{J^a_{NET}}{J_{H^+}} \quad \text{Equation 2-10}$$

Net water fluxes and β-values reported are derived from the amount of water collected at the anode stream in order to maximize the signal-to-noise ratio. Sample data are shown in Appendix B.

The EOD flux (J_{EOD}) is a function of the current density (j) and can be calculated according to Equation 2-11.

$$J_{EOD} = \frac{jN_d}{F} \quad \text{Equation 2-11}$$

where F and N_d represent Faraday's constant and the EOD coefficient (H_2O/H^+), respectively. By assuming an EOD coefficient (N_d), the EOD flux can be estimated. Since the measured net *in-situ* water flux (J_{NET}) is the sum of J_{EOD} and the back permeation flux (J_{WP}), J_{WP} can be estimated according to Equation 2-12:

$$J_{WP} = J_{NET} - J_{EOD} \quad \text{Equation 2-12}$$

The triple serpentine flow channel design used in this work was suited to the nature of this type of water balance measurement. For instance, this flow channel design allowed the set gas flow rates to be relatively small that kept the ratio of J^a_{NET} and $J_{a\text{-}in}$ (the amount of water introduced at the anode, normalized by the cell area, 25 cm^2) to be in the range of 0.3 - 0.5 and 1.4 - 1.6 for the tested,

which are defined later (*c.f.*, section 3.2.2.2, conditions (a) and (d).) However, it has to be noted that the disadvantage of this small flow rate is the inhomogeneity of the humidity along the channel at high current density. For instance, the humidity of the saturated anode stream (>100% RH) was found to decrease to 80% RH at the outlet, while the humidity of the relatively dry (40% RH) anode stream increased to near saturation point at the outlet when water transport (J_{NET}) was the largest.

CHAPTER 3 MEASUREMENTS OF WATER PERMEATION THROUGH NAFION® MEMBRANE AND ITS CORRELATION TO *IN-SITU* WATER TRANSPORT*

3.1 Introduction

In this chapter, water flux measurements obtained *ex-situ* are compared to fuel cell water balance measurements obtained *in-situ*, under comparable conditions of temperature and relative humidity. The comparison is made with the specific purpose of revealing the role of back transport of water on fuel cell performance. More specifically, this chapter describes the comparison of water transport data obtained when a Nafion® NRE211 membrane is exposed to either liquid or vapour phases of water, and wherein a chemical potential gradient is developed across the membrane by either controlling the differential humidity in the case of water vapour or hydraulic pressure in the case of liquid water. Accordingly, three types of water permeation are defined:

a) Vapour-vapour permeation (VVP) – wherein both sides of the membrane are exposed to water vapour and the driving force for water permeation is created by off-setting the humidity on both sides of the membrane. This method is similar to what it is

*Sections of this work have been published in:
Journal of the Electrochemical Society, M. Adachi, T. Navessin, Z. Xie, B. Frisken and S. Holdcroft, 156, 6 (2009)

described as “Standard test methods of water vapour transmission of materials” in ASTM.[121]

b) Liquid-vapour permeation (LVP) – wherein one side of the membrane is in contact with liquid water and the other side is exposed to water vapour. The driving force for water permeation is controlled by varying the relative humidity of the vapour.

c) Liquid-liquid permeation (LLP) – wherein both sides of the membrane are in contact with liquid water and the driving force for water permeation is created by applying hydraulic pressure.

Ex-situ VVP, LVP and LLP permeabilities may be correlated to water transport through an operating fuel cell. Using *in-situ* net water balance measurements on fuel cells, the *ex-situ* permeability data are used to determine which mode of water transport (VVP, LVP, LLP) applies for an operational PEM for a given set of conditions. These studies provide specific information related to water transport properties of dispersion-cast, Nafion® NRE211 membranes and lead to a better understanding of the complex water transport phenomena occurring in PEMFCs.

3.2 Results and discussion

3.2.1 *Ex-situ* measurements of water permeation

3.2.1.1 Vapour-vapour permeation (VVP) and Liquid-vapour permeation (LVP)

The fluxes for vapour-vapour (VVP) and liquid-vapour permeation (LVP) cases through NRE211 membrane (28 μm-thick) are given in Figure 3-1. For VVP measurements, one side of the membrane was exposed to air humidified at 96% RH, while the RH of the opposite side was varied between 38 – 85%. For LVP measurements, the membrane was exposed to liquid water on one side while the RH of the other side was varied. For both types of measurements, a water concentration gradient is developed in the membrane, which serves to transport water to the side where the chemical activity of water is lower, *i.e.*, the side exposed to lower RH. The flux of water is observed to increase with a reduction in relative humidity of the "drier" side. The rate of water permeation for the case of LVP is much greater than for VVP.

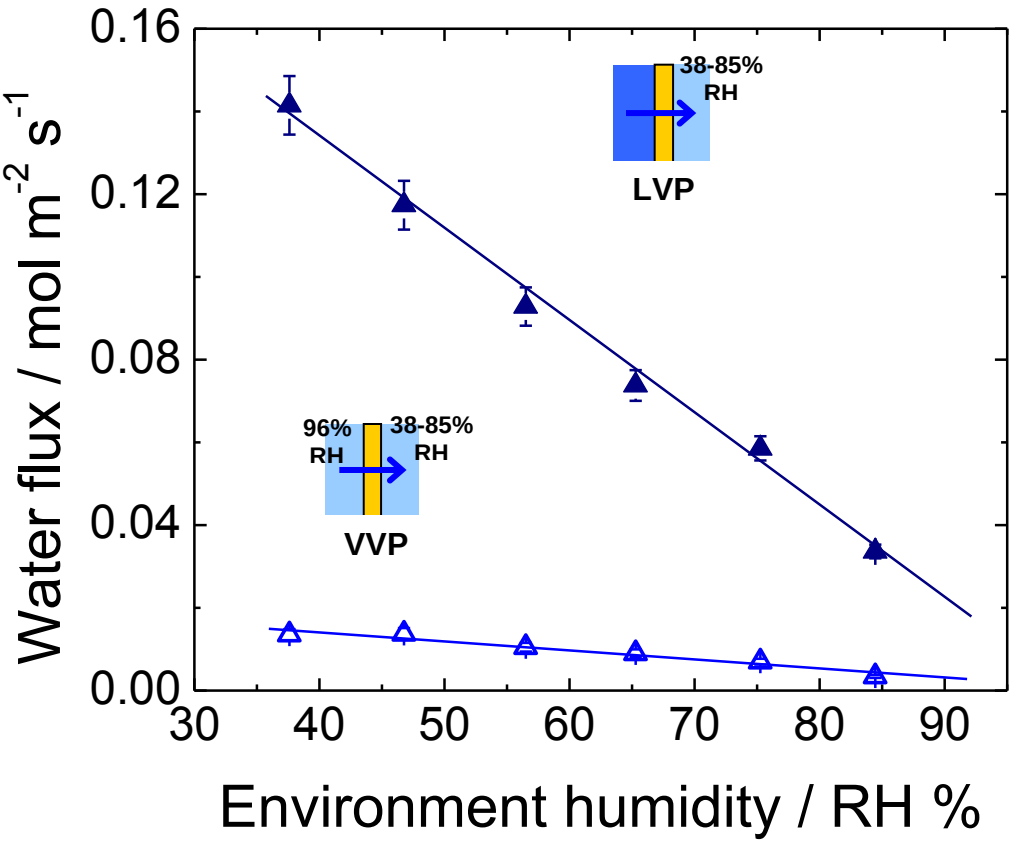

Figure 3-1 **Rate of water permeation through NRE211 at 70°C as a function of relative humidity of the drier side of the membrane. LVP configuration: liquid water/membrane/variable RH; VVP configuration: 96% RH/membrane/variable RH. LVP(▲) and VVP(△).**

3.2.1.2 Liquid-liquid permeation (LLP)

The water fluxes through NRE211 membrane (28 μm-thick) corresponding to the liquid-liquid permeation (LLP) case, in which transport is induced by application of hydraulic pressure, are shown in Figure 3-2. The permeance was determined from the linear slope of this plot to be 2.69 x 10^{-14} m Pa^{-1} s^{-1}. The

thickness-normalized permeability is 7.53 x 10^{-19} m^2 Pa^{-1} s^{-1}, which is similar in value to other values reported for Nafion® membranes.[122,123]

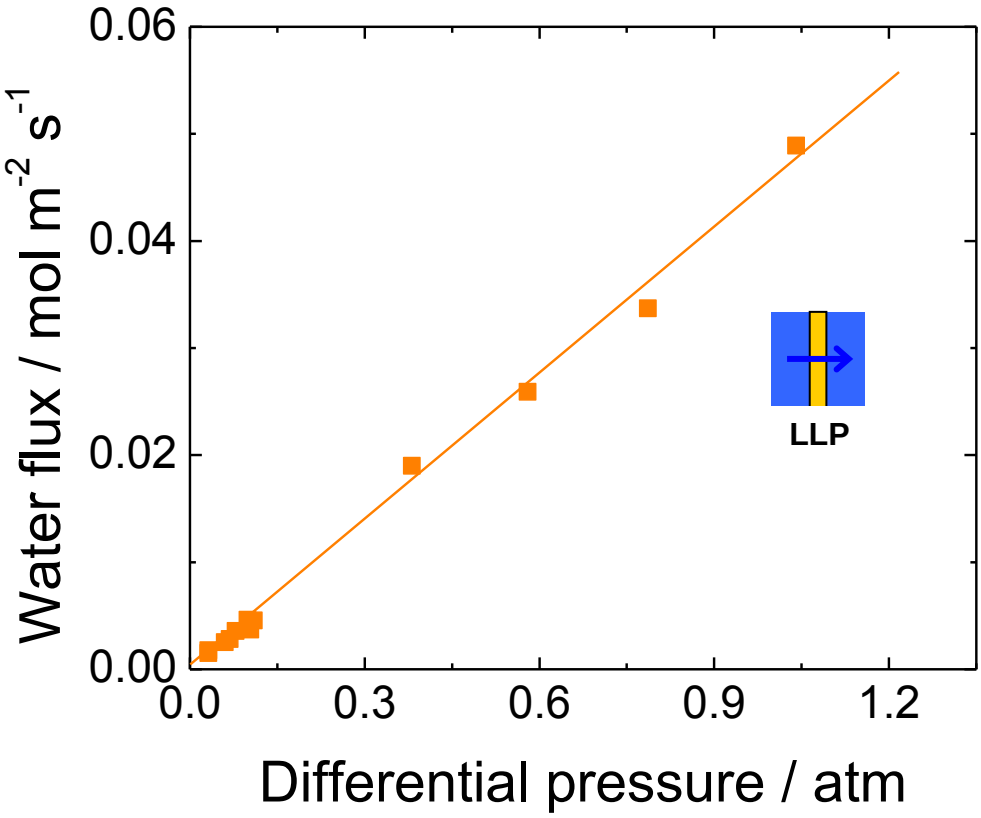

Figure 3-2 Rate of water permeation through NRE211 at 70°C as a function of hydraulic pressure difference (LLP).

3.2.1.3 Chemical potential of vapour, liquid water and pressurized liquid water

In order to quantitatively compare VVP, LVP, and LLP, and to compare the different water transport properties among various PEMs for fuel cell applications, the differential chemical potential of water across the membranes was calculated, as described below.

Chemical potentials of water in the liquid and vapour phase at various temperatures and 1.0 atm are given as:[124]

$$\mu^{0}{}_{liq\_T(x)} = \mu^{0}{}_{liq} + \gamma_{liq}\left(T(x) - T_{STD}\right) \quad \textbf{Equation 3-1}$$

$$\mu^{0}{}_{vap\_T(x)} = \mu^{0}{}_{vap} + \gamma_{vap}\left(T(x) - T_{STD}\right) \quad \textbf{Equation 3-2}$$

where μ^{0}_{liq} and μ^{0}_{vap} are the standard chemical potentials of liquid water and water vapour at 298 K, 1.0 atm: –237.18 kJ mol^{-1} and –228.59 kJ mol^{-1}, respectively. γ (J mol^{-1} K^{-1}) represents the temperature coefficient for the chemical potential of water in the liquid and vapour phase: –69.9 and –188.7 J mol^{-1} K^{-1}, respectively. The chemical potentials of liquid and vapour at 343 K, $\mu^{0}_{liq\_343K}$ and $\mu^{0}_{vap\_343K}$, are thus calculated to be –240.33 kJ mol^{-1} and –237.08 kJ mol^{-1}, respectively.

From the standard chemical potential of water vapour at 70°C, the chemical potentials of water vapour at various relative humidities were calculated according to Equation 3-3; where y indicates the relative humidity (expressed as %) and R, T, $p_{sat\text{-}vap}$ and p_{tot} correspond to the universal gas constant, temperature of the environment, saturated vapour pressure at that temperature and ambient pressure, respectively.[125] The chemical potentials of water vapour at various humidities at 70°C calculated from Equation 3-3 are plotted in Figure 3-3. As the relative humidity is increased towards saturation, the chemical potential of water vapour approaches that of liquid water.

$$\mu_{vap\_RH(y)} = \mu^{0}{}_{vap\_343K} + RT \ln \left[\frac{\left(\frac{y}{100} \right) p_{sat-vap}}{p_{tot}} \right] \quad \text{.....Equation 3-3}$$

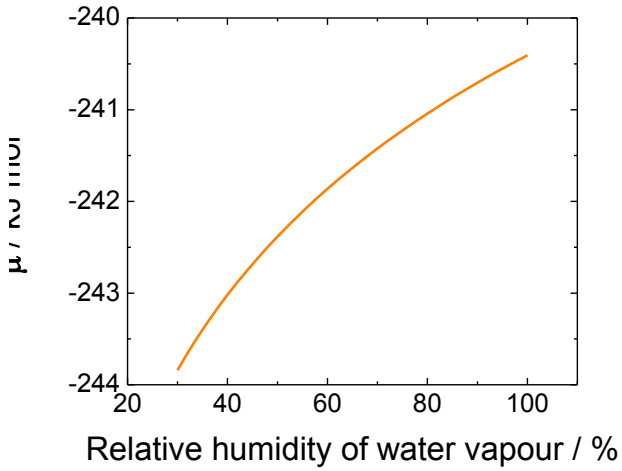

Figure 3-3 Calculated chemical potential of water vapour for the range of 30 – 100 %RH at 70°C.

The chemical potential of liquid water under pressure was estimated using Equation 3-4, where *p(z)*, p_{STD} and δ indicate the applied pressure, standard pressure and the pressure coefficient for water. Here, the standard pressure is 1 atm and the coefficient, δ, is 1.990 J mol^{-1} atm^{-1}.[124] The calculated chemical potentials of liquid water as a function of pressure are plotted in Figure 3-4.

$$\mu_{liq\_p(z)} = \mu^{0}{}_{liq\_343K} + \delta\left[p(z) - p_{STD}\right] \quad \text{Equation 3-4}$$

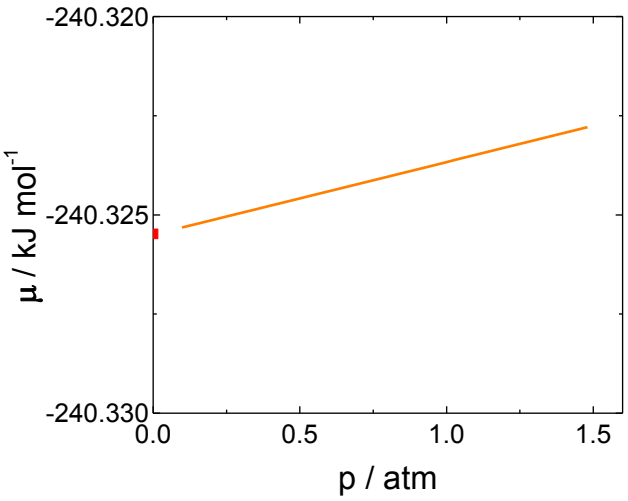

Figure 3-4 Calculated chemical potentials of pressurized liquid water for the range of 0 – 1.5 atm above ambient pressure at 70°C.

As illustrated in Figure 3-3 and Figure 3-4, the chemical potential of water vapour increases non-linearly with relative humidity, whereas the chemical potential of liquid water increases linearly with pressure. Moreover the variation in chemical potential of the latter is much smaller in magnitude. From Equations 3-1 and 3-3, Equation 3-5 and Equation 3-6 define the difference in chemical potentials of water for VVP and LVP measurements, where y corresponds to %RH. Similarly, From Equation 3-3 and 3-4, Equation 3-7 describes the difference in chemical potentials created for LLP measurements.

$$\Delta\mu_{VVP\_RH(y)} = \mu_{vap\_RH(96\%)} - \mu_{vap\_RH(y)} \quad \text{Equation 3-5}$$

$$\Delta\mu_{LVP\_RH(y)} = \mu^{0}{}_{liq\_343K} - \mu_{vap\_RH(y)} \quad \text{Equation 3-6}$$

$$\Delta\mu_{LLP\_P(z)} = \mu_{liq\_P(z)} - \mu^{0}{}_{liq\_343K} \quad \text{Equation 3-7}$$

3.2.1.4 Water permeation fluxes and chemical potential gradient

The differential chemical potential across the membrane constitutes the driving force responsible for water permeation through the membrane. The water fluxes reported in Figure 3-1 and Figure 3-2 are thus replotted in Figure 3-5 against the difference in chemical potentials of water on the other side of the membrane. The break in the axis is necessary because of the wide range of Δμ values generated in the LLP and LVP/VVP experiments. For all three types of water permeation measurements, the water flux was observed to increase linearly with increasing Δμ. Values of effective permeation coefficient (effective permeance), expressed as a function of chemical potential, were obtained from the slopes of the plots to be $(59 \pm 4.6) \times 10^{-4}$, $(52 \pm 1.7) \times 10^{-3}$ and 26 ± 0.80 $mol^2 m^{-2} s^{-1} kJ^{-1}$ for VVP, LVP and LLP measurements, respectively.

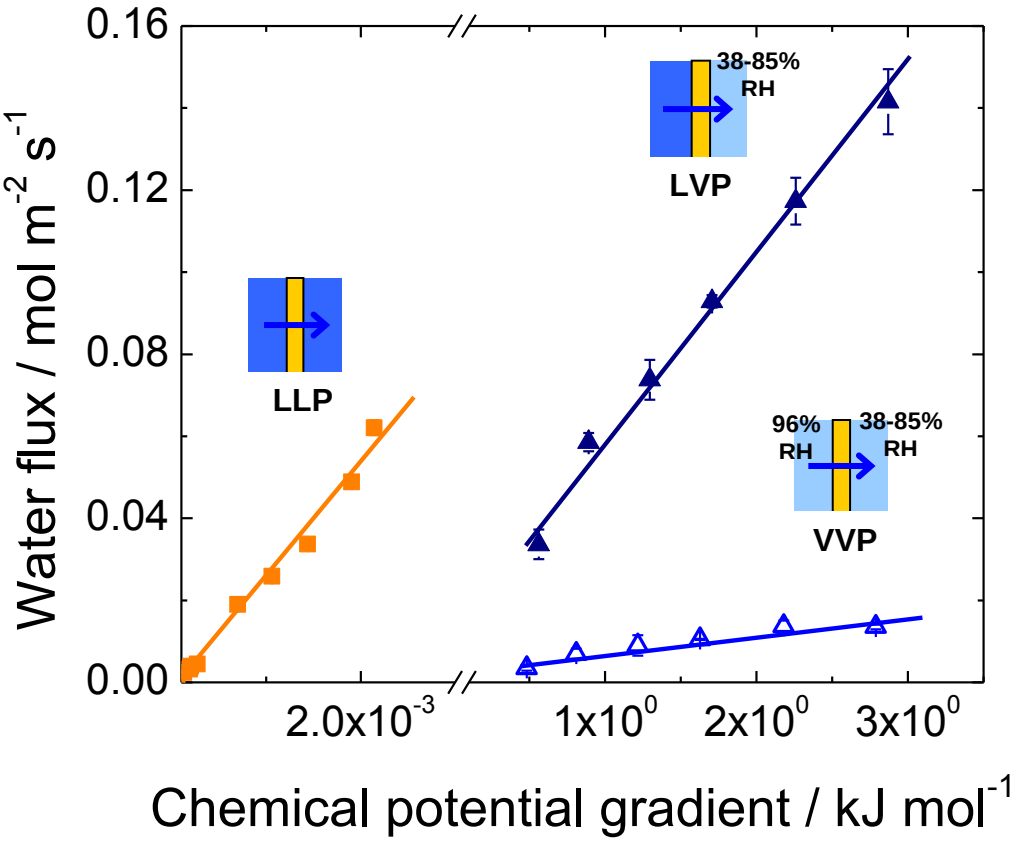

Figure 3-5 **Rate of water permeation at 70°C as a function of the difference in chemical potentials of water on either side of the membrane. LLP(■), LVP(▲) and VVP(△).**

The largest of the effective water permeation coefficients is obtained when liquid water is in contact with both sides of the membrane (LLP), the next largest when liquid is in contact with one side (LVP), and the smallest when both sides are exposed only to water vapour (VVP). LLP permeability coefficients are ~ 500 and 5000 times greater than LVP and VVP permeability coefficients, respectively. Two explanations are provided to account for these observations. The hydration state of the membrane is known to be an influential factor for water transport

through the membrane, with larger water contents leading to higher degrees of swelling and more facile water transport. As shown by numerical simulations and experimental measurements, and described by Kreuer and Paddison, “pores” of Nafion® expand upon hydration.[36] During the measurements, membranes exposed to liquid water on both sides (LL) are expected to contain a higher content of water than those exposed to vapour on one side (LV); which in turn, is expected to contain more water than those exposed to vapour on both sides (VV). The second explanation involves consideration of interfacial water transport (adsorption and desorption of water), which is known to play a significant role in the overall permeation of water, as discussed by Majsztrik et al.,[88] Romero et al.[86] and recently quantified by Monroe et al.[126] and Aotani et al.[63] In the LLP case, the formation of a liquid-membrane interface and a membrane/liquid interface is expected to facilitate ingress and egress of water into and out of the membrane, relative to the LVP case, for which water from the membrane must egress into the vapour phase (membrane/vapour interface); and relative to the VVP case, for which water must ingress from (vapour/membrane), and egress to (membrane/vapour), the vapour phase.

Despite the fact that the formation of liquid/membrane interfaces leads to a high permeability coefficient for water, the largest permeation flux of water is observed to be largest for the LVP measurements (see Figure 3-5). This is because the presence of vapour on one side of the membrane creates a much larger chemical potential driving force (3 - 4 orders of magnitude greater than for the LLP system). $\Delta\mu$ is relatively small for all reasonable hydraulic pressures

used in the LLP measurement, because pressure is an ineffective method for raising the chemical potential of a liquid.

The presence of a liquid-membrane interface, however, is noticeable when comparing the permeation fluxes of water under LVP conditions relative to VVP conditions. The observed permeation fluxes of water for the LVP measurements is much greater than for VVP measurements, even though Δμ is similar for both. Clearly, interfacial phenomenon, *i.e.*, a liquid/membrane interface versus a vapour/membrane interface is of great importance to the permeability of water. Majsztrik and others state a similar conclusion.[84,86,88]

In this work, the chemical potentials of water that are in contact with the membrane is calculated and is used to define the driving force for all three types of water permeation (*i.e.*, LLP, LVP and VVP). However, as Eikerling et al. suggest, a variation in the sizes of the hydrophilic pores may be attributed to the differences in chemical potential of liquid water within the membrane.[66] Especially under LVP and VVP conditions, sizes of the hydrophilic pores are expected to decrease towards the "drier side" due to the difference in hydration state across the membrane. In this scenario, smaller pores will attract water from the larger pores due to the internal capillary pressures, implying that an additional driving force for water permeation is created spontaneously within the membrane. The capillary pressure for a hydrophilic pore can be described by Kelvin's equation (Equation 3-8).[7,66]

$$p_c = \frac{2\gamma \cos\theta}{r_c} \quad \text{.....Equation 3-8}$$

where, p_c, γ, θ and r_c represent the capillary pressure (atm), surface tension (64 mN m^{-1} for liquid water at 70°C),[6] contact angle of the surface for the hydrophilic phase, and the capillary radius. While assuming the contact angle to be 0° (*i.e.*, assuming hydrophilic pores in Nafion® are completely wetted during water permeation), capillary pressures for pores with diameters in the range of 2 to 5 nm (*i.e.*, $1.0 \leq r_c \leq 2.5$ nm)[30,37,42] are calculated to be in the range of 1300 to 510 atm, respectively. This large difference in capillary pressures (*i.e.*, ~800 atm) translates to the difference in chemical potentials of water in 2 nm and 5 nm pores to be ~1.5 kJ mol^{-1}, according to the pressure coefficient discussed previously, *i.e.*, δ = 1.990 J mol^{-1} atm^{-1}. While the typical differences in chemical potentials under LVP and VVP conditions are found to be in the range of 0.37 – 2.9 kJ mol^{-1} (*c.f.*, pg. 59), a chemical potential gradient created by capillary pressure may create an effective driving force within the membrane under LVP and VVP conditions. However, due to the complexity and lack of experimental confirmation of the morphology and pore size distribution of the hydrophilic pores within Nafion membranes, the chemical potential gradient created within the membrane and internal capillary forces are not considered further in this thesis work.

3.2.2 *In-situ* measurements of water permeation

3.2.2.1 Polarization curves and the β-value

Polarization behaviour of NRE211 MEA

Polarization curves for an NRE211-based MEA at 70°C and under four different operating conditions are presented in Figure 3-6. The operating

conditions are: (a) wet anode (>100% RH, T_{dp} = 75°C) and dry cathode (40% RH), (b) dry anode (40% RH, T_{dp} = 50°C) and wet cathode (>100% RH, T_{dp} = 75°C), (c) wet anode and wet cathode (100% RH, T_{dp} = 70°C), and (d) wet anode and wet cathode with back pressure at the cathode (100% RH, T_{dp} = 70°C, +0.66 atm). Further details are provided in the experimental section. (*c.f.*, section 2.4)

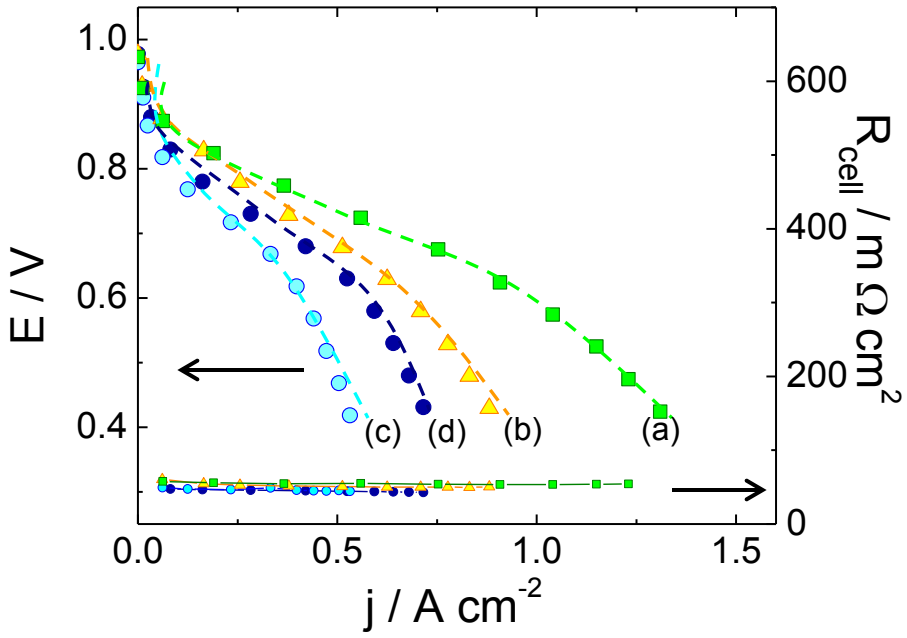

Figure 3-6 Polarization curves and cell resistances for NRE211-based MEAs obtained under different conditions. (a) ■: RH_{anode}>100%, $RH_{cathode}$=40%, (b) △: RH_{anode}=40%, $RH_{cathode}$>100%, (c) ○: RH_{anode}=100%, $RH_{cathode}$=100%, (d) ●: RH_{anode}=100%, $RH_{cathode}$=100%, $BP_{cathode}$= 0.66 atm. Cell temperature: 70°C. Humidified hydrogen and air were supplied in a stoichiometric ratio 2.0: 3.0.

The highest current was observed for case (a), when the anode was fully humidified and the cathode was operated with air introduced at lower humidity. 0.97 A cm^{-2} was generated at 0.6 V under these conditions. When the anode was fed with gases at a lower humidity and the cathode was fully humidified, *i.e.*,

case (b), the single cell performance reduced to 0.67 A cm^{-2} at 0.6 V. When both the anode and cathode were fully humidified, case (c) the performance decreased to 0.42 A cm^{-2}, but improved upon application of a back pressure applied to the cathode, *i.e.*, case (d), to 0.56 A cm^{-2} at 0.6 V. The correlations of performance with the different operating conditions is not unexpected: For case (a), reducing the humidity at the cathode reduces the likelihood of its flooding, while fully humidifying the anode reduces its propensity to dehydrate; case (b) promotes flooding at the cathode and dehydration of the anode, relative to case (a). The performance under these conditions is discussed later. In case (c), the fully humidified gases are likely to flood the cathode, limiting the fuel cell performance; this is partially mitigated by the application of back pressure, case (d) which forces water from the cathode to the anode.

3.2.2.2 Water transport through NRE 211-based MEAs

Net water fluxes at the anode and cathode were measured for fuel cells operated under the same conditions described above. These fluxes are plotted in Figure 3-7 as a function of current density.

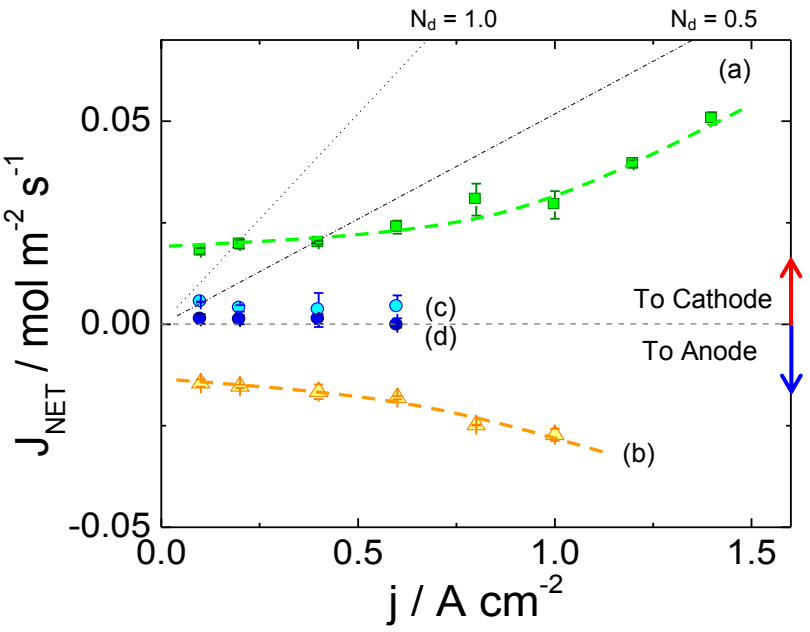

Figure 3-7 Net water flux as a function of current density obtained under different conditions. (a) ■: RH_{anode}>100%, $RH_{cathode}$=40%, (b) △: RH_{anode}=40%, $RH_{cathode}$>100%, (c) ○: RH_{anode}=100%, $RH_{cathode}$=100%, (d) ●: RH_{anode}=100%, $RH_{cathode}$=100%, $BP_{cathode}$= 0.66 atm. Dashed lines indicate the estimated EOD flux for N_d = 0.5 and 1.0 (*c.f.*, Equation 2-11)

In case (a), a positive water flux (anode-to-cathode) was observed. This is because both the chemical potential gradient, Δμ, formed by application of the differentially humidified gases, and the EOD flux act in concert to direct water from the anode to the cathode. For current densities up to ~0.4 A cm^{-2}, the flux of water is ~0.020 mol m^{-2} s^{-1}. In this regime, the measured flux seems to be independent to the current density and the EOD flux, implying that the concentration gradient driven fluxes, *i.e.*, VVP or LVP, is the major contributor to the net water flux. At higher current densities, *i.e.*, >0.6 A cm^{-2}, the EOD flux plays a more significant role in the net water transport and the water flux is observed to increase steadily as more current is drawn.

In case (b), a negative water flux (cathode-to-anode) is observed. For low current densities (<0.4 A cm^{-2}), the net water flux is ~ 0.015 mol m^{-2} s^{-1}. As in case (a), EOD is negligible in this region and thus the net water flux is due to the permeation of water resulting from the concentration gradient that is formed from a fully humidified cathode and partially humidified anode. As the current density is increased (above 0.6 A cm^{-2}), the net water flux towards the anode increases, despite the fact that EOD brings water from the anode to the cathode. This phenomenon will be discussed later. (*c.f.*, pg. 71)

Small, positive net water fluxes are observed for case (c). Under low current density operation, under these conditions, there is little external driving force ($\Delta\mu$) for water permeation to occur, as the RH at the anode and cathode are similar. Despite EOD potentially exerting a more dominant effect at higher current densities the net water flux as a function of current remains flat and small, possibly the result of back-transport of water from the water-generating cathode. Applying a back pressure to the cathode, case (d) forces water from cathode to anode. Hence the net water fluxes are slightly lower in value than those observed for case (c), and in fact the net water flux is ~ zero at 0.6 A cm^{-2}.

As background to further discussion of the results, the possible water fluxes operating within the membrane under the four different fuel cell conditions are summarized in Figure 3-8.

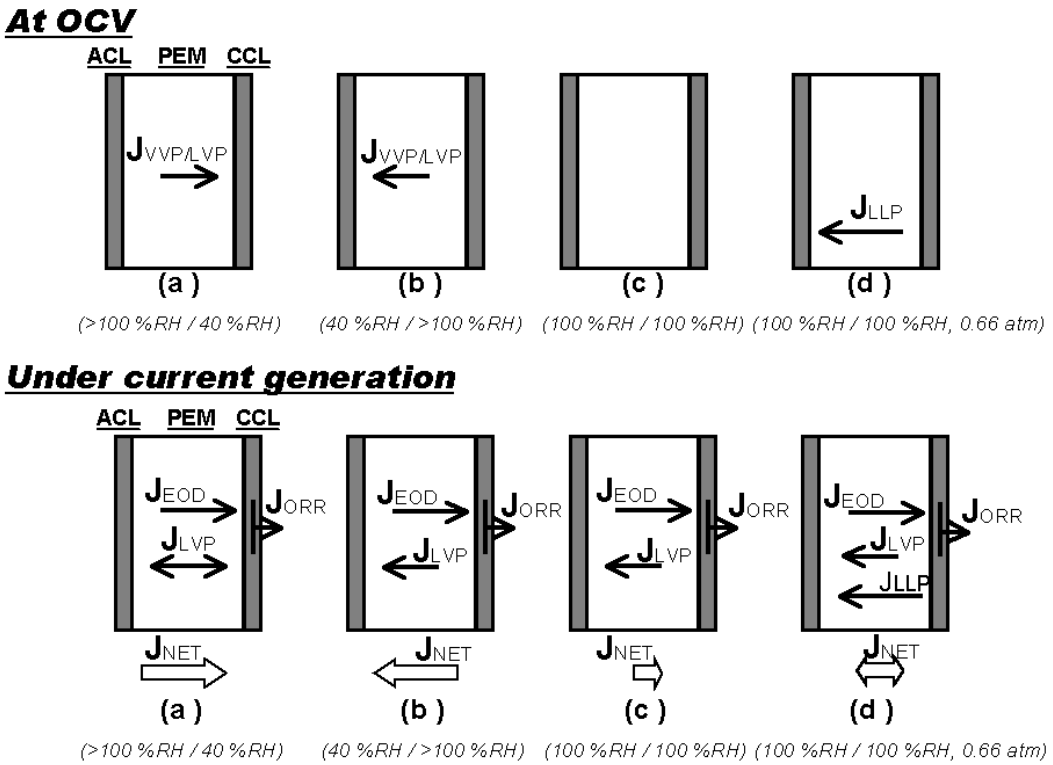

Figure 3-8 Scenarios for steady-state water transport within the membrane under four operating conditions. J_{NET} indicates the direction of measured net water flux.

Under open circuit voltage conditions (OCV), *i.e.*, zero current, water transport from anode-to-cathode is expected to occur in case (a) because of the differential humidity of the hydrogen and air. For similar reasons, water transport is expected to occur in the opposite direction, cathode-to-anode, for case (b). The fluxes of water, shown in Figure 3-7, when extrapolated to zero current are 0.018 and 0.014 mol m^{-2} s^{-1} for case (a) and (b), respectively. Given that gases are supplied to one side of the membrane fully humidified and the other at ~40% RH, two possible scenarios exist: (1) the membrane is exposed to liquid water at the fully humidified side of the membrane and 40% water vapour at the other side, to form a situation that is equivalent to conditions described by LVP *ex-situ*

measurements; (2) The membrane is exposed to saturated water vapour on one side and 40% RH on the other, as described by VVP measurements. Scenario (1) can be discounted because a membrane exposed to liquid on one side and 40% RH (LVP) on the other is capable of transporting ~0.14 mol m^{-2} s^{-1} of water (*i.e.*, an order of magnitude greater than the *in-situ* fluxes observed), as determined from the LVP plot shown in Figure 3-1. Scenario (2), on the other hand is consistent with the observed water fluxes. A membrane exposed to 96% RH on one side and 38% RH on the other transports ~0.014 mol m^{-2} s^{-1} water (*i.e.*, similar to the observed fluxes), as determined from the VVP plot shown in Figure 3-1. The data are thus interpreted as indicating that at OCV the PEM is exposed to water vapour on both sides despite one of the gases being saturated with moisture. This statement does not preclude liquid water forming in micropores in the catalyst layer, it simply implies that the membranes do not experience bulk liquid water at its interface, under these conditions.

In case (c), no water transport in either direction is expected at OCV, as no external chemical potential gradient of water exists across the membrane. However, in case (d), pressure is applied to the cathode and it is interesting to consider whether water can be transported as described by LLP of the type indicated in Figure 3-2. According to this plot, the LLP permeation flux under 0.66 atm differential pressure is 0.033 mol m^{-2} s^{-1}. However, the water flux at OCV in the fuel cell for case (d) has not been measured.

When current is drawn from the cell, water is generated at the cathode at a rate that is directly proportional to current. Furthermore, the flux of protons

creates an EOD that draws additional water from the anode to the cathode. The EOD is a nebulous parameter to measure or quantify, since the coefficient, N_d, is highly dependent on the water content of the membrane, as illustrated in Table 1-2, and can vary largely with current density and with the net direction of water transport in the membrane.

In the context of this work, the scenarios where N_d = 0.5 and 1.0 are considered, as Ge et al. have reported EOD coefficients to lie in the range of 0.3 – 1.0 for vapour equilibrated MEAs. It is interesting to note when N_d = 0.5, the EOD flux brings water to the cathode at the same rate as that produced by reduction of oxygen, when N_d = 1.0, the rate at which water is produced (generated and transported) at the cathode is triple that of when where EOD is absent. Estimates of EOD, ignoring forward- or back-transport of water, for N_d values of 0.5 and 1.0 are plotted in Figure 3-7 as a function of current density.

EOD for N_d = 0.5 is particularly significant in this work as the plot is near-parallel to the net water flux vs current for fuel cells operated under conditions described as case (a). At current densities of 1.0 – 1.4 A cm^{-2} the measured net water flux increases linearly with current, which is an expected observation when the rate of back transport has reached a limiting value and where further increases in water flux are caused by the linear increase in EOD with current. In other words, N_d under these conditions, and over this high current region, is estimated to be 0.5. Although it is speculation to comment on whether N_d is different or not for lower current densities, it is reasonable to assume that N_d

reaches a maximum when the membranes are sufficiently hydrated, which occurs for case (a) at high current densities.

For fuel cells operated under conditions described as case (a), the measured net water fluxes lie well below those estimated from the EOD flux for N_d = 0.5, except for very low current densities, where the flux of water is dominated by concentration gradient driven permeation. This estimation of N_d = 0.5 is a conservative estimation according to other literature values (*c.f.*, Table 1-2). Comparing the net water flux of water at 1.0, 1.2, and 1.4 A cm^{-2} with the flux theoretically generated by EOD (N_d = 0.5), it is deduced that the actual net water flux of water is consistently 0.022 mol m^{-2} s^{-1} lower than the estimated EOD at each current density. This suggests that back transport of water to the anode plays a significant role in determining the water balance.

This raises the question as to which mode of permeation is operating: LLP, LVP, or VVP? Insight to this question can be sought by considering which process is intuitively likely to be operating, and which is capable of producing a permeability of water of at least 0.022 mol m^{-2} s^{-1}. LLP can be quickly discounted because the differential pressure generated in the cell would have to be unreasonably high to achieve this rate of permeation. For instance, *ex-situ* LLP measurements indicate that it requires 0.46 atm differential pressure to support a water flux of 0.022 mol m^{-2} s^{-1}, as can be derived from Figure 3-2 – but no such pressure is applied to the fuel cell and it is unlikely the cell would generate this pressure internally (*c.f.*, section 4.2.2). Furthermore, it is highly unlikely that the PEM at the anode is saturated at liquid water; given that it is exposed only to

water vapour and that the net flow of water occurs from anode to cathode. Similarly, VVP can be eliminated as a mode for water transport because permeabilities in excess of 0.014 mol m^{-2} s^{-1} are only achievable, according to Figure 3-1, when the RH on the drier side < 38%. Recall that in case (a) the anode is fed with 100% RH hydrogen while the cathode is fed with 40% RH. As, water is produced at the cathode and accumulated at the cathode by EOD, the effective RH at the cathode at high current must be substantially higher than 40%, possibly, the membrane is exposed to liquid water. Of the three scenarios for water permeation, only LVP is capable of sustaining the rate of water permeation required to account for back-transport. As a substantial amount of water is generated/accumulates at the cathode under high current it is not unreasonable to consider that the PEM on the cathode side is exposed to liquid water. The RH of the hydrogen at the anode inlet is at saturation, but the outlet humidities are calculated to be decreased to 99 – 85% RH, based on the amount of water introduced and transported, which could generate a chemical potential gradient and may explain why water is transported towards the anode. Figure 3-1 (LVP) indicates that the water permeability is 0.034 mol m^{-2} s^{-1} when the membrane is exposed to liquid water on one side and ~84% RH vapour on the other, which is capable of sustaining the level of back-transport calculated above (0.022 mol m^{-2} s^{-1}). In summary, the back transport of water for fuel cells operated at high current under case (a) [wet anode (>100% RH) and dry cathode (40% RH)] could be explained by LVP where the membrane on the cathode side is exposed to liquid water while the anode side is exposed to vapour.

The influence of EOD and back transport on the net water flux for MEAs operated under conditions described by case (b) [dry anode (40% RH) and wet cathode (>100% RH)] can be reasoned using similar arguments, but taking into account that the initial humidities are reversed. Assuming for sake of discussion that Nd = 0.5, the EOD flux is 0.052 mol m^{-2} s^{-1} towards the cathode at 1.0 A cm^{-2}, as given in Figure 3-7. The actual net flux of water is -0.027 mol m^{-2} s^{-1}, towards the anode, at 1.0 A cm^{-2}. Clearly, back-transport of water offsets EOD. The difference in water fluxes indicates that back transport is ~ 0.079 mol m^{-2} s^{-1}. When the operating mode of permeation is considered, LLP can be quickly discounted as the source for back-water transport because water fluxes of this magnitude require differential pressures in excess of 1 atm (see Figure 3-2). VVP can be discounted because such fluxes cannot be reasonably achieved for this magnitude of water permeation (see Figure 3-1), and because it is highly likely that the cathode side of the membrane is exposed to liquid water because the initial humidity is at saturation point, and water is generated at the cathode. If the cathode side of the membrane is considered as being wet and the anode side exposed to 40% RH, it is reasonable to assume from Figure 3-1 indicates that LVP is capable of sustaining the level of back-transport observed for case (b) in Figure 3-7.

For fuel cells operated under conditions described by case (c) (see Figure 3-8), the net water fluxes are positive, but relatively small, when current is drawn (see Figure 3-7). Since both gases are supplied fully humidified and water is generated at the cathode, it is assumed the membranes are well hydrated. The

low value of the cell resistance obtained by current interruption method reported in Figure 3-6 for operating fuel cells supports this. Thus, it is reasonable to assume N_d is ~0.5 as observed for case (a), and that EOD is much larger (and positive) with respect to the observed net flux. Since expected water flux is low in this case, the EOD flux is expected to be the dominant contributor to the net flux of water. However, since the net water does not follow the trends from the estimated EOD flux, VVP and/or LVP type water transport appears to regulate the water balance within the MEA. VVP is, however, discounted as a mechanism for back transport because it is highly likely that the cathode side of the membrane is exposed to liquid water given the initial humidity is at saturation point and because water is generated at the cathode. This leaves LVP to explain back transport since case (c) was operated at ambient pressure. Case (d) represents identical conditions to case (c) with the addition of a differential pressure of 0.66 atm between the two electrodes. A differential pressure of 0.66 atm would be expected to provide an additional 0.033 mol m^{-2} s^{-1} of water flux back to the anode if the transport was described by LLP (see Figure 3-2). However, the net water fluxes at the various current densities are only marginally more negative that those in case (c), lowering the net flux by values ranging from 0.0043 to 0.0003 mol m^{-2} s^{-1} at 0.6 A cm^{-2}. While more work needs to be substantiate this, it appears that LLP is not operating even in these highly hydrating states. The difference between estimated EOD and the net water flux can easily be accounted for by LVP. The effect of back pressure on LVP

scenario warrants further investigation, as it was not taken into account in these studies.

In Figure 3-9, water fluxes were converted to net water transport coefficients, β, which reveals the net number of water molecules transported, and their direction, as a function of the protonic flux. Positive β-values indicate net water transport from anode to cathode; negative values indicate the reverse. Large β-values observed at lower current density regions for case (a) and case (b) are the result of the small proton flux compared to the net water transport through the MEA due to VVP or LVP type permeation. The significance of looking at the β-values is its tendency of converging to a constant value at higher current densities. β-values converge to 0.32, -0.28, 0.11 and 0.055 for conditions (a), (b), (c) and (d), respectively. Despite the fact that EOD coefficient (N_d) appears to have a value of ~ 0.5, or even larger according to other reported values, the β-values are smaller, due to the influence of back transport. β-values observed for case (c) and case (d), which differ in only in differential pressure indicate that the differential pressure exerts a relatively small effect. This again suggests that back transport in case (c) and case (d), is dominated by LVP, and not LLP, as the latter would be more susceptible to the application of biased back pressure.

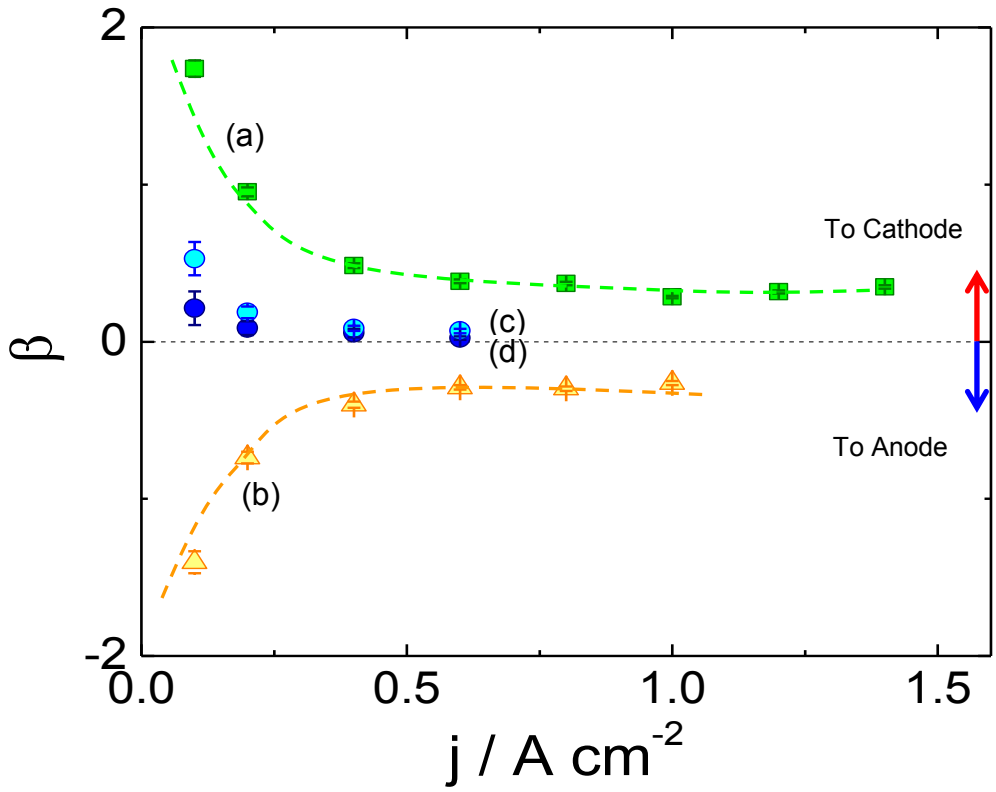

Figure 3-9 Net water transport coefficients (β-values) obtained for four different operating conditions. (a) ■: RH_{anode}>100%, $RH_{cathode}$=40%, (b) △: RH_{anode}=40%, $RH_{cathode}$>100%, (c) ○: RH_{anode}=100%, $RH_{cathode}$=100%, (d) ●: RH_{anode}=100%, $RH_{cathode}$=100%, $BP_{cathode}$= 0.66 atm. Cell temperature: 70°C. Humidified hydrogen and air were supplied in a stoichiometric ratio 2.0: 3.0.

3.3 Conclusion

Liquid-liquid permeation (LLP), liquid-vapour permeation (LVP) and vapour-vapour permeation (VVP) fluxes were measured for dispersion cast, 25 μm, NRE211 membrane at 70°C. Water fluxes increased with increase in chemical potential gradient across the membrane for all three types of permeations. Water permeation coefficients, *i.e.*, water flux values normalized to the chemical potential gradient of water and membrane thickness, were

determined for each scenario of water permeations. The largest water permeation coefficient was obtained for LLP due to it's the high hydration state of the membrane as well as favourable water sorption and desorption processes at the membrane-liquid water interface. However, the difference in chemical potential of water across the membrane created by application of reasonable hydraulic pressure gradients are calculated to be three orders of magnitude smaller than those generated by scenarios described by VVP and LVP. The significance of the chemical potential gradient of water across the membrane is significant in determining the water flux in operating fuel cells.

The water flux through this thin Nafion® membrane is largest when the membrane is exposed to liquid on one side and vapour on the other. LVP water transport is largely responsible for regulating water balance within the operating MEA. This leads to a conclusion that formation of a chemical potential gradient for water and good hydration at the interface and across the membrane allows the membrane to self-regulate water content across the operating MEA. When both these factors work together, in the cases of LVP, the water permeation flux is large enough to offset the substantial EOD flux in an operating fuel cell.

.

CHAPTER 4 THICKNESS DEPENDENCE OF WATER PERMEATION THROUGH NAFION® MEMBRANES*

4.1 Introduction

Water management is crucial to the operation of PEMFCs. As observed in Chapter 3, too much water at the cathode suppresses the transport of gaseous reactants and affects the fuel cell performance.[9,19,66,127] At 1 A cm^{-2}, the rate of water generated by ORR is 0.052 mol m^{-2} s^{-1}. Additionally, water is transported towards the cathode by electro-osmotic drag (EOD). The EOD coefficient (number of water molecules transported per proton) is reported to be in the range of 0.3 to 3.0.[58-63,63,64] At 1 A cm^{-2}, and for an EOD coefficient (N_d) of 0.5, the combined rate of water transport/generation at the cathode is 0.10 mol m^{-2} s^{-1} (0.15 mol m^{-2} s^{-1}, when N_d = 1.0. *c.f.*, Equation 2-11). While water may exhaust from the cathode via the gas diffusion layer, it would be favourable for the water to permeate back to the anode via the membrane since this may mitigate the need to humidify the anode; moreover, water exiting via the GDL may impede incoming oxygen gas.[65] Understanding water management, and the permeability of the membrane to water are thus required for further advancement of PEM fuel cell technology.

---

*Sections of this work have been submitted to:
Journal of Membrane Science, M. Adachi, T. Navessin, Z. Xie, N. Li, S. Tanaka and S. Holdcroft, (2010)

In Chapter 3, water permeation fluxes through Nafion® NRE211 membrane were obtained under three different permeation environments.

i) Vapour-vapour permeation (VVP) – wherein both sides of the membrane are exposed to water vapour and the driving force for water permeation is created by offsetting the humidities. This is termed vapour-permeation.[75,76] The VVP flux for conditions of 96% RH/NRE211/38% RH at 70°C is 0.016 mol m^{-2} s^{-1}.[25]

ii) Liquid-vapour permeation (LVP) – wherein one side of the membrane is exposed to liquid water and the other side is exposed to water vapour. This is similar to pervaporation except the pressure on both sides of the membrane is equal.[128,129] The LVP flux for conditions of liquid water/NRE211/38% RH at 70°C is 0.14 mol m^{-2} s^{-1}.[25]

iii) Liquid-liquid permeation (LLP) – wherein both sides of the membrane are exposed to liquid water and the water permeation is driven by hydraulic pressure gradient across the membrane. The hydraulic permeability of NRE211 was found to be 2.43 x 10^{-16} m^2 Pa s^{-1} and the LLP flux for a differential pressure of 1.0 atm is 0.048 mol m^{-2} s^{-1}.[25]

The larger fluxes of LVP, compared to VVP, is attributed to contact of the membrane with liquid water.[63,84,86,88,107,114] An earlier study by Thomas et al. revealed the difference in water content of membranes exposed to liquid and vapour.[130] They also report water content profiles within 190 µm-thick Nafion® membranes using SANS for vapour-equilibrated, vapour permeation, and pervaporation conditions. Although, permeabilities were not reported, the water

concentration gradient within the membrane is larger during pervaporation compared to vapour permeation due to the presence of liquid water in the former. Bode et al. studied the effect of the membrane interface during permeation of water and estimated the *interfacial* water exchange flux associated with a 30 μm-thick poly(ether-block-amide) membrane.[131] They used a solution-diffusion model to show that the permeation flux increases proportionally with concentration gradient and decreases with membrane thickness. The model describes permeation data for dense, thick membranes, in which the bulk diffusion within the membrane is rate-limiting; but in the case of thin membranes, when *interfacial* mass transport was not negligible, the model was not applicable, and the rate of *interfacial* mass transport had to be taken into account.

In this work, the water permeabilities through Nafion® membranes of wet thicknesses ranging from 6 to 201 μm are described, in order to examine the relative importance of *interfacial* and *bulk* water transport resistances.

4.2 Results

4.2.1 *Ex-situ* measurements of water permeation

The LLP fluxes of water through Nafion® membranes are shown in Figure 4-1. Each data point represents the steady state flux for a given pressure difference. The upper axis represents the corresponding chemical potential difference, as derived in section 3.2.1.3. The slope of the plot, the permeance (water flux per unit difference in chemical potential), increases as the membrane

thickness is reduced. Permeance values, and the values normalized to membrane thickness, the permeability of the membrane to water, are summarized in Table 4-1.

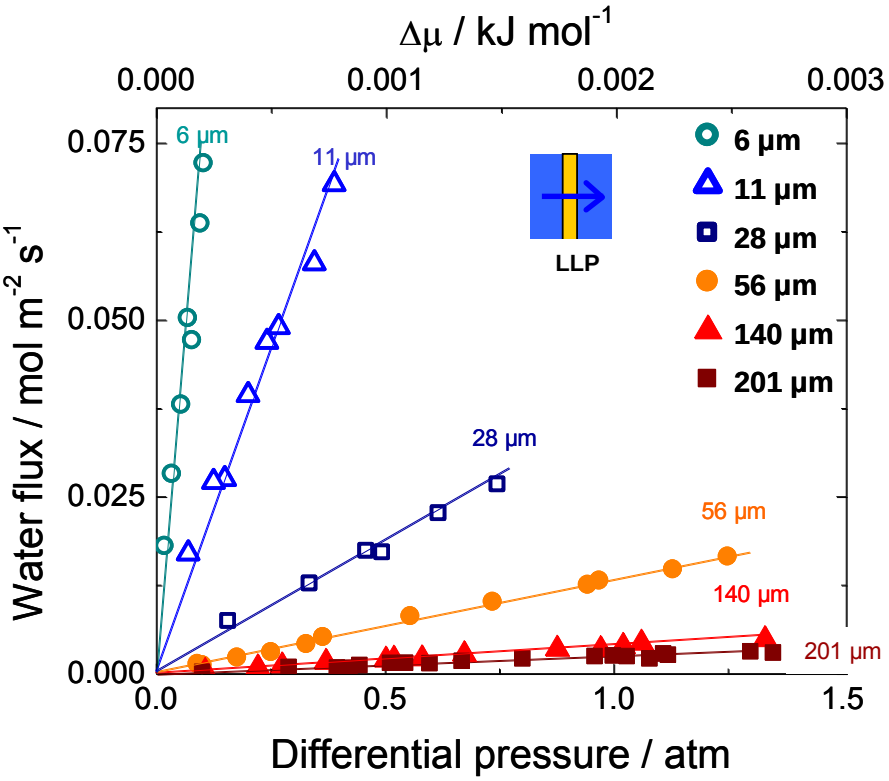

Figure 4-1 **Liquid-liquid permeation (LLP) fluxes of water through Nafion® membranes versus differential pressure at 70°C. The differential chemical potential is presented on the top axis.**

Table 4-1 **Hydraulic permeance and permeability (LLP) through Nafion® membranes at 70°C.**

	Wet thickness / μm	Permeance / $mol^2\ m^{-2}\ s^{-1}\ kJ^{-1}$	Permeability / $10^{-4}\ mol^2\ m^{-1}\ s^{-1}\ kJ^{-1}$
Dispersion -cast membranes	6	324	19.4 ± 0.4
	11	99.4	10.3 ± 0.3
	28	19.1	5.36 ± 0.11
Extruded membranes	56	7.01	3.93 ± 0.04
	140	2.05	2.87 ± 0.05
	201	1.21	2.43 ± 0.06

LVP and VVP fluxes of water through Nafion® are shown in Figure 4-2(a) and (b), respectively, as a function of the RH of the drier side. The corresponding chemical potential differences are larger than those produced under LLP conditions (*c.f.*, Figure 4-1), as application of a pressure gradient is a less effective means of developing a chemical potential difference (*c.f.*, 3.2.1.3). Both LVP and VVP fluxes of water are observed to increase with decreasing RH. The range of water fluxes for LVP fluxes was much larger in comparison to VVP. Water fluxes of LVP and VVP increased, with decreasing membrane thicknesses.

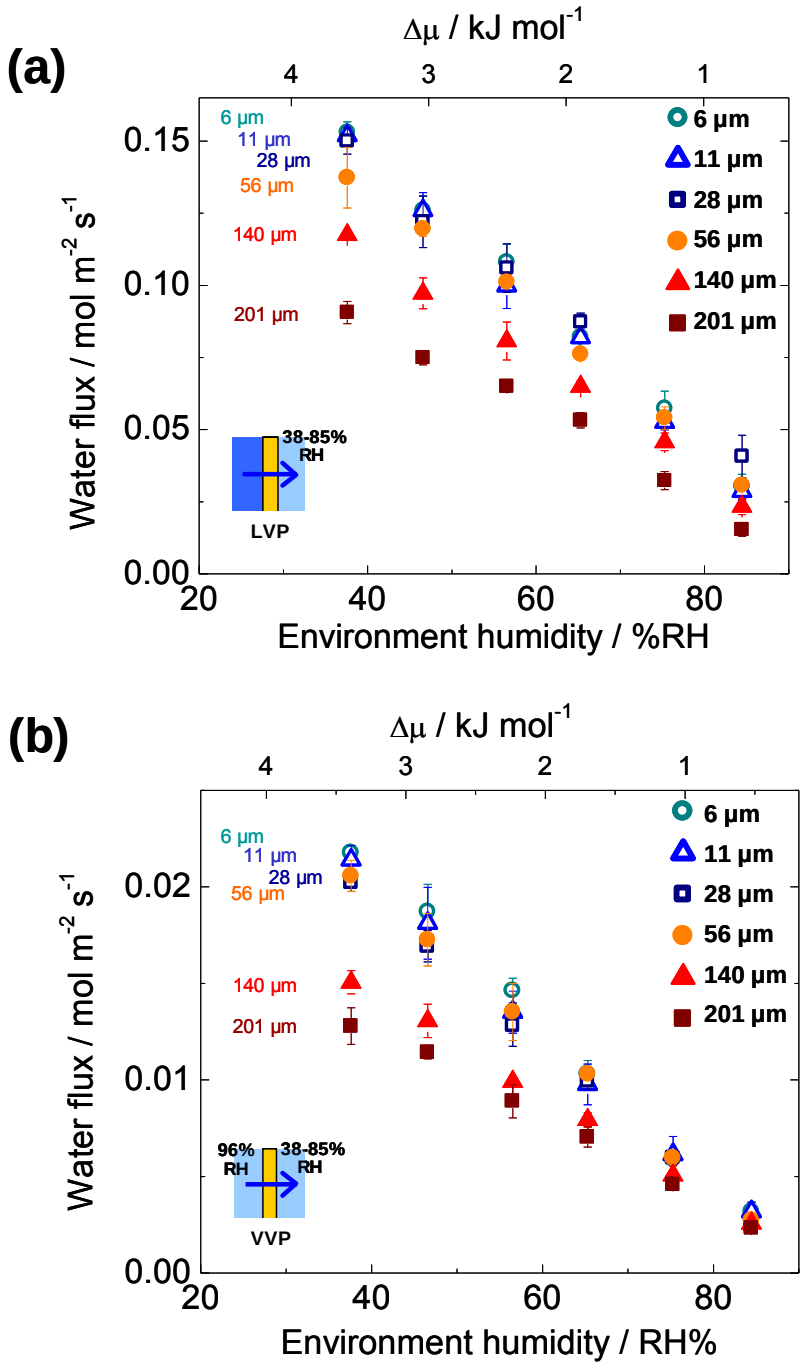

Figure 4-2 **(a) Liquid-vapour permeation (LVP) fluxes and (b) vapour-vapour permeation (VVP) fluxes of water through Nafion® membranes versus environment humidity at 70°C. The differential chemical potential is presented on the top axis.**

Figure 4-3 compares LLP, LVP and VVP water fluxes. For LLP, a differential pressure of 1.0 atm was taken. For LVP and VVP, the conditions were liq./PEM/38% RH and 96% RH/PEM/38% RH, respectively. For liquid-vapour permeation conditions, reducing the membrane thickness from 201 μm to 56 μm resulted in water fluxes to increase from 0.091 ± 0.002 to 0.137 ± 0.006 mol m^{-2} s^{-1}. However, a reduction in membrane thickness from 28 μm to 6 μm yielded similar LVP fluxes (0.150 ± 0.003 and 0.153 ± 0.002 mol m^{-2} s^{-1}, respectively). Similarly, for vapour-vapour permeation conditions, reducing the membrane thickness from 201 μm to 56 μm resulted in water fluxes to increase from 0.0134 ± 0.0005 to 0.0206 ± 0.0004 mol m^{-2} s^{-1}. However, reducing the membrane thickness from 28 μm to 6 μm gave similar VVP fluxes (0.0202 ± 0.0002 and 0.0213 ± 0.0003 mol m^{-2} s^{-1}, respectively). The maximum LVP and VVP fluxes observed in this work were ~0.15 and ~0.021 mol m^{-2} s^{-1}, respectively. Majsztrik et al., Romero et al. and others[63,81,84,86,88] ascribed this phenomena to the relatively slow rate of water transport at the membrane interfaces. This has been discussed in the context of VVP and LVP measurements on NRE211 membranes (*c.f.*, Chapter 3). If the transport rates of water vapour at the membrane interfaces are slow compared to the rate of water transport within the membrane, then *interfacial* processes may become rate-limiting - and may explain why the LVP and VVP fluxes reach a maximum.

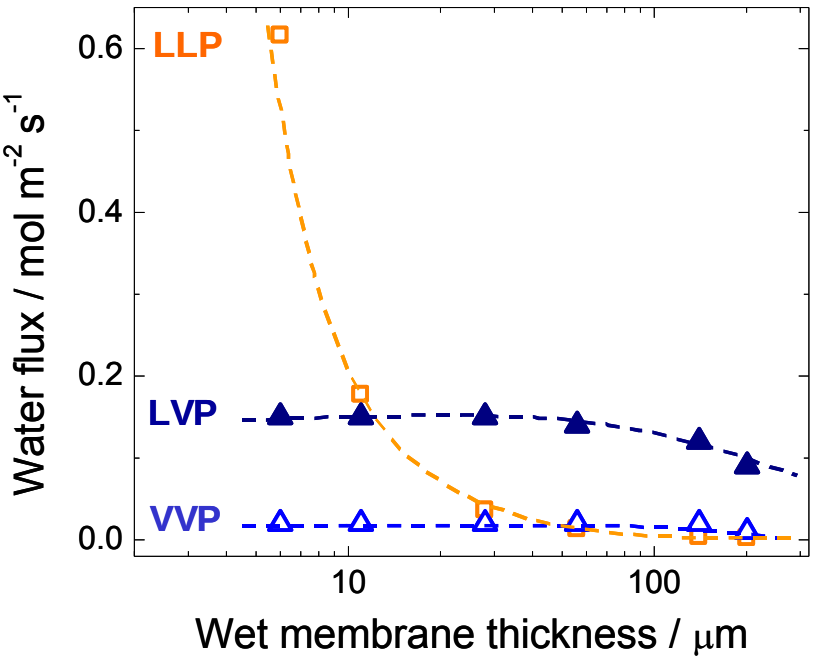

Figure 4-3 LLP, LVP and VVP fluxes for Nafion® membranes versus wet membrane thickness. Temp., 70°C. LLP, Δp = 1.0 atm (□), LVP, 38% RH (△) and VVP, 38% RH (△) are selected for comparison.

A comparison between the three types of water permeation is summarized as the following:

a. LVP fluxes are observed to be ~7 times larger than VVP fluxes, regardless of membrane thickness.

b. The order of increasing water permeation is as follows (using Δp=1.0 atm for LLP as a point of comparison.):

   i. LLP < VVP < LVP, for thicknesses > 28 μm.

   ii. VVP < LLP < LVP, for thicknesses between 11 to 28 μm.

   iii. VVP < LVP < LLP, for thicknesses < 11 μm.

4.2.2 *In-situ* measurements of water permeation

4.2.2.1 Dry-anode/wet -cathode operating conditions

Polarization curves and cell resistances (R_{cell}) under dry-anode/wet-cathode conditions (*i.e.*, anode, 40% RH, T_{dp} = 50^{o}C and cathode, >100% RH, T_{dp} = 75^{o}C) are presented in Figure 4-4(a). The corresponding iR-corrected polarization curves are shown in Figure 4-4(b).

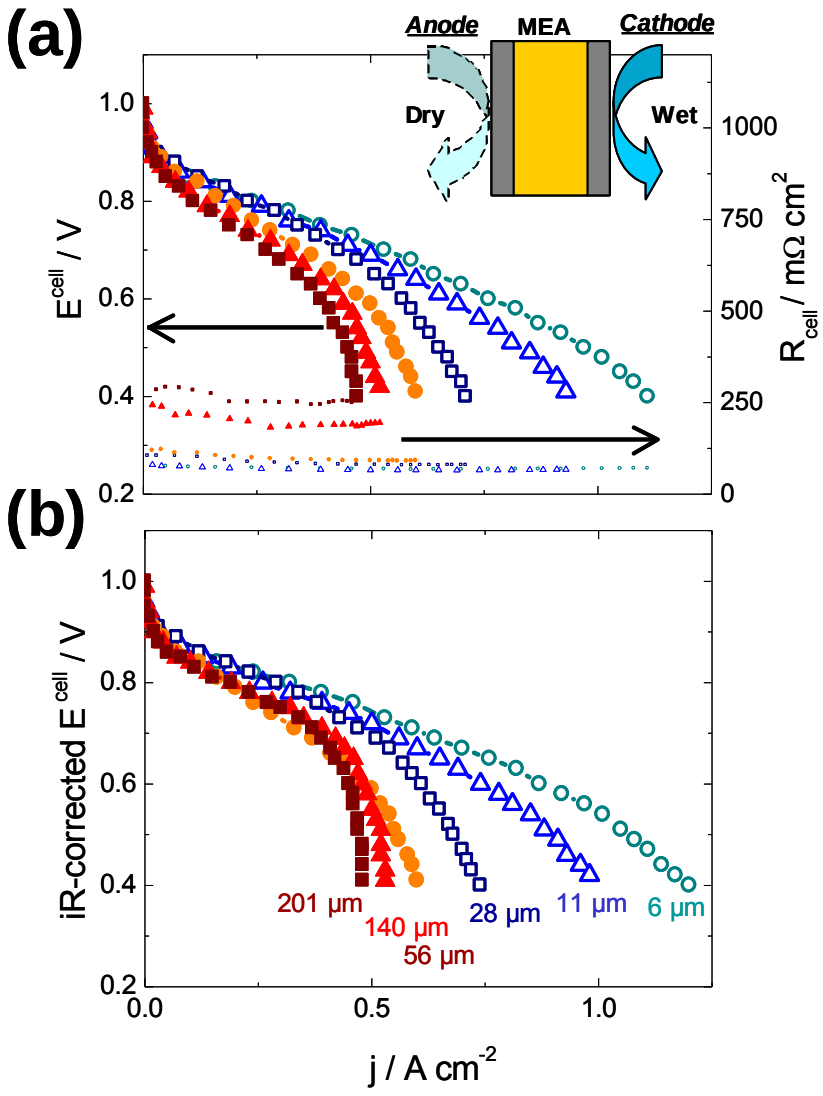

Figure 4-4 **(a) Polarization curves and cell resistances (R_{cell}) obtained under RH_{anode} = 40%, $RH_{cathode}$ > 100 %, ambient pressure at the outlets. Cell temperature, 70°C. Humidified H_2 and air supplied in a stoichiometric ratio 2.0 and 3.0. (b) Corresponding iR-corrected polarization curves. Membrane thicknesses: 6 μm(○), 11 μm(△), 28 μm(□), 56 μm(●), 140 μm(▲) and 201 μm(■).**

Figure 4-4(a) shows the improvement in fuel cell performance with decreasing membrane thickness. For example, the current density at 0.6 V increases from 0.39 to 0.76 A cm^{-2} when the membrane thickness is reduced

from 201 μm to 6 μm, while R_{cell} values are 244 and 66 mΩ cm^2, for 201 μm and 6 μm thick membranes, respectively. R_{cell} values are in the same range of those obtained under fully humidified conditions, 220 and 54 mΩ cm^2, respectively, which, implies membrane dehydration is insignificant under these conditions. Improvements in performances are even more pronounced for thinner membranes in the high current density regime.

The net water fluxes through the operating fuel cell are shown in Figure 4-5. The *in-situ* net water flux (J_{NET}) represents the sum of the fluxes due to EOD (J_{EOD}) and back permeation of water (J_{WP}). (*c.f.*, Equation 2-12) The negative water fluxes correspond to net water transport towards the anode and is attributable to back permeation. The increasingly negative net water flux observed for decreasing membrane thicknesses implies that the back permeation of water (J_{WP}) increases with decreasing membrane thicknesses.

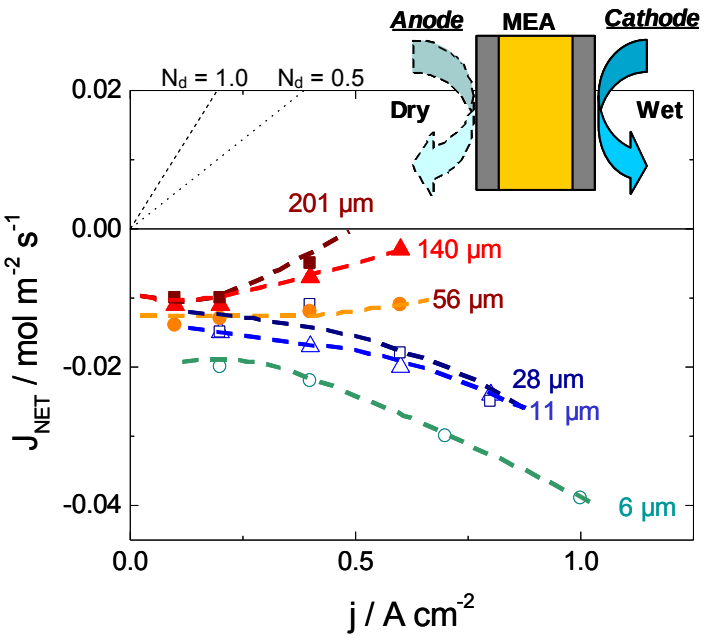

Figure 4-5 ***In-situ*** **net water fluxes (J_{NET}) as a function of current density (j) under the dry-anode/wet-cathode condition. Dashed lines indicate the calculated EOD flux (J_{EOD}) for N_d = 0.5 (···) and 1.0 (---). Membrane thicknesses: 6 µm(○), 11 µm(△), 28 µm(□), 56 µm(●), 140 µm(▲) and 201 µm(■).**

Addition to the analysis in Chapter 3, averaged RHs (*c.f.*, section 2.4.4) of the anode and cathode streams are taken into account. The relative humidities of the anode and cathode gases introduced to the fuel cell were 40 and >100% RH, respectively. While the average RH at the cathode was >100%, the average RH at the anode varied according to the magnitude and the direction of the net water flux. (see section 2.4.4 for the definition of "average RH") In the case of membranes 201 to 56 µm thick, the average RH of the anode was 40 - 59% for current densities up to 0.4 A cm^{-2}. In the case of 28 to 6 µm thick membranes, the average RH of the anode increased from 40% to 74%, for current densities up to 0.8 A cm^{-2}. In both cases, the anode is largely below saturation point, from

which the membranes are assumed to be exposed to water vapour at the anode but in contact with liquid water at the cathode. Thus, liquid-vapour permeation (LVP) is most likely the mode of water permeation for the back transport of water under these operating conditions.

In the discussion on NRE211 membrane (*c.f.*, section 3.2.2.2), N_d was taken as 0.5. A similar estimation of N_d was used to conduct a case study. At a current density of 0.4 A cm^{-2}, the EOD flux (J_{EOD}) towards the cathode is calculated to be 0.021 mol m^{-2} s^{-1}, from which the back permeation fluxes (J_{WP}) for 201, 140 and 56 μm thick membranes are estimated to be 0.026, 0.029 and 0.033 mol m^{-2} s^{-1}, respectively (*c.f.*, Equation 2-12). Since the average RH of the anode was found to be 49 - 59% at 0.4 A cm^{-2}, this permeation flux corresponds to an *ex-situ* LVP measurement under conditions of liq./PEM/49% RH to liq./PEM/59% RH. The *ex-situ* LVP flux of 201, 140 and 56 μm thick membranes, under the LVP conditions of liq./PEM/59% RH (extrapolated from the obtained LVP fluxes) are 0.058, 0.075 and 0.091 mol m^{-2} s^{-1}, respectively. These values are sufficiently large to account for the rates of back permeation measured *in-situ* through fuel cells (LVP fluxes under liq./PEM/49% RH are even larger, see Figure 4-2(a)). In contrast, the rates of LLP and VVP, measured *ex-situ*, are insufficient to account for the rates of back permeation as illustrated by the following: the average pressure of the cathode is +0.025 atm with respect to the anode, due to the difference in supplied gas flow rates. This small pressure difference would provide back permeation fluxes measured *ex-situ* (LLP fluxes at Δp=0.025 atm) of 5.8 x 10^{-5}, 9.7 x 10^{-5} and 3.3 x 10^{-4} mol m^{-2} s^{-1} for 201, 140 and

56 μm thick membranes, respectively. These are insignificant in relation to the estimated back permeation fluxes (J_{WP}) during fuel cell operation: which were 0.026, 0.029 and 0.033 mol m^{-2} s^{-1} for 201, 140 and 56 μm thick membranes, respectively. Similarly, the maximum VVP fluxes obtained *ex-situ* (under conditions of 96% RH/PEM/38% RH) for 201, 140 and 56 μm thick membranes are 0.013, 0.015, 0.021 mol m^{-2} s^{-1}, respectively, which alone could not account for the rates of back permeation flux estimated *in-situ*.

For thinner membranes (28 to 6 μm thick), the fluxes of back permeation of water (J_{WP}) are estimated to be 0.049, 0.051 mol m^{-2} s^{-1} for 28 μm and 11 μm thick membranes at 0.6 A cm^{-2}, and 0.066 mol m^{-2} s^{-1} for 6 μm thick membrane at 0.7 A cm^{-2}, respectively (*c.f.*, Equation 2-12). The magnitudes of the back permeation fluxes (J_{WP}) are approximately double those estimated for membranes >56 μm thick. The average RH of the anode under these conditions ranges from 67 to 74%, in which the membranes are assumed to be in contact with liquid water at the cathode, and water vapour *and* liquid water at the anode (because when the average RH exceeds 70%, the RH at the outlet is over the saturation point, under this condition). LVP fluxes under similar conditions, liq./PEM/70% RH (extrapolated from the obtained LVP fluxes), for membranes 28 to 6 μm thick range from 0.067 to 0.074 mol m^{-2} s^{-1}, which are sufficient to account for the estimated rates of back permeation. The average gas pressure difference between the cathode and the anode was measured to be 0.029 atm, which can create LLP fluxes up to 0.0011, 0.0051 and 0.018 mol m^{-2} s^{-1}, for 28, 11 and 6 μm thick membranes, respectively. These represent 2%, 10% and 27%

of the estimated back permeation flux, respectively, indicating that LLP cannot be completely ruled out as a mode of back permeation although it appears not to be the dominant mode of water permeation. VVP is discounted as a possible mode of back permeation because the maximum VVP flux observed, *ex-situ*, under similar conditions is ~0.021 mol m^{-2} s^{-1}.

4.2.2.2 Dry operating conditions

Polarization curves and cell resistances (R_{cell}) under dry conditions (*i.e.*, anode and cathode, 18% RH, T_{dp} = 35^{o}C) are presented in Figure 4-6(a) and the corresponding iR-corrected polarization curves are shown in Figure 4-6(b).

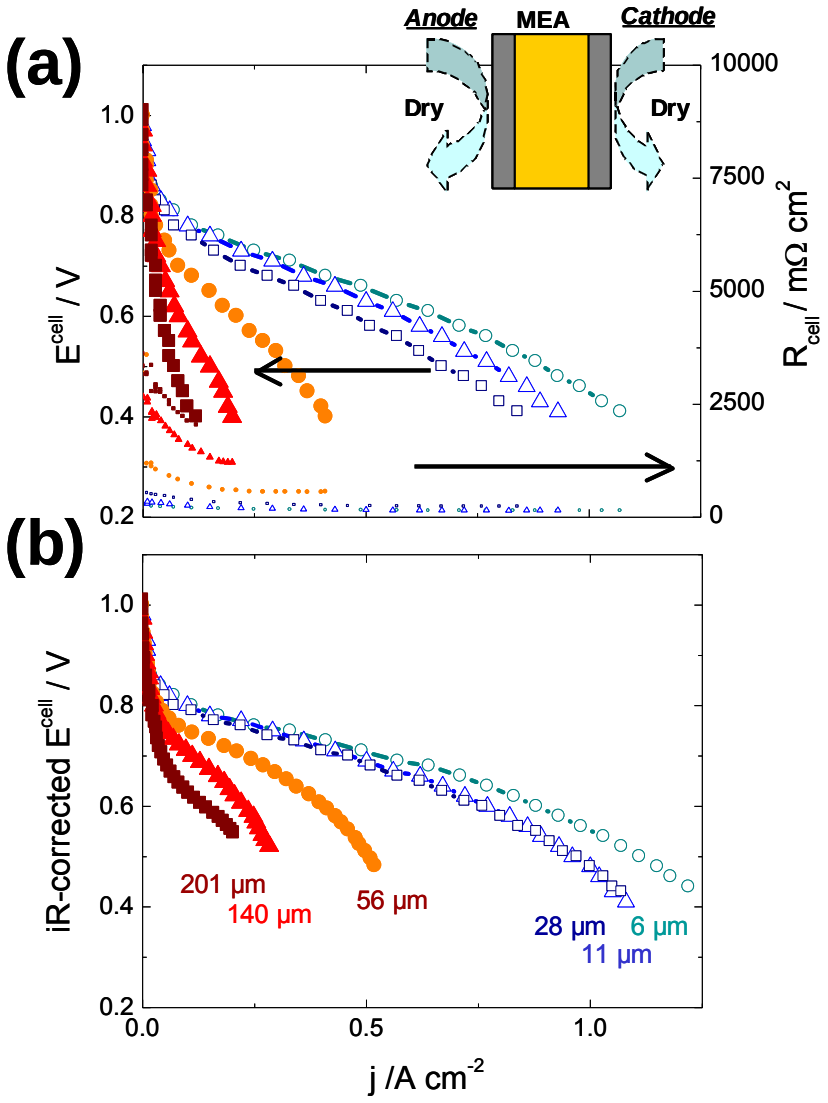

Figure 4-6 **(a) Polarization curves and cell resistances (R_{cell}) obtained under RH_{anode} = $RH_{cathode}$ = 18 %, ambient pressure at the outlets. Cell temperature, 70°C. Humidified H_2 and air supplied in a stoichiometric ratio 2.0 and 3.0. (b) Corresponding iR-corrected polarization curves. Membrane thicknesses: 6 µm(○), 11 µm(△), 28 µm(□), 56 µm(●), 140 µm(▲) and 201 µm(■).**

Figure 4-6(a) shows the significant improvements in fuel cell performance with decreasing membrane thickness. For example, the current density at 0.6 V increases from 0.04 to 0.64 A cm^{-2} when the membrane thickness is reduced

from 201 to 6 μm, while R_{cell} values are 2750 and 138 mΩ cm^2 for 201 and 6 μm thick membranes, respectively. R_{cell} values are found to be an order of magnitude larger for 201 μm thick membranes and 2–3 times larger for 6 μm thick membranes compared to R_{cell} values obtained under fully humidified conditions, which indicates that membrane dehydration is significant under these conditions.

Similarly, the net water flux through the operating fuel cell is shown in Figure 4-7. Net water fluxes are near zero (±0.001 mol m^{-2} s^{-1}) for membranes ranging in thickness, 201 to 56 μm; whereas increasingly negative water fluxes (0.004 to 0.013 mol m^{-2} s^{-1}) are found for membranes ≤28 μm, which confirms that the back permeation of water (J_{WP}) increases with decreasing membrane thicknesses.

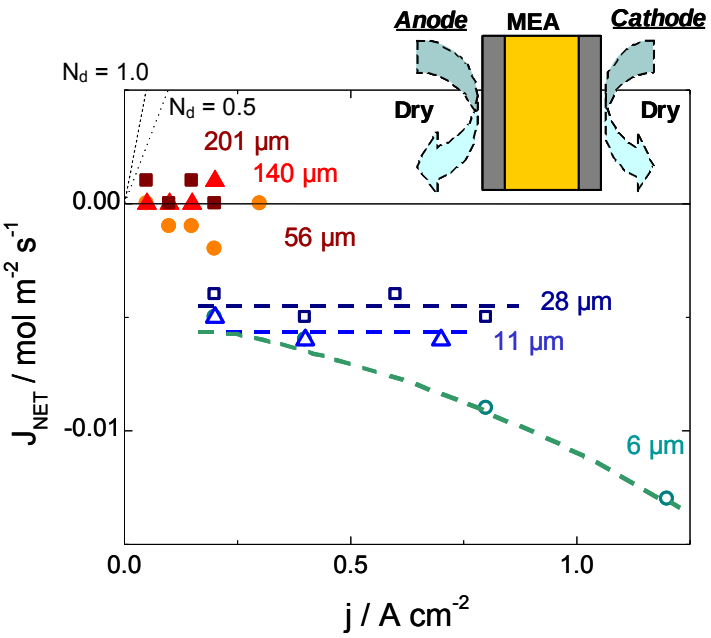

Figure 4-7 ***In-situ*** **net water fluxes (J_{NET}) as a function of current density (j) under the dry condition. Dashed lines indicate the calculated EOD flux (J_{EOD}) for N_d = 0.5 (···) and 1.0 (---). Membrane thicknesses: 6 µm(○), 11 µm(△), 28 µm(□), 56 µm(●), 140 µm(▲) and 201 µm(■).**

The RH of the anode and cathode gases introduced to the fuel cell were 18%. Under these conditions, both RH values of the anode and the cathode vary according to the net water flux. In the case of membranes, 201 to 56 µm thick, the average RH values of anode and cathode increased to 23% and 40%, respectively, for current densities up to 0.2 A cm^{-2}. In these cases, the anode and cathode streams are prevalently below saturation, which suggests that the membranes are exposed to water vapour on both sides. Thus, vapour-vapour permeation (VVP) is expected to be the dominant mode of water permeation for the back transport of water, under these operating conditions.

Assuming an N_d value of 0.5, for reasons previously discussed (*c.f.*, section 3.2.2.2), and taking a current density of 0.2 A cm^{-2}, the EOD flux (J_{EOD}) towards the cathode is calculated to be 0.010 mol m^{-2} s^{-1}, from which the back permeation fluxes (J_{WP}) for 201, 140 and 56 μm thick membranes are estimated to be 0.010, 0.011 and 0.012 mol m^{-2} s^{-1}, respectively. Unfortunately, the *ex-situ* VVP setup did not allow the measurement of water permeation under conditions of reduced RH on both sides of the membrane. However, the magnitudes of back permeation fluxes estimated *in-situ* coincide with the range of VVP fluxes obtained *ex-situ* (*c.f.*, Figure 4-2(b)).

In the case of thinner membranes (≤28 μm), back permeation fluxes (J_{WP}) are estimated to be 0.035 mol m^{-2} s^{-1} for 28 μm thick membranes at 0.6 A cm^{-2}, 0.038 mol m^{-2} s^{-1} for 11 μm thick membranes at 0.7 A cm^{-2}, and 0.051 mol m^{-2} s^{-1} for 6 μm thick membranes at 0.8 A cm^{-2}. The magnitudes of the back permeation fluxes (J_{WP}) are ~3 to 5 times larger than those for the thicker membranes (*i.e.*, those >56 μm). The maximum VVP flux, measured *ex-situ*, for these membranes is ~0.021 mol m^{-2} s^{-1}, which is insufficient to completely account for the measured rate of back permeation; whereas the corresponding *ex-situ* LVP fluxes under conditions of liq./PEM/38% RH is ~0.15 mol m^{-2} s^{-1}. While the average RH values for the anode under these conditions were found to be in the range of 26 - 33%, the RH values for the cathode were found to be in the range of 33 - 37%, respectively. Although the cathode gases were found below saturation, we assert the membranes are in contact with water vapour *and* liquid water at the

cathode under this high current density regime, due to the magnitude of the estimated rate of back permeation.

Negative *in-situ* net water fluxes (J_{WP}) were observed to increase dramatically in the case of 6 μm thick membrane. At 1.2 A cm^{-2} the net *in-situ* water flux (J_{NET}) was found to be -0.013 mol m^{-2} s^{-1}, from which it is estimated that the back permeation flux (J_{WP}) is 0.075 mol m^{-2} s^{-1}, assuming N_d = 0.5. In the absence of physical pressure, this relatively large back permeation flux (J_{WP}) can only be accounted for by LVP. The average RH of the anode was estimated to be ~20 % RH and if the membrane is in contact with liquid at the cathode at this high current density regime, the corresponding maximum LVP flux (J_{LVP}), 0.15 mol m^{-2} s^{-1}, obtained *ex-situ*, under the conditions of liq./PEM/38%RH, is sufficient to account for the rate of back permeation (J_{WP}). Additionally, although the anode is below saturation point, partial hydraulic pressure driven LVP may occur since the average gas pressure difference between the cathode and the anode was measured to be 0.041 atm, which is sufficient to create a LLP flux of 0.025 mol m^{-2} s^{-1} for 6 μm thick membranes. This corresponds to ~1/3 of the estimated back permeation flux, which cannot be neglected.

These quantitative case studies on back permeation of water under two operating conditions were conducted assuming an EOD coefficient of N_d = 0.5. However, similar observations were found when N_d = 1.0 was assumed. When N_d = 1.0, the EOD flux towards the cathode double from when N_d = 0.5, but further reduction of the RH at the anode and the formation of the liquid/membrane interface at lower current density initiated LVP type back

permeation of water. The corresponding fluxes of water were also found sufficient to account for the estimated rates of back permeation.

4.3 Discussion

4.3.1 Water transport resistances ($R_{interface}$ and $R_{internal}$) and the water balance limiting current density (j_{MAX})

In order to examine the relative importance of *interfacial* and *internal* water transport to the membrane's permeability to water, an approach similar to Aotani et al.[63,132] was taken to ascribe water transport resistances corresponding to liquid-liquid permeation (R_{LLP}), liquid-vapour permeation (R_{LVP}) and vapour-vapour permeation (R_{VVP}):

$$R_{LLP} = \frac{\Delta\mu_{LLP}}{J_{LLP}} \quad \text{Equation 4-1}$$

$$R_{LVP} = \frac{\Delta\mu_{LVP}}{J_{LVP}} \quad \text{Equation 4-2}$$

$$R_{VVP} = \frac{\Delta\mu_{VVP}}{J_{VVP}} \quad \text{Equation 4-3}$$

where J and Δμ represent the water permeation flux and the corresponding chemical potential difference leading to water permeation.

In Figure 4-8, water transport resistances for LLP, LVP and VVP are presented as a function of the wet membrane thickness. The resistances decrease in the order VVP > LVP > LLP, which is consistent with the increasing hydration state of the membrane[89,130] and the reduction in number of vapour/membrane interfaces.[25] Transport resistance decreases with decreasing

membrane thickness. The water transport resistance unit presented, 1.0 kJ m^2 s mol^{-2}, is equivalent to 1.1 mΩ cm^2. (*Note*: 1 Ω = 1 J A^{-2} s^{-1} = 1 J s C^{-2}), The protonic transport resistance through a fully hydrated 28 μm thick Nafion® is calculated to be 28 mΩ cm^2, based on the specific conductivity of 0.1 S cm^{-1}. (*Note*: R_{cell}, obtained *in-situ*, under fully humidified conditions is in the same order of magnitude (*c.f.*, section 4.2.2.1).) Although the driving forces and the transport mechanisms of water and proton may differ, the transport resistance of water through 28 μm thick Nafion® under LLP condition is found to be 2 to 3 orders of magnitude smaller than the transport resistance of proton.

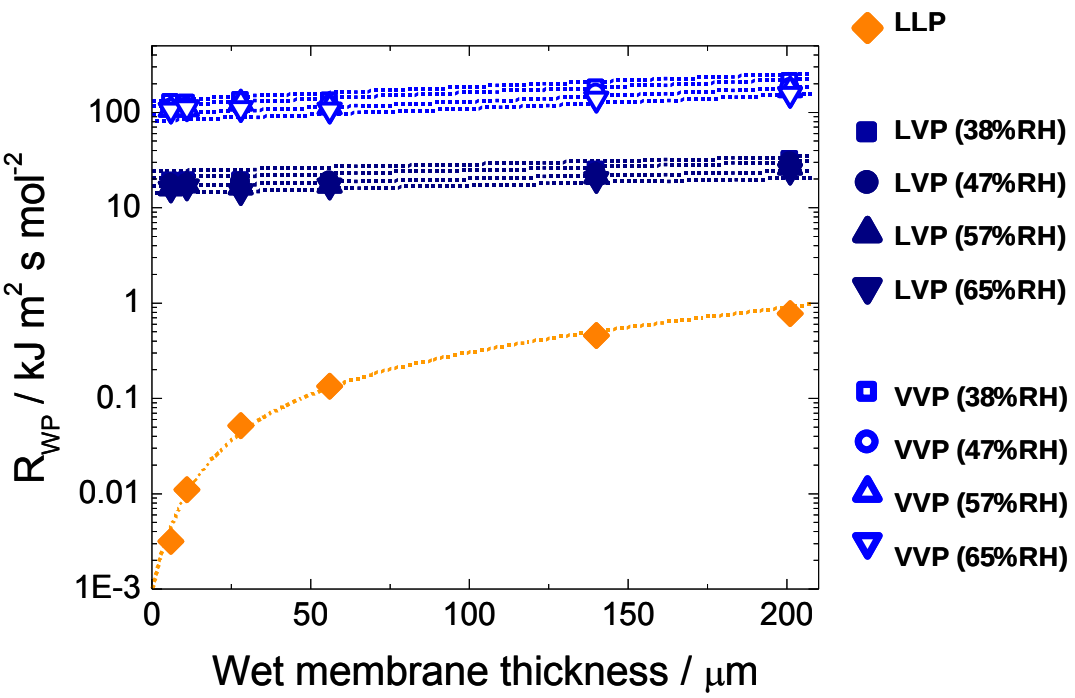

Figure 4-8 **Water permeation resistance (R_{WP}) of Nafion® versus wet membrane thickness at 70°C. LLP(◆), LVP-38% RH(■), LVP-47% RH(●), LVP-57% RH(▲), LVP-65% RH(▼), VVP-38% RH(□), VVP-47% RH(○), VVP-57% RH(△) and VVP-65% RH(▽).**

The *interfacial* water transport resistance at the membrane/liquid water interface is considered negligible.[126] Thus, R_{LLP} is primarily the *internal* water transport resistance; R_{LVP} consists of an *internal* transport resistance ($R_{LVP\_internal}$) and a transport resistance at the water egressing side corresponding to the membrane/vapour interface ($R_{LVP\_interface}$); and R_{VVP} consists of an *internal* transport resistance ($R_{VVP\_internal}$) and two *interfacial* membrane/vapour transport resistances ($R_{interface}$).

R_{LVP} and R_{VVP} extrapolated to zero-thickness provide the *interfacial* water transport resistance ($R_{interface}$). *Internal* water transport resistances ($R_{internal}$) are estimated by subtracting $R_{interface}$ from R_{LVP} and R_{VVP}. Figure 4-9 summarizes $R_{interface}$ and $R_{internal}$ for LVP and VVP for different thicknesses of Nafion. For all cases, $R_{interface}$ and $R_{internal}$ decrease with increasing RH, which is consistent with the increasing hydration state of the bulk and the surface of the membrane.[63,89,130,133] $R_{internal}$ for LVP was found to be ~1/5 of $R_{internal}$ for VVP, presumably due to the higher hydration state of the membrane at LVP. A large difference between LVP and VVP is observed for $R_{interface}$. For instance, $R_{interface}$ for VVP and LVP for 201 μm thick membranes at 38% RH is 118 and 17.8 kJ m^2 s mol^{-2}, respectively. $R_{interface}$ for VVP consists of ingressing and egressing transport resistances at the membrane/vapour interfaces; whereas $R_{interface}$ for LVP is due to the egressing transport at the membrane/vapour interface only. A large $R_{interface}$ for VVP in comparison to $R_{interface}$ for LVP may also be attributed to the difference in hydration of the membrane surface. Indeed, AFM studies of Nafion® membrane surfaces reveal an increase in hydrophilic domain size with increasing RH.[89,133]

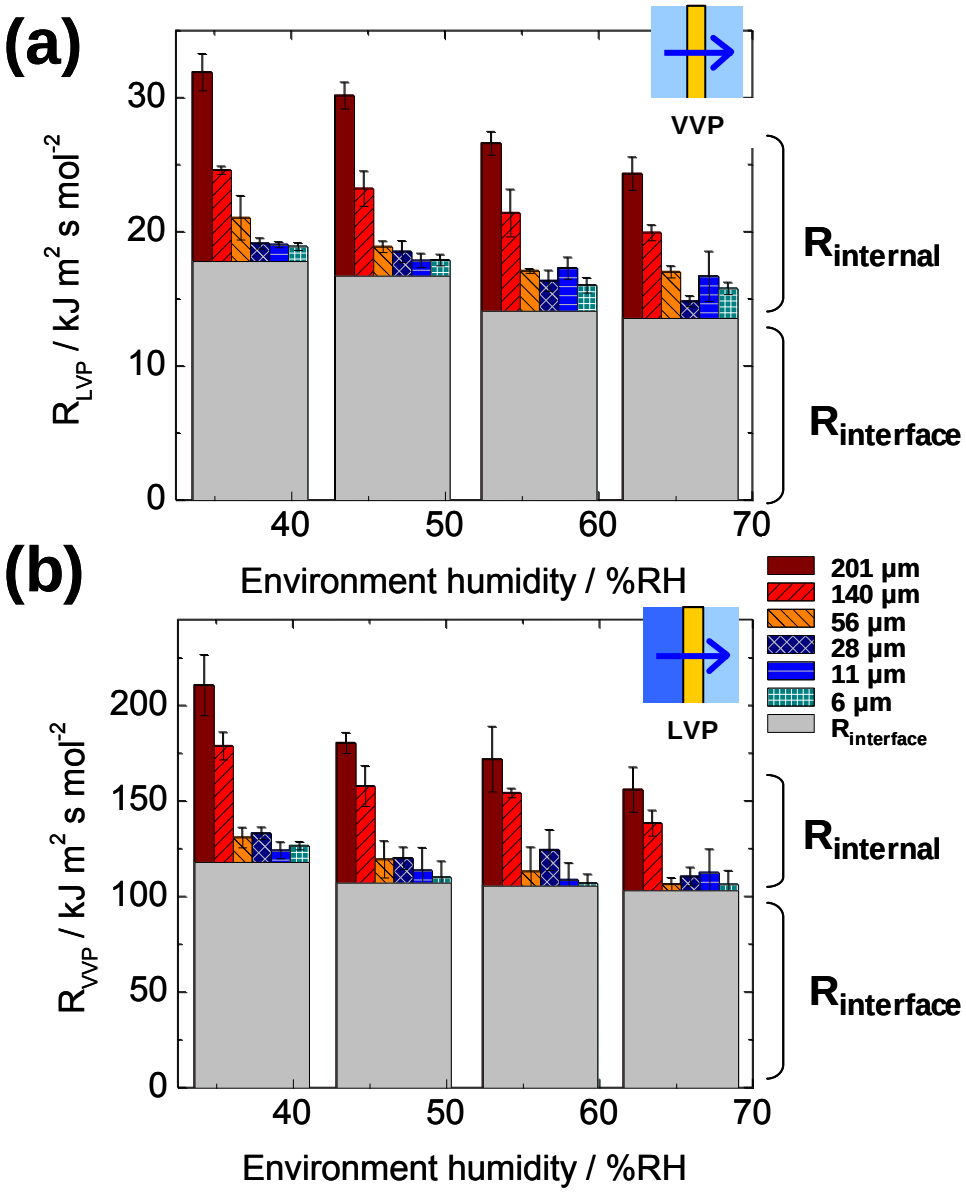

Figure 4-9 Interfacial and internal water transport resistances ($R_{interface}$ and $R_{internal}$) of (a) LVP and (b) VVP of Nafion® at 70°C.

In the case of LVP, the ratio of *interfacial* water transport resistance to the *total* water transport resistance ($R_{LVP\_interface}/R_{LVP}$) is 0.53 – 0.56 (depending on RH) for 201 μm thick membranes and 0.86 – 0.94 for 6 μm thick membranes. In

the case of VVP, $R_{VVP\_interface}/R_{VVP}$ is 0.56 – 0.66 (depending on RH) for 201 μm thick membranes and 0.93 – 0.99 for 6 μm thick membranes. In both cases, the contribution of *interfacial* water transport resistance is more than half of the *total* water transport resistance for 201 μm thick membrane and is found to increase substantially with decreasing membrane thickness to the point that the *interfacial* resistance dominates the transport resistance.

The interplay between water transport resistances and the chemical potential difference across the membrane determine the water permeation flux. The *total* water transport resistances for VVP and LVP are in the range of 110 - 210 and 15 - 32 kJ m^2 s mol^{-2}, respectively; while water transport resistance of LLP is in the range of 0.0032 - 0.78 kJ m^2 s mol^{-2}. The water transport resistances of VVP and LVP are ~2 - 5 orders of magnitudes larger than that of LLP. The water transport resistances of VVP and LVP decrease with membrane thickness but are limited by the *interfacial* water transport resistance, which is the major component regardless to the membrane thickness; the water transport resistance of LLP decreases with decreasing membrane thickness. In this work, the chemical potential differences created across the membrane during VVP and LVP lie in the range 0.37 to 2.9 kJ mol^{-1}; while the chemical potential difference created across the membrane under LLP conditions of Δp=1.0 atm is 0.0020 kJ mol^{-1}. The magnitudes of chemical potential differences created across the membrane under VVP and LVP conditions are thus ~3 orders larger than LLP, however, the larger *interfacial* water transport resistance limits the water permeation even for ultra-thin membranes, while in the case of LLP, small

chemical potential differences are sufficient to efficiently drive water through thin membranes.

The water balance across the MEA influences the performance of the fuel cell, thus it is useful to determine the balance point between membrane's water permeation flux and the EOD flux is useful. The EOD flux (J_{EOD}), is a function of the current density (j), which can be calculated according to Equation 2-11. The current density at the balance point is defined as the maximum current density (j_{MAX}) when *in-situ* net water flux (J_{NET}) is zero. When the operating current density exceeds j_{MAX}, the *in-situ* net water flux is positive (*i.e.*, net water flux towards cathode) and may lead to flooding or dehydration within the MEA. The water balance-derived maximum current density (j_{MAX}) is described according to Equation 4-4:

$$j_{MAX} = \frac{F}{N_d} J_{WP}(t, \Delta\mu) \quad \text{.....Equation 4-4}$$

where F, N_d and J_{WP} represent Faraday's constant, the EOD coefficient, and the water permeation flux, which is obtained experimentally and a function of the membrane thickness (t) and the differential chemical potential (Δμ), respectively. The water permeation fluxes (J_{WP}) through Nafion® membranes under LLP, LVP and VVP are taken from Figure 4-1, Figure 4-2(a) and (b). For LLP, water permeation fluxes at differential pressure of 1.0 and 0.1 atm are taken; for LVP and VVP, the maximum and the minimum water permeation fluxes obtained in this work are taken as those measured where the dry side is 38% and 85% RH, and are shown in Figure 4-10. Assuming a N_d value of 0.5 as an example, at

70°C, the water balance maximum current densities were estimated to be: 0.004, 1.8, and 0.2 A cm^{-2}, respectively, for LLP (at Δp = 1.0 atm)-, LVP (at 38% RH)- and VVP (at 38% RH)-type back permeation of water through 201 μm thick membranes; 0.7, 2.9, and 0.4 A cm^{-2}, respectively, through 28 μm thick membranes; and 12, 3.0, and 0.4 A cm^{-2}, respectively, through 6 μm thick membranes. This further illustrates the advantage of LVP for thick membranes (>28 μm) and LLP for thin membranes (≤11 μm), as discussed in section 4.2.1.

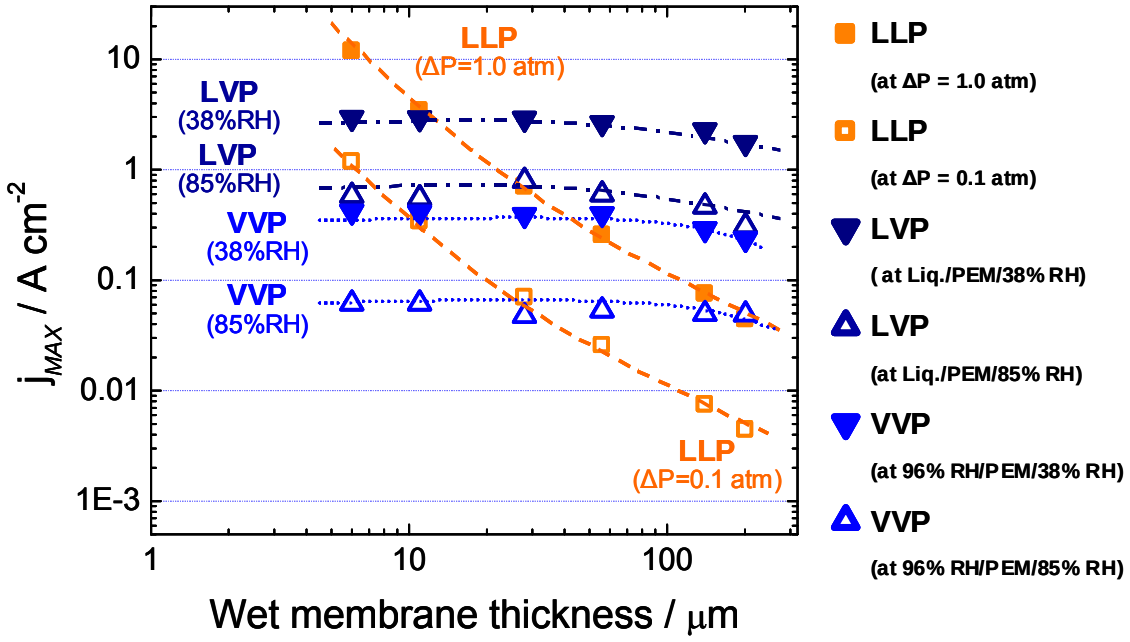

Figure 4-10 Estimated maximum current densities versus wet membrane thickness at 70°C. j_{MAX} is the current when the *in-situ* net water flux is zero for an EOD flux (J_{EOD}) calculated with N_d = 0.5. Water permeation fluxes (J_{WP}) are obtained from the *ex-situ* measurements in this work. The types of water permeation and the range of driving forces are shown in the legend

Furthermore, from the perspective of enhancing the back permeation of water, except where the membranes are exposed to liquid on both sides (LLP),

reducing the thickness below ~50 μm does not provide any advantage in performance. This is true, even when the EOD coefficients were nominally varied from 0.3 to 3.0 (*c.f.*, Figure 4-11). This is because interfacial resistance dominate water permeation through thin membranes. Another feature extracted from Figure 4-10 is that LVP, which will most likely be the mode of water permeation at high current density operation, is able to maintain a water balance up to 3 A cm^{-2} (at N_d = 0.5 and if the RH of the anode is low). Of course, these assertions do not take into account the role of proton resistance on fuel cell performance. Finally, this analysis illustrates that if the liquid water is not in contact with any side of the membrane, then water permeability is significantly affected, leading to limiting feasible fuel cell currents to well below 1.0 A cm^{-2}. This may exlain why fuel cell performances at elevated temperatures (*i.e.*, >120^{o}C) are modest: back permeation of water from the cathode to anode is severely compromised.[134,135]

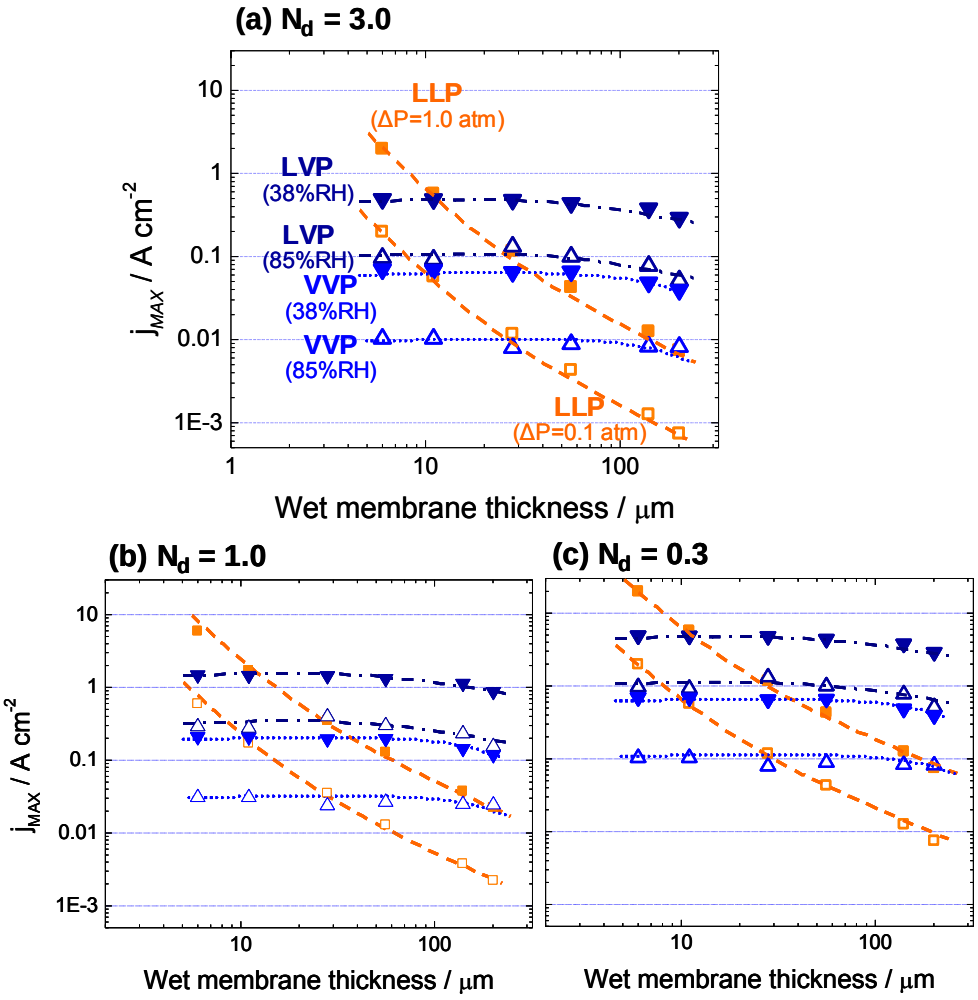

Figure 4-11 Estimated maximum current densities versus wet membrane thickness at 70°C. j_{MAX} is the current when the net water flux is zero for an EOD flux (J_{EOD}), calculated with: (a) N_d = 3.0, (b) N_d = 1.0 and (c) N_d = 0.3. Water permeation fluxes (J_{WP}) are obtained from the *ex-situ* measurements in this work. The types of water permeation and the range of driving forces are shown in the legend.

4.4 Conclusion

Ex-situ measurements of liquid-liquid permeation (LLP), liquid-vapour permeation (LVP) and vapour-vapour permeation (VVP) fluxes of water reveal the effect of reducing the membrane thickness. Water permeation fluxes under

LLP conditions increase with decreasing membrane thickness. Water permeation fluxes under LVP and VVP conditions initially increase with decreasing membrane thickness (to 56 μm), but change little for further decreases in thickness.

The following trends are found for water permeation fluxes: (i) $J_{LVP} > J_{VVP} > J_{LLP}$ for membranes ≥56 μm; (ii) $J_{LVP} > J_{LLP} > J_{VVP}$ for membranes ranging 11 – 28 μm; (iii) $J_{LLP} > J_{LVP} > J_{VVP}$ for membranes ≤11 μm. The trends suggest that concentration gradient-driven water permeation is effective for thicker membranes; while pressure gradient-driven water permeation is effective for ultra-thin membranes.

Internal and *interfacial* water transport resistances for Nafion® are estimated for the three types of water permeation. The ratio of *interfacial* transport resistance over *total* transport resistance for vapour-vapour permeation (VVP) is determined to be ~0.61 for 201 μm membranes and ~0.96 for 6 μm membranes, respectively. The same ratio for liquid-vapour permeation (LVP) is ~0.55 for 201 μm and ~0.90 for 6 μm membranes, respectively. The contribution of *interfacial* water transport resistance to the *total* water transport resistance is significant and found to increase with a reduction in membrane thickness. The *interfacial* resistance is negligible when the membrane is exposed to liquid on both sides, *i.e.*, LLP. The hydraulic pressure driven water transport rates increases dramatically for ultra-thin membranes.

It is generally known that back permeation helps mitigate water accumulation at the cathode and/or membrane dehydration at the anode during

the operation of a fuel cell. For the two operating conditions discussed, fuel cell performance improves with decreasing membrane thickness. Under dry-anode/wet-cathode operating conditions, liquid-vapour permeation (LVP) is considered the prevalent means for back permeation of water, regardless of membrane thickness. In the case of ultra-thin membranes (28 to 6 μm), further increases in the rate of back permeation are observed, which may be attributed to the assistance of small hydraulic pressures across these thin membranes. Under dry operating conditions, in the low current density regime, vapour-vapour permeation (VVP) was found to be prevalent for the back permeation of water through membranes, regardless of membrane thickness. Higher current densities (≥0.6 A cm^{-2}) under dry conditions are only achieved for thin membranes (6 to 28 μm), which are presumably due to the formation of a liquid/membrane interface at the cathode, leading to enhanced back permeation of water. The rate of back permeation increases further as the thicknesses of the membranes is reduced to 6 μm, possibly due to the increasing influence of hydraulic pressure driven water permeation.

Estimation of the maximum current that a given water transport process can support, *i.e.*, when the net water flux is zero, illustrates the effectiveness of LLP for thin membranes (≤11 μm). However, PEM fuel cells will normally be operated under conditions where the back permeation of water will be dominated by LVP; LVP alone will not significantly enhance the back permeation of water when reducing the membrane thickness below ~50 μm, because interfacial transport becomes dominant. In the case where fuel cells are operated under

VVP water fluxes, *e.g.*, at low RH and/or elevated temperatures, water permeation (from cathode to anode) is severely compromised to the point that fuel cell performance is also compromised.

CHAPTER 5 WATER PERMEATION THROUGH CATALYST-COATED MEMBRANES*

5.1 Introduction

Ex-situ studies of water permeation through Nafion® membranes reveal the importance of water vapour transport at the membrane interfaces.[25,84,86,88,126] In the previous chapters, it is found that water permeation through membranes exposed to liquid water on one side and non-saturated vapour on the other is much larger than for membranes exposed to a differential water vapour pressure. Hydraulic pressure-driven water permeation, *i.e.*, water permeation when the membrane is exposed to liquid water on both sides, is generally greater than membranes exposed to vapour on both sides, but smaller for membranes exposed to liquid water on one side and water vapour on the other (*c.f.*, section 3.2.1).

A catalyst layer comprises of carbon-supported Pt particles and proton conducting ionomer. In the absence of free-standing catalyst layers, experimental measurements of water permeation through catalyst layers is difficult, and thus rely on theoretical and empirical models based on mass transport phenomena through porous media.[136-140] Diffusivity of water vapour in catalyst layers is reported to be few orders of magnitude larger than liquid water

---

*Sections of this work have been published in:
Electrochemical and Solid-State Letters, M. Adachi, T. Romero, T. Navessin, Z. Xie, Z. Shi, W. Mérida and S. Holdcroft 13, 6 (2010)

in Nafion.[64,65,84,107,114,141-145] However, since sorption and desorption of water at the membrane interface significantly influences the permeability of the membrane to water, it is not unreasonable to conjecture that a catalyst layer might influence water sorption and desorption kinetics. For instance, hydrophilic nano-pores in the catalyst layer may facilitate condensation of water at the membrane surface due to a capillary effect[19,21], which may lead to enhanced water transport (*i.e.*, LVP); or the catalyst layer may change the area of the ionomer-water interface. The influence of catalyst layers on the water permeability of membranes is the topic of this work. Water permeation is measured on pristine membranes (NRE211), half-catalyst-coated membranes ($hCCM_s$) for which the CL is deposited on the water sorption side, half-catalyst-coated membranes ($hCCM_d$) for which the CL is deposited on the desorption side and catalyst-coated membranes (CCM) for which CLs are deposited on both sides. The acronyms and schematics of samples are shown in Figure 5-1, together with a TEM image of the PEM/CL interface, which shows the intimacy of contact between the two.

The following water permeation measurements were conducted:

a) Vapour-dry permeation (VDP), for which one side of the membrane is exposed to saturated water vapour, while dry helium gas is flowed over the other.[86,126]
b) Liquid-dry permeation (LDP), for which one side of the membrane is exposed to liquid water and dry helium gas is flowed over the other.[86]

c) Liquid-liquid permeation (LLP), for which both sides of the membrane are exposed to liquid water and water permeation is driven by a hydraulic pressure gradient.[25]

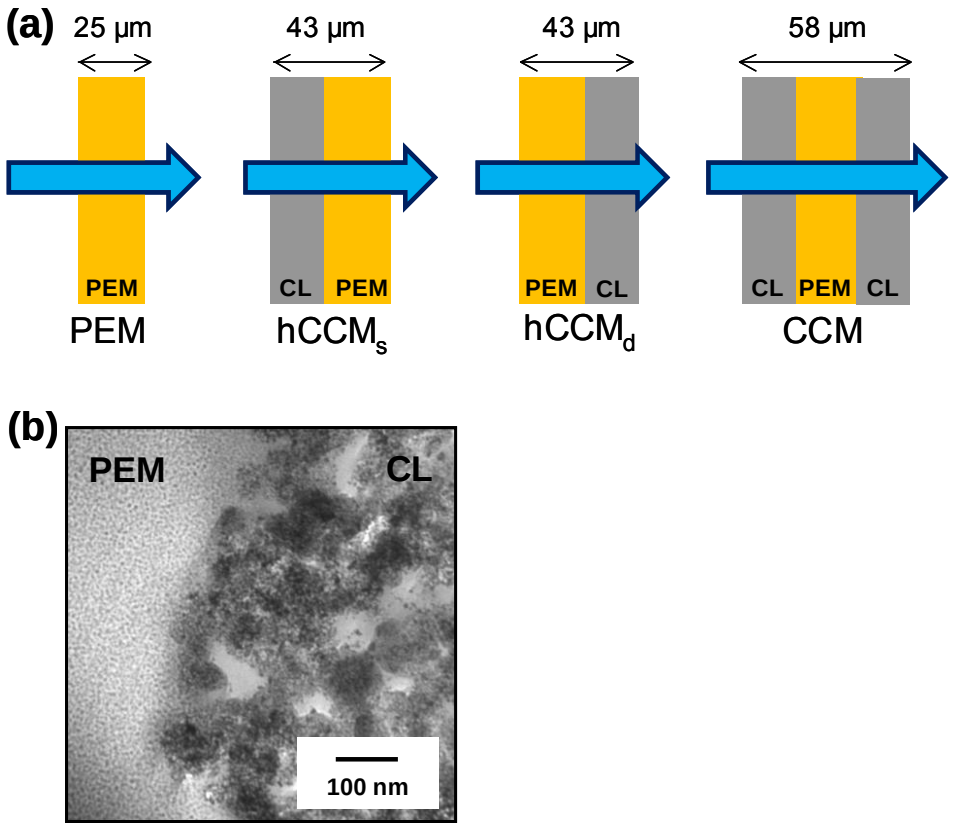

Figure 5-1 **(a) Schematic of the NRE211 and catalyst-coated membranes. PEM, pristine NRE211; hCCM$_s$, half-catalyst-coated membrane (catalyst layer upstream of water permeation); hCCM$_d$, half-catalyst-coated membrane (catalyst layer downstream of water permeation); CCM, catalyst-coated membrane. (b) TEM image of the membrane/catalyst layer interface.**

5.2 Results and discussion

5.2.1 Vapour-dry permeation (VDP)

Vapour-dry permeation fluxes of water through the membrane and catalyst-coated membranes are plotted against the flow rate of the carrier gas in Figure 5-2. VDP fluxes increase with flow rate, saturate, and gradually decrease

at higher flow rates. For flow rates between 30 -100 mL min^{-1}, the RH of the "dry side" was estimated to be 10 - 25% according to the dew point temperature. For higher flow rates, *i.e.*, 300 - 1000 mL min^{-1}, the RH of the "dry side" was 4 to 1 %. Increasing the flow rate reduces the RH on the "dry side" and increases the driving force for permeation across the membrane. The increase in water permeation flux under low flow rate (*i.e.*, <100 mL min^{-1}) is due to an increase in the water concentration gradient across the membrane. In the high flow rate regime, 300 - 700 mL min^{-1}, the reduced RH of the "dry side" may dehydrate the membrane interface and reduce the rate of water permeation.[86-88,115,126] The intermediate flow rate range (*i.e.*, 500 – 700 mL min^{-1}), within which fluxes are maximum, is representative of the relative rates of permeation in the absence of significant dehydration. Within all these flow rate regimes, no significant differences in water permeation were observed (< ±10%) between NRE211 and catalyst-coated membranes. The presence of the catalyst layer does not affect the rate of permeation, when deposited at the membranes' sorption or desorption interface, or both.

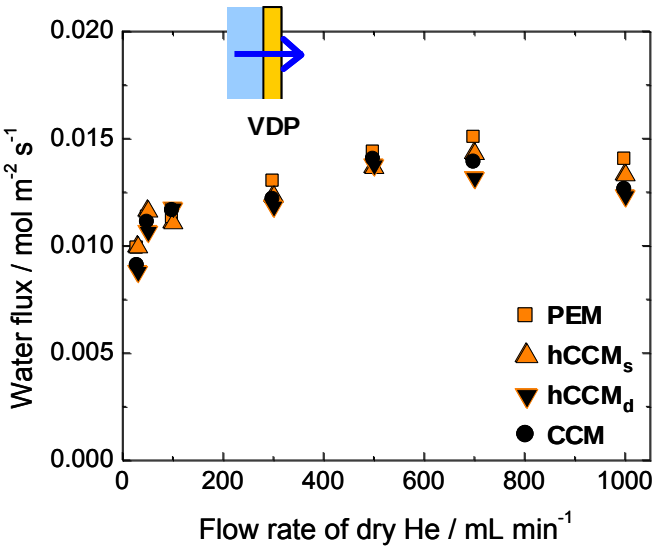

Figure 5-2 Vapour-dry permeation (VDP) fluxes through NRE211 and catalyst-coated membranes at 70°C. PEM(□), $hCCM_s$(△), $hCCM_d$(▼) and CCM(●).

5.2.2 Liquid-dry permeation (LDP)

LDP fluxes of water through the membrane and catalyst-coated membranes increase with increasing flow rate of the carrier gas, as shown in Figure 5-3. Similarly to the case of VDP, this is due to the decreasing RH of the "dry side", which increases the driving force for permeation. Since the LDP fluxes are 4 to 5 times larger than VDP, which is a consequence of having at least one liquid/membrane interface,[87,115] severe dehydration of the membrane on the "dry side" is less likely. Thus the flux did not reach a maximum within the flow rate studied. As with VDP measurements, the permeation fluxes through the NRE211 and catalyst-coated membranes were identical, within the experimental error.

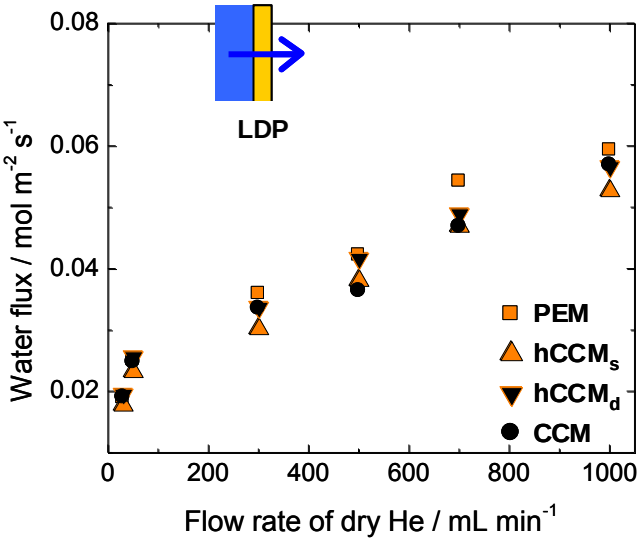

Figure 5-3 Liquid-dry permeation (LDP) fluxes through NRE211 and catalyst-coated membranes at 70°C. PEM(□), $hCCM_s$(△), $hCCM_d$(▼) and CCM(●).

5.2.3 Liquid-liquid Permeation (LLP)

The LLP flux of water increased linearly with applied pressure as shown in Figure 5-4. The gradient of the slope represents the hydraulic permeance. These values are 8.30 ± 0.18, 8.02 ± 0.14, 8.44 ± 0.19 and 8.20 ± 0.17 $x10^{-12}$ m Pa^{-1} s^{-1}, for PEM, $hCCM_s$, $hCCM_d$ and CCM, respectively, and are similar to permeance values presented previously for NRE211 (*c.f.*, section 3.2.1.2). As with VDP and LDP measurements, the presence of the catalyst layer had a negligible effect on the membrane's permeability to water.

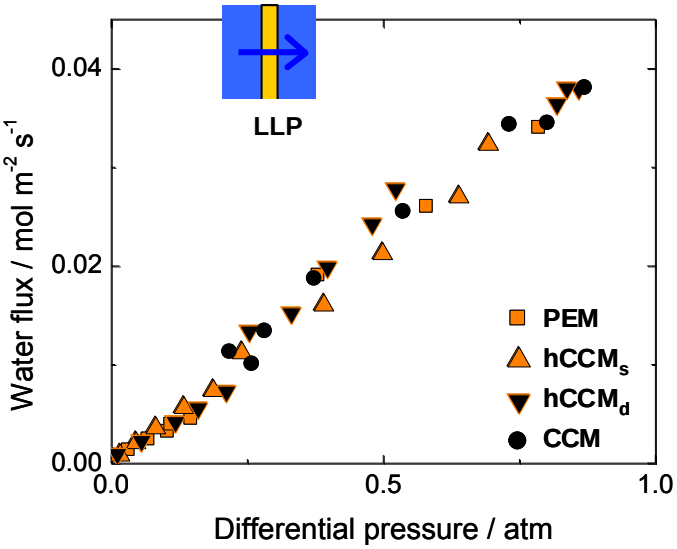

Figure 5-4 Liquid-liquid permeation (LLP) fluxes through NRE211 and catalyst-coated membranes at 70°C. PEM(□), $hCCM_s$(△), $hCCM_d$(▼) and CCM(●).

5.2.4 Comparison between the three modes of membrane water permeation

Figure 5-5 compares water permeation fluxes through NRE211 and catalyst-coated membranes measured under VDP, LDP and LLP conditions. Representative fluxes are taken at carrier gas flow rates of 500 and 1000 mL min^{-1} and a differential pressure of 1.0 atm for VDP, LDP and LLP, respectively. The RH values on the either side of the membrane under the various conditions are also provided in the figure. In this comparison, water fluxes associated with LDP and LLP are found to be ~4 and ~3 times larger than fluxes measured under VDP conditions. This observation is consistent with previous studies for pristine membranes.[25,83,87,115] As intimated previously (*c.f.*, section 3.2.1), this is due to the presence of liquid water at the membrane interface that maintains hydration and enhances water transport across the interface.

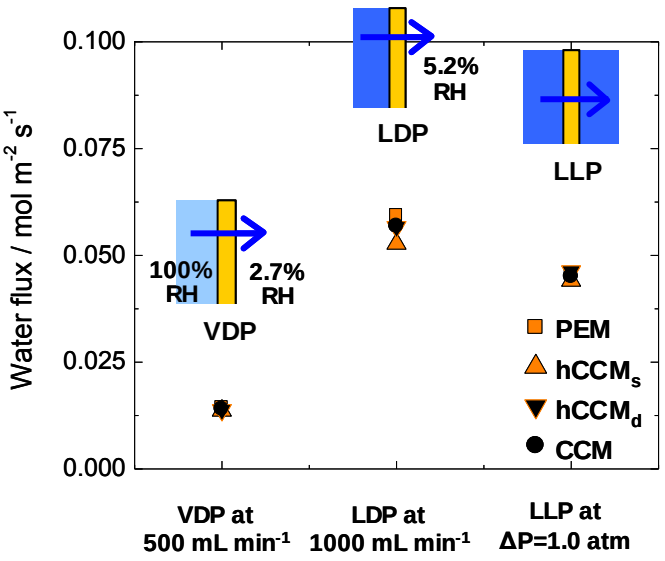

Figure 5-5 **Comparison of the representative water permeation fluxes measured by VDP, LDP and LLP for the NRE211 and catalyst-coated membranes. All measurements were conducted at 70°C. PEM(□), $hCCM_s$(△), $hCCM_d$(▼) and CCM(●).**

5.3 Conclusion

Three types of water permeation (VDP, LDP and LLP) were measured for NRE211 and catalyst-coated membranes at 70°C. The difference in permeabilities of NRE211 membrane (PEM), half-catalyst-coated membranes ($hCCM_s$ and $hCCM_d$) and catalyst-coated membrane (CCM) is negligible. The membrane is confirmed to be the "bottleneck" for water transport across catalyst-coated membranes; the presence of the catalyst layer apparently exerts no influence on the *interfacial* water sorption/desorption dynamics of the membrane interfaces, despite being located at the membrane/water interface. This is likely because the physical properties of the membrane extend into the catalyst layer.

CHAPTER 6 CONCLUSION AND FUTURE WORK

6.1 Conclusion

In this work, water permeability through Nafion® membranes was studied by systematically changing the phase of water (*i.e.*, liquid and vapour) at the membrane interfaces and varying the magnitudes of the chemical potential gradient. *Ex-situ* permeability measurements were designed and conducted to investigate the role of back permeation within an operating PEMFC. Water permeabilities under hydraulic permeation (liquid-liquid permeation, LLP), pervaporation (liquid-vapour permeation, LVP and liquid-dry permeation, LDP), and vapour permeation (vapour-vapour permeation, VVP and vapour-dry permeation, VDP) conditions were measured at 70^{o}C.

In the case of 28 μm NRE211 membranes, effective water permeation coefficients, *i.e.*, water flux values normalized to the chemical potential gradient of water, were determined for each water permeation scenario. The largest water permeation coefficient was obtained for LLP, which was two to three orders of magnitude larger than that obtained under LVP and VVP conditions, respectively. This was attributed to the high hydration state of the membrane, as well as a favourable water transport rate at the membrane interface. However, the differential chemical potential across the membrane during LLP was calculated to be approximately three orders of magnitude smaller than VVP and LVP. The magnitude of the chemical potential gradient of water across the

membrane was found to be significant in determining the water permeation flux. As a result, the water flux through the NRE211 membrane is largest when the membrane is exposed to liquid on one side and vapour on the other (*i.e.*, LVP).

In-situ water balance measurements were conducted by operating a single cell at 70^{o}C under four different operating conditions (*i.e.*, variations of RH and the pressures). *In-situ* net water fluxes revealed that liquid-vapour water transport is largely responsible for regulating the water balance within the operating fuel cell. It is found that formation of the membrane/liquid water interface at the cathode, and the creation of a sufficient chemical potential gradient across the membrane, enhances the back permeation of water through the operating MEA. When both these factors work together, in the cases of LVP, the water permeation flux was found to be large enough to offset the substantial EOD flux (anode to cathode) and allowed the membrane to self-regulate the water balance across an operating fuel cell.

Ex-situ measurements of the three modes of water permeation (*i.e.*, LLP, LVP, and VVP) were extended to investigate the effect of reducing the membrane thickness from 201 to 6 μm. Water permeation fluxes under LLP conditions increase with decreasing membrane thickness; water permeation fluxes under LVP and VVP conditions initially increase with decreasing membrane thickness (to 56 μm), but change little for further decreases in thickness.

Internal and *interfacial* water transport resistances for Nafion® are estimated for the three modes of water permeation. It is found that the

contribution of *interfacial* water transport resistance to *total* water transport resistance is significant and the contribution is found to increase with reduction in membrane thickness – explaining why further increases in water fluxes under LVP and VVP conditions were not observed with decreasing membrane thicknesses below 56 μm. The *interfacial* resistance was negligible when the membrane was exposed to liquid on both sides, *i.e.*, LLP. From the perspective of enhanced membrane water permeation, the results confirmed the advantage of liquid/membrane interfaces as part of the membrane water permeation process.

The maximum current density, where the back permeation flux offsets the EOD flux, was estimated according to the *ex-situ* water permeation measurements. The calculated maximum current densities increased with decreasing membrane thickness from 201 to 6 μm. It is found that under fuel cell operating conditions, the LVP-type back permeation of water effectively balances water transport for thick membranes (≥28 μm), while the LLP type back permeation of water was effective in balancing water transport for thin membranes (≤11 μm). The results further illustrate the advantage of forming a liquid/membrane interface for water permeation. The liquid/membrane interface facilitates the back permeation of water and leads to better water management in an operating fuel cell.

In-situ water balance measurements were also extended to investigate the effect of reducing the membrane thickness on performance of a PEMFC. Fuel cell performance improved with decreasing membrane thickness. Under dry-

anode/wet-cathode operating conditions, LVP is considered the prevalent means for back permeation of water, regardless of membrane thickness. In the case of ultra-thin membranes (6 to 11 μm), further increases in the rate of back permeation are observed, which may be attributed to the assistance of small hydraulic pressures across these thin membranes. Under dry operating conditions, in the low current density regime, VVP was found to be prevalent for the back permeation of water through membranes, regardless of membrane thickness. Higher current densities (>0.6 A cm^{-2}) were achieved in the case of thin membranes (6 to 28 μm), presumably due to the formation of a liquid/membrane interface at the cathode, for which the rate of back permeation is facilitated and the water accumulation at the cathode was mitigated.

Three types of water permeation were measured for catalyst-coated membranes at 70^{o}C. However, the differences in the permeabilities of pristine membranes, half-catalyst-coated membranes, and catalyst-coated membranes were found to be negligible. The results confirmed the membrane to be the "bottleneck" for water transport across CCM; the presence of the catalyst layer apparently exerts no influence on the *interfacial* water sorption/desorption dynamics of the membrane interfaces, despite being located at the membrane/water interface. This is likely because the physical properties of the membrane extend into the catalyst layer. Indeed, the water permeation fluxes of CCM was higher when the membrane was exposed to liquid water on one side and water vapour on the other (liquid-dry permeation, LDP), than when the

membrane was exposed to water vapour on both sides (vapour-dry permeation, VDP). This also coincides with the observations for pristine membranes.

The findings may be summarized as:

i. Water permeation flux increases with increasing differential chemical potential applied across the membrane.

ii. Under conditions relevant to PEMFC operation, the chemical potential gradient across the membrane is effectively created by a differential concentration of water rather than by differential pressure across the membrane.

iii. Water permeation flux increases with decreasing membrane thickness, except when the membrane is exposed to vapour. The rate-limiting water transport at the membrane/vapour interface prevents further increases in water permeation with decreasing membrane thickness.

iv. A catalyst layer coated on the membrane surface does not affect the rate of water permeation.

These findings have implications in the selection of membranes and the corresponding operating conditions of the fuel cell. For instance, to regulate the water balance effectively within an operating MEA, creating a membrane/liquid interface facilitates the back permeation of water; concentration gradient-driven back permeation of water is effective for thick membranes, while pressure gradient-driven back permeation of water is effective for thin membranes.

6.2 Further discussion and future work

This thesis work revealed that water transport at the membrane/vapour interface is the rate-limiting process in water permeation through Nafion® membranes. This raises the question: what determines the rate of water transport at the membrane/vapour interface? Both ingressing and egressing water transport at the membrane surface involves a phase change of water. Water vapour condenses on hydrophilic domains in the case of ingressing transport; and liquid water evaporates from hydrophilic domains in the case of egressing transport. The correlation between the size of the domain and the RH of the environment is described by Kelvin's equation. The evaporation and condensation of water is driven by the difference in chemical potentials between liquid water in the membrane and the water vapour that is in contact with the membrane. Thus, the magnitude of differential chemical potential is a factor that determines the rate of phase change.

Besides the intrinsic rate of phase change of water, and the magnitude of the differential chemical potential, two other factors can be considered to affect the rates of evaporation and condensation of water at the membrane surfaces: (a) the areal size of the hydrophilic domains and (b) their hygroscopic nature. The sizes of hydrophilic domains in the bulk membrane have been reported to expand with increasing RH (*c.f.*, section 1.2.4). Indeed, electrochemical/contact-mode atomic force microscopy (AFM) studies revealed that hydrophilic domains at the membrane surface also increase with increasing RH, as shown in Figure 6-1.[133,146-148] A decrease in the size of the hydrophilic domain leads to a

decrease in the overall rates of evaporation and condensation. This may account for the difference in *interfacial* water transport resistances with decreasing RH (*c.f.*, Figure 4-9).

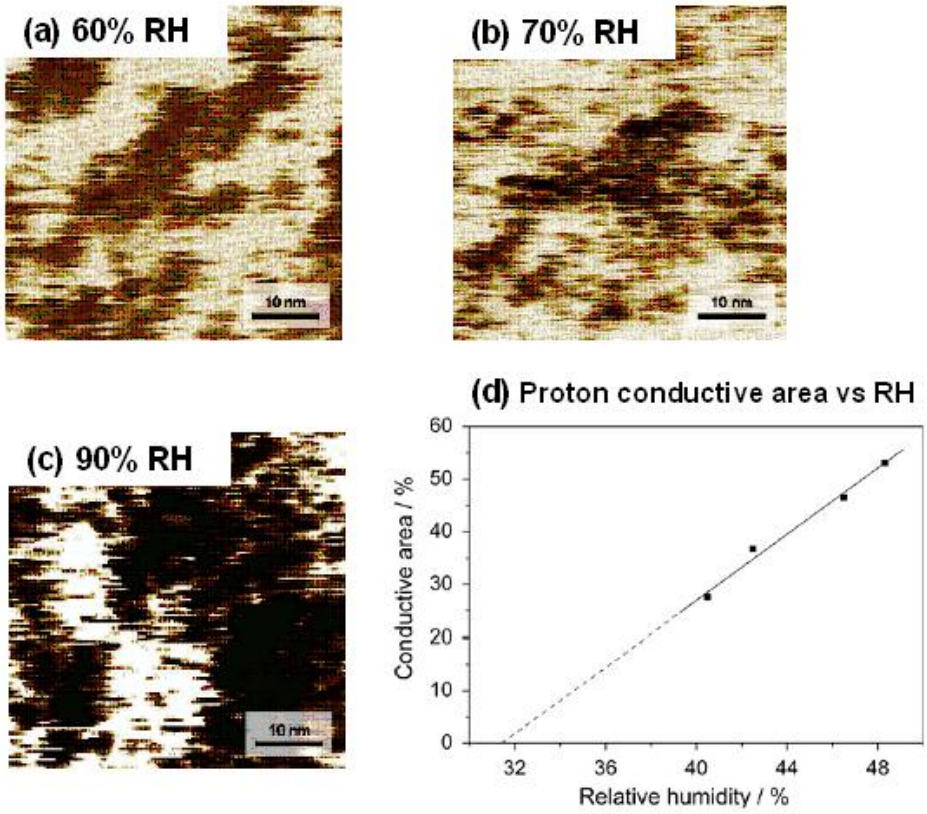

Figure 6-1 Current mapping images of Nafion® N115 membrane surface obtained by electrochemical/contact mode AFM, under conditions of (a) 60% RH, (b) 70% RH and (c) 90% RH. Dark areas indicate the proton conducting domains (*i.e.*, hydrophilic domains)[133] Copyright (2009) with permission from Elsevier. (d) Area-ratio of the proton conductive domains of Nafion® N117 membrane surface versus RH.[146] Copyright (2007) with permission from Royal Society of Chemistry.

The hygroscopic nature of the hydrophilic domains may also affect the sorption and desorption of water at the membrane surface. It has been reported that the amount of water in the hydrophilic domains decreases as RH is

reduced.[80,89,149] However, since the number of sulfonic groups remains constant, it leads to an increase in acidity (*i.e.*, increase in proton concentration) within the hydrophilic domains. As a preliminary experiment, the evaporation rate of water was measured for aqueous sulfuric acid solution. The mass lost of a solution-filled beaker was measured over time (placed in a water bath at 70^{o}C, similar to the LVP setup, but in the absence of the membrane). Figure 6-2 shows the evaporation rate of water versus concentration of sulfuric acid. As seen in this figure, the evaporation rate of water was reduced as the concentration of the sulfuric acid increased. While the reported proton concentration of the hydrophilic domain of fully hydrated Nafion® membrane is estimated to be ~2.6 mol L^{-1},[46] the proton concentration within the membrane is expected to increase even further with dehydration of the membrane. Thus, it may be that the evaporation rate of water is suppressed with dehydration of the membrane, due to the increase in acidity of the hydrophilic domains, and it may also explain the differences in *interfacial* water transport resistances ($R_{interface}$) between LVP and VVP (*c.f.*, section 4.3.1).

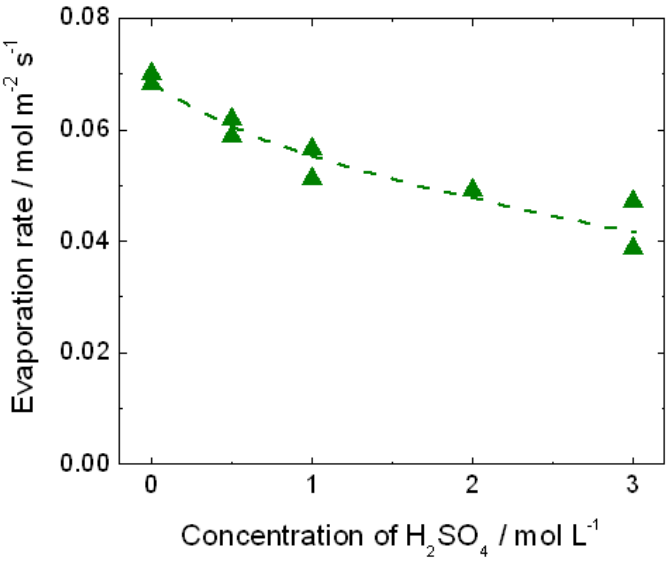

Figure 6-2 Evaporation rate of water versus concentration of sulfuric acid at 70°C, ambient pressure. RH of the surrounding environment is 40% RH at 25°C.

A combination of factors, such as site-specific sorption of water hydrophilic domains (<50% of the total surface, *c.f.*, Figure 6-1(d)); the decrease in size of the hydrophilic domains with decreasing RH; and hygroscopic interaction between water and the acidic domains in the membrane, are all considered to influence the rate of water transport at the membrane/vapour interface.

Speculating that the water transport at the membrane/vapour interface may be sensitive to the factors discussed above, another question raised is: why the catalyst layer had negligible influence to the water permeability through membranes? Especially since the catalyst layer is deposited on the membrane surface. As schematically shown in Figure 6-3, the agglomerates of carbon particles (100 - 300 nm) in the catalyst layer are covered with ionomer.[13,19,150] As also seen in the TEM image (*c.f.*, Figure 5-1(b)), the catalyst layer consists of

void spaces between the carbon agglomerates that range between 20 to 100 nm, *i.e.*, macropores, and void spaces within the carbon agglomerates that are <20 nm, *i.e.*, micropores.[20,150] The bundled-ionomer forms the hydrophilic domains and they are exposed to the macro- and micro- pores. These exposed hydrophilic domains are the access point for water, which evaporation and condensation occur. When the catalyst layer is in contact with liquid water on both sides of the membrane electrode assembly (*i.e.*, liquid-liquid permeation condition), it is expected that the rate of water transport through the catalyst layer is much greater than through the membrane, due to the differences in the pore sizes of water transporting pathways,[19,66] *i.e.*, the pore sizes of the membrane are one to two orders of magnitude smaller than the pore sizes of the catalyst layer (*c.f.*, section 1.2.4)). Thus, it is logical to speculate that membrane is the bottleneck for water permeation under LLP condition. However, when the catalyst layer is exposed to water vapour, it becomes more difficult to rationalize the negligible effect of the catalyst layer on rates of water transport. As shown in Figure 6-3, it is postulated that the bundled-ionomer coated around the carbon agglomerate determines the number of exposed hydrophilic domains that allow water to evaporate and condense. It is also postulated that the rates of evaporation and condensation is determined by surfaces near the membrane-catalyst layer interface because water molecules (~0.3 nm in diameter) can readily diffuse through macropores (20 – 100 nm) in the outer parts of the catalyst layer. In fact, diffusivity of water through vapour is few orders of magnitudes larger than the diffusivity through liquid water.[64,65,84,107,114,141-145]

Thus, the effective area of the exposed hydrophilic domains relevant to evaporation and condensation is not too dissimilar for catalyst-coated membrane compared to pristine membranes and may explain why the water permeability of the pristine membrane and the catalyst-coated membranes are similar under vapour-dry permeation and liquid-dry permeation conditions.

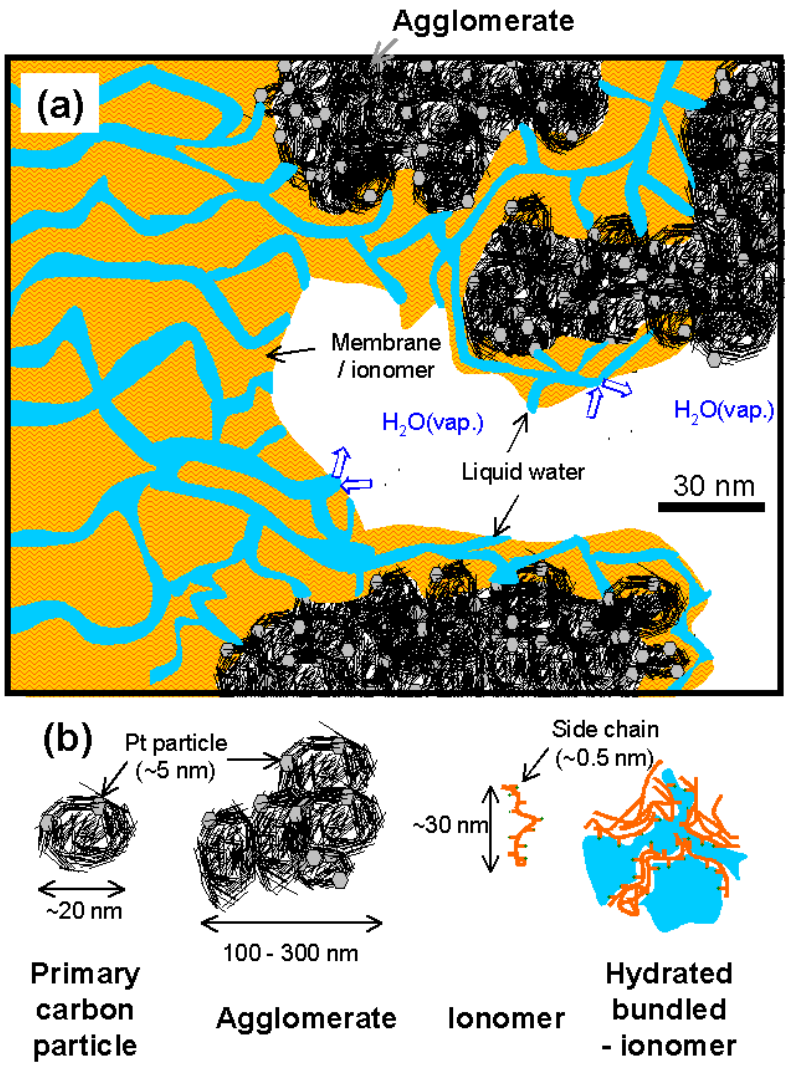

Figure 6-3 **(a) Schematic of the membrane-catalyst layer interface. The diameter of water molecules are ~0.3 nm[20], the diameter of the hydrophilic domains of the membrane/bundled-ionomer is 2 - 5 nm.[30,37,42] The carbon agglomerate sizes are 100 – 300 nm.[20,150] (b) Schematic representation of the primary carbon particle (~20 nm),[20,150] agglomerate of the primary carbon particles (100 – 300 nm),[20,150,151] single Nafion® oligomer (~ 30 nm, length of the side chain is ~ 0.5 nm),[20,151] and the hydrated bundle of ionomer. The green dot at the end of the side chain represents the sulfonic groups.**

Under fuel cell operating conditions, water is generated within the agglomerates (see Figure 6-3). When the current density is increased and the water is generated at a higher rate than the evaporation rate of water, it is not

unreasonable to assume that a liquid/ionomer interface is formed at the agglomerate/ionomer interface. This leads to LVP-type water permeation through the ionomer/membrane phase, which [dry operating condition (*c.f.*, section 4.2.2.2)] supports this assertion.

This thesis work has revealed that future work should focus on the studies of water transport phenomena at the membrane/vapour interface. The study can be extended to different membranes and measurement conditions (*i.e.*, temperature, RH and pressure). Identifying the key parameters that influences water transport at the membrane/vapour interface will be useful in the further development of high-water-permeable, gas-impermeable, ultra-thin membranes.

Studies of the water transport phenomena at the membrane/vapour interface can be approached from: (i) correlation studies of the surface properties of a membrane (*i.e.*, morphology and the hygroscopic properties) versus the rates of water transport – a material science approach; and (ii) measurements of the rate and the activation energy of water transport at the membrane/vapour interface – a thermodynamic approach. Steady-state rates of water vapour ingressing and egressing at the membrane/vapour interface can be measured using a setup similar to the LVP cell, presented in this work. Ultra-thin membranes, (ideally <10 μm) may be used in order to specifically study the *interfacial* water transport. Water sorption and desorption isotherms may be obtained in order to determine the equilibrium water content of the membranes.

When the study is targeted for developing PEMs for high temperature PEMFC applications (*i.e.*, >120^{o}C), *in-situ* water transport can be also studied. In high temperature PEMFC, the *in-situ* permeation of water might be best represented by a membrane/vapour interface. In order to investigate the impact of *interfacial* water transport to fuel cell performance above 100^{o}C, the prior *ex-situ* studies on *interfacial* water transport may be very useful. The outcomes of these studies may be useful for further advancement in high-temperature PEMFC technology, as well as other membrane processes that involve water vapour permeation through membranes.

APPENDICES

APPENDIX A EXPERIMENTAL SCHEME

Figure A - 1 summarizes the experimental scheme of this thesis work. Membranes were pre-treated prior to measurements. Water permeabilities under three conditions: liquid-liquid permeation (LLP), liquid-vapour permeation (LVP) and vapour-vapour permeation (VVP) were measured for all pristine membranes. Catalyst layers were coated on one side or both sides of the membrane to measure the water permeabilities of catalyst coated membranes and the *in-situ* net water fluxes through the operating membranes. The permeabilities of catalyst-coated membranes were obtained under three conditions: liquid-dry permeation (LDP), vapour-dry permeation (VDP) and LLP, mentioned above. Prior to the *in-situ* water balance measurements, the MEA was conditioned and polarization curves were obtained. All measurements were conducted at 70^{o}C.

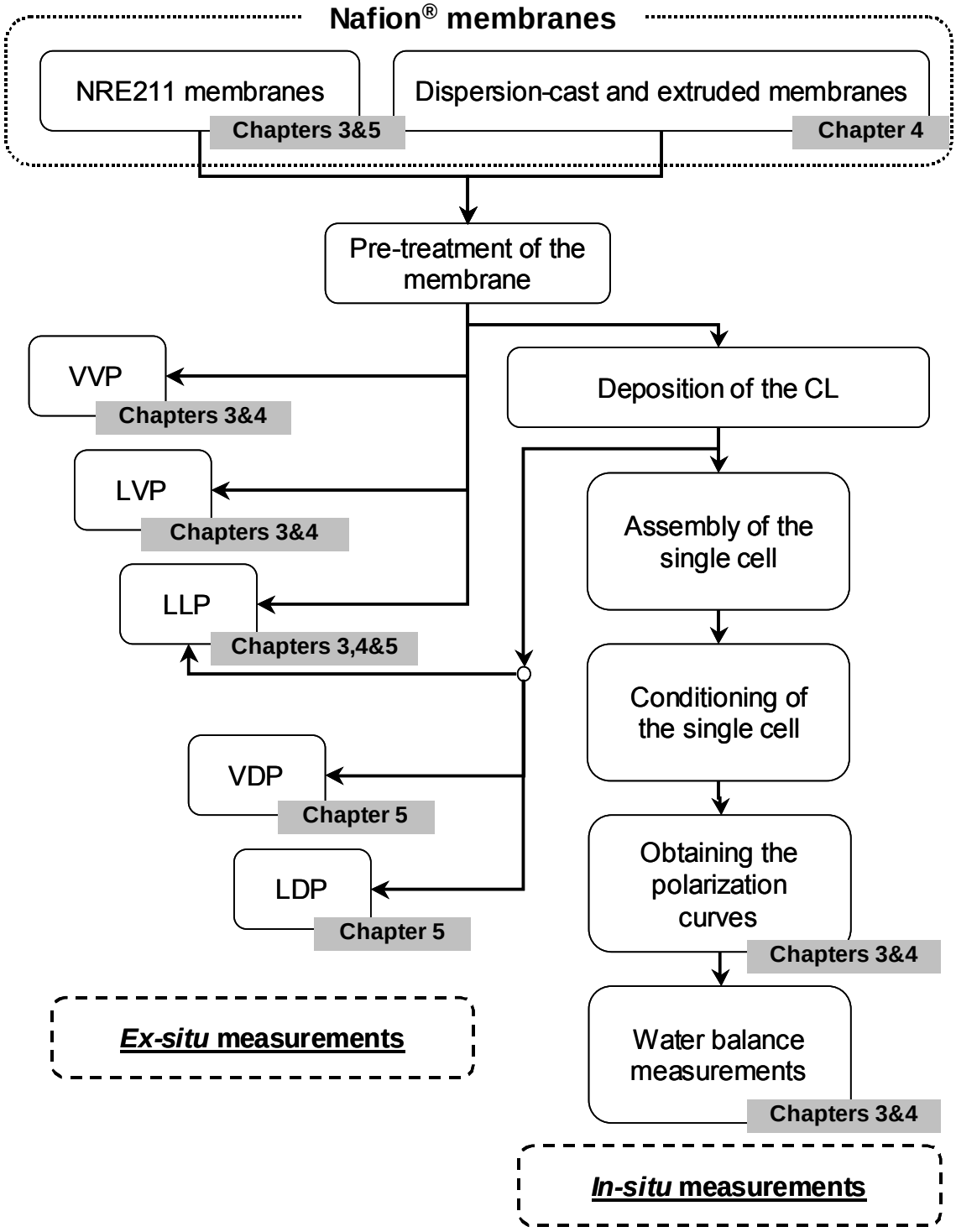

Figure A - 1 Experimental scheme of this thesis work.

APPENDIX B SAMPLE OF DATA ACQUISITION AND ANALYSIS

B.1 Vapour-vapour permeation (VVP)

Table B- 1 shows sample data sets of vapour-vapour permeation (VVP) through NRE211 membranes at 70°C. Δt, M_{ini} and M_{fin} represent the duration of the measurement, mass of the cell before and after the measurements, respectively.

Table B- 1 Sample data of vapour-vapour permeation (VVP) through NRE211. The geometrical active area for water permeation was 37.74 cm^2.

Date	set RH / %	Δt / min	Δt / s	M_{ini} / g	M_{fin} / g	J_{VVP} / mol m^{-2} s^{-1}
9th Nov 07	40	161	9660	1025.30	1016.50	**0.0133**
22nd Nov 07	50	260	15600	991.10	978.00	**0.0123**
20th Nov 07	60	247	14820	1049.80	1039.15	**0.0105**
20th Nov 07	70	199	11940	1034.55	1028.70	**0.0072**
5th Dec 07	80	268	16080	1091.45	1084.55	**0.0063**
5th Dec 07	90	338	20280	1084.20	1080.15	**0.0029**

As discussed in section 2.3.1, the vapour-vapour permeation fluxes are calculated according to Equation B-1 (Equation 2-1 in section 2.3.1).

$$J_{VVP} = \frac{\left(\frac{\Delta M}{M_{H_2O} \Delta t} \right)_{PEM}}{A} \quad \text{Equation B-1}$$

where $\Delta M/\Delta t$ represents the evaporation rate of water, M_{H_2O} and A represent the molar mass of water and the geometrical area of the membrane, respectively. ΔM can be calculated from Equation B-2.

$$\Delta M = M_{ini} - M_{fin} \quad \text{Equation B-2}$$

B.2 Liquid-vapour permeation (LVP)

Table B- 2 shows the sample data sets of liquid-vapour permeation (LVP) through NRE211 membrane at 70°C. Δt, M_{ini}, M_{fin} and $k_{background}$ represent the duration of the measurement, mass of the cell before and after the measurement and the evaporation rate of water from the perimeter of the polyethylene film (*c.f.*, section 2.3.1), respectively.

Table B- 2 Sample data of liquid-vapour permeation (LVP) through NRE211. The geometrical active area for water permeation was 38.08 cm^2.

				background		NRE211			
Date	set RH / %	Δt / min	Δt / s	M_{ini} / g	M_{fin} / g	M_{ini} / g	M_{fin} / g	$k_{background}$ / mol s^{-1}	J_{LVP} / mol m^{-2} s^{-1}
9th Oct 07	40	161	9660	1501.10	1478.30	1445.20	1319.80	1.304E-04	**0.154**
11thOct 07	50	168	10084	1575.45	1551.40	1531.90	1419.75	1.317E-04	**0.127**
1st Oct 07	60	181	10876	1517.25	1498.80	1499.15	1410.15	9.370E-05	**0.094**
3rd Oct 07	70	197	11842	1478.75	1465.65	1383.90	1302.10	6.110E-05	**0.084**
4th Oct 07	80	162	9728	1526.05	1518.40	1346.20	1300.05	4.343E-05	**0.057**
5th Oct 07	90	191	11453	1549.00	1542.10	1463.70	1426.45	3.328E-05	**0.038**

The water evaporation rate of the "background" cell, $k_{background}$, is calculated according to Equation B-3:

$$k_{background} = \left(\frac{\Delta M}{M_{H_2O} \Delta t} \right)_{background} \quad \text{.....Equation B-3}$$

where $\Delta M/\Delta t$ and M_{H_2O} represent the evaporation rate of water and the molar mass of water, respectively. ΔM can be calculated from Equation B-2. The liquid-vapour permeation fluxes are calculated according to Equation B-4 (Equation 2-2 in section 2.3.1).

$$J_{LVP} = \frac{\left(\frac{\Delta M}{M_{H_2O} \Delta t} \right)_{PEM} - \left(\frac{\Delta M}{M_{H_2O} \Delta t} \right)_{background}}{A} \quad \text{.....Equation B-4}$$

where A is the geometrical area of the membrane.

B.3 Liquid-liquid permeation (LLP)

Table B- 3 shows the sample data sets of liquid-liquid permeation (LLP) through NRE211 membrane at 70°C. j_v, Δp, and j_m represent the measured volumetric flow rate of water, differential pressure measured across the membrane, and the molar flow rate of water, respectively.

Table B- 3 Sample data of liquid-liquid permeation (LLP) through NRE211. The geometrical active area for water permeation was 4.13 cm^2.

Date	j_v / m^3 s^{-1}	Δp / Pa	j_m / mol s^{-1}	J_{LLP} / mol m^{-2} s^{-1}	Δp / atm
30th Oct 08	3.660E-10	1.055E+05	2.018E-05	**0.049**	**1.04**
	2.523E-10	7.967E+04	1.391E-05	**0.034**	**0.79**
	1.939E-10	5.877E+04	1.069E-05	**0.026**	**0.58**
	1.420E-10	3.860E+04	7.828E-06	**0.019**	**0.38**
	4.650E-10	1.186E+05	2.564E-05	**0.062**	**1.17**

The liquid-liquid permeation fluxes are calculated according to Equation B-5.

$$J_{LLP} = \frac{10^3 j_m \rho}{M_{H_2O} A} \quad \text{Equation B-5}$$

where ρ, M_{H_2O} and A represent the density of water at 293K, molar mass of water, and the geometrical area of the membrane, respectively. The density of water (ρ) at 298 K, 998.207 kg m^{-3}, was used in the calculation.[6]

B.4 Vapour-dry permeation (VDP) and liquid-dry permeation (LDP)

Table B- 4 and Table B- 5 show the sample data sets of vapour-dry permeation (VDP) and liquid-dry permeation (LDP), respectively, through NRE211 membrane at 70°C. v, T_{cell}, T_{dp}, and p_{vp} represent the gas flow rate, the cell temperature, measured dew point temperature and the calculated water vapour pressure, respectively. The water vapour pressure of the carrier gas is calculated from the dew point temperature, according to Equation 2-3 and 2-4 in section 2.3.3.

Table B- 4 Sample data of vapour-dry permeation (VDP) through NRE211. The geometrical active area for water permeation was 2.00 cm^2.

Date	ν / mL min^{-1}	T_{cell} / °C	T_{dp} / °C	p_{vp} / kPa	J_{VDP} / mol m^{-2} s^{-1}
4th Feb 08	30	70	42.0	15.85	**0.007**
	50	70	36.2	13.04	**0.009**
	100	70	26.1	9.15	**0.010**
	300	70	12.5	3.44	**0.013**
	500	70	5.9	2.72	**0.014**
	700	70	0.6	2.25	**0.013**
	1000	70	-5.7	1.73	**0.012**

Table B- 5 Sample data of liquid-dry permeation (LDP) through NRE211. The geometrical active area for water permeation was 2.00 cm^2.

Date	ν / mL min^{-1}	T_{cell} / °C	T_{dp} / °C	p_{vp} / kPa	J_{LDP} / mol m^{-2} s^{-1}
22th May 08	30	70	55.1	15.85	**0.014**
	50	70	51.1	13.04	**0.019**
	100	70	44.1	9.15	**0.027**
	300	70	26.4	3.44	**0.030**
	500	70	22.5	2.72	**0.040**
	700	70	19.4	2.25	**0.046**
	1000	70	15.3	1.73	**0.051**

J_{VDP} and J_{LDP} can be calculated according to Equation B-6 (Equations 2-5, 2-6 and 2-7 in section 2.3.3).

$$J_{VDP,LDP} = \frac{p_{vp} v}{RT_{cell} A(p_{tot} - p_{vp})} = \frac{M_{vp} v}{A\ (p_{tot} - p_{vp})} \quad \text{.....Equation B-6}$$

where R, A, and M_{vp} represent the universal gas constant, the geometrical area of the membrane, and molar concentration of water vapour, respectively. p_{tot} is the total pressure, which is 1.0 atm in this case.

B.5 *In-situ* net water flux from the water balance measurement

Table B- 6 show the sample data sets of *in-situ* net water flux through NRE211 membrane under 70°C, wet-anode/dry-cathode condition. E, J, and J_{e^-}, represent the measured cell voltage, current density, and the corresponding flux of electrons in the external circuit, respectively. The flux of electrons is equivalent to the protonic flux (J_{H^+}) through the membrane. M_{ini}, M_{fin} and Δt represent the mass of the water-collecting bottles before and after the measurement, and the duration of the measurement, respectively.

$j_{a\text{-}in}$ and $j_{a\text{-}in}$, respectively, represent the flow rate of water introduced and exhausted to/from the cell. While $j_{a\text{-}in}$ is obtained from the calibration measurement, prior to the experiment, $j_{a\text{-}out}$ can be calculated according to Equation B-7:

$$j_{a-out} = \frac{10^4 \Delta M'}{M_{H_2O} \Delta t} \quad \text{Equation B-7}$$

where ΔM', M_{H_2O}, and Δt represent the mass water collected, the molar mass of water, and the duration of the measurement, respectively. ΔM can be calculated from Equation B-8.

$$\Delta M' = M_{fin} - M_{ini} \quad \text{Equation B-8}$$

Thus, J^a_{NET} can be calculated according to Equation B-9 (Equation 2-9 in section 2.4.4):

$$J^{a}{}_{NET} = \frac{j_{a-out} - j_{a-in}}{A_{cell}} \quad \text{Equation B-9}$$

The net water transport coefficient, β, is calculated by normalizing the net molar flux of water to the molar flux of protons, and is expressed as Equation B-10 (Equation 2-10 in section 2.4.4):

$$\beta = \frac{J^{a}{}_{NET}}{J_{H^+}} \quad \text{Equation B-10}$$

Table B- 6 Sample data of *in-situ* net water flux through NRE211 under wet-anode/dry-cathode conditions. The geometrical active area of the cell was 25.0 cm^2.

75/70/50 Anode ***try1***	E / V	J / A cm^{-2}	Je^- / mol m^{-2} s^{-1}	Flow rate / L min^{-1}	M_{ini} / g	M_{fin} / g	M_{H2O} / g	Δt /s	$J_{a\text{-}out}$ / mol m^{-2} s^{-1}	$J_{a\text{-}in}$ / mol m^{-2} s^{-1}	J_{NET} / mol m^{-2} s^{-1}	β
27th Feb 2007	0.84	0.10	0.010	0.244	179.00	186.35	7.35	5283	0.031	-0.048	**0.017**	*1.64*
27th Feb 2007	0.81	0.20	0.021	0.245	170.20	176.35	6.15	4616	0.029	-0.048	**0.018**	*0.88*
27th Feb 2007	0.76	0.40	0.041	0.244	159.75	168.00	8.25	6614	0.028	-0.048	**0.020**	*0.49*
27th Feb 2007	0.70	0.60	0.062	0.307	153.35	157.80	4.45	2817	0.035	-0.060	**0.025**	*0.40*
28th Feb 2007	0.65	0.80	0.083	0.375	143.90	152.55	8.65	4078	0.047	-0.073	**0.026**	*0.32*
28th Feb 2007	0.56	1.00	0.104	0.444	155.75	163.45	7.70	3227	0.053	-0.085	**0.032**	*0.31*
28th Feb 2007	0.47	1.20	0.124	0.514	175.25	182.35	7.10	2594	0.060	-0.099	**0.038**	*0.31*
28th Feb 2007	0.35	1.40	0.145	0.582	144.15	150.30	6.15	2158	0.063	-0.112	**0.049**	*0.34*
28th Feb 2007	0.22	1.60	0.166	0.662	154.90	164.45	9.55	3015	0.070	-0.121	**0.051**	*0.31*

75/70/50 Anode ***try2***	E / V	J / A cm^{-2}	Je^- / mol m^{-2} s^{-1}	Flow rate / L min^{-1}	M_{ini} / g	M_{fin} / g	M_{H2O} / g	t /s	$J_{a\text{-}out}$ / mol m^{-2} s^{-1}	$J_{a\text{-}in}$ / mol m^{-2} s^{-1}	J_{NET} / mol m^{-2} s^{-1}	β
2nd Mar 2007	0.84	0.10	0.010	0.244	148.35	163.65	15.30	11600	0.029	-0.048	**0.019**	*1.80*
1st Mar 2007	0.81	0.20	0.021	0.244	144.00	148.45	4.45	3630	0.027	-0.048	**0.021**	*1.00*
1st Mar 2007	0.76	0.40	0.041	0.244	169.35	174.50	5.15	4020	0.028	-0.048	**0.019**	*0.47*
9th Feb 2007	0.70	0.60	0.062	0.305	149.05	153.60	4.55	2670	0.038	-0.060	**0.022**	*0.35*
1st Mar 2007	0.65	0.80	0.083	0.373	143.65	149.95	6.30	3588	0.039	-0.073	**0.034**	*0.41*
9th Feb 2007	0.55	1.00	0.104	0.444	169.60	177.05	7.45	2769	0.059	-0.085	**0.026**	*0.25*
12th Feb 2007	0.47	1.20	0.124	0.514	169.60	178.55	8.95	3380	0.059	-0.099	**0.040**	*0.32*
12th Feb 2007	0.37	1.40	0.145	0.583	154.70	161.25	6.55	2409	0.060	-0.112	**0.052**	*0.36*
13th Feb 2007	0.22	1.60	0.166	0.653	154.90	167.10	12.20	4447	0.061	-0.121	**0.061**	*0.37*

APPENDIX C DERIVATION OF THE ACTIVATION ENERGIES (E_A) OF WATER PERMEATION THROUGH NAFION® MEMBRANES

Representative VDP, LDP and LLP fluxes at 30, 50, 70^{o}C are shown in Figure C- 1. The values presented here are the water permeation fluxes through Nafion® NRE211 membranes (PEM) and the catalyst-coated membranes (CCM). Water fluxes of VDP and LDP were taken at carrier gas flow rate of 500 and 1000 mL min^{-1}, respectively; water fluxes of LLP were taken at differential pressure of 1.0 atm.

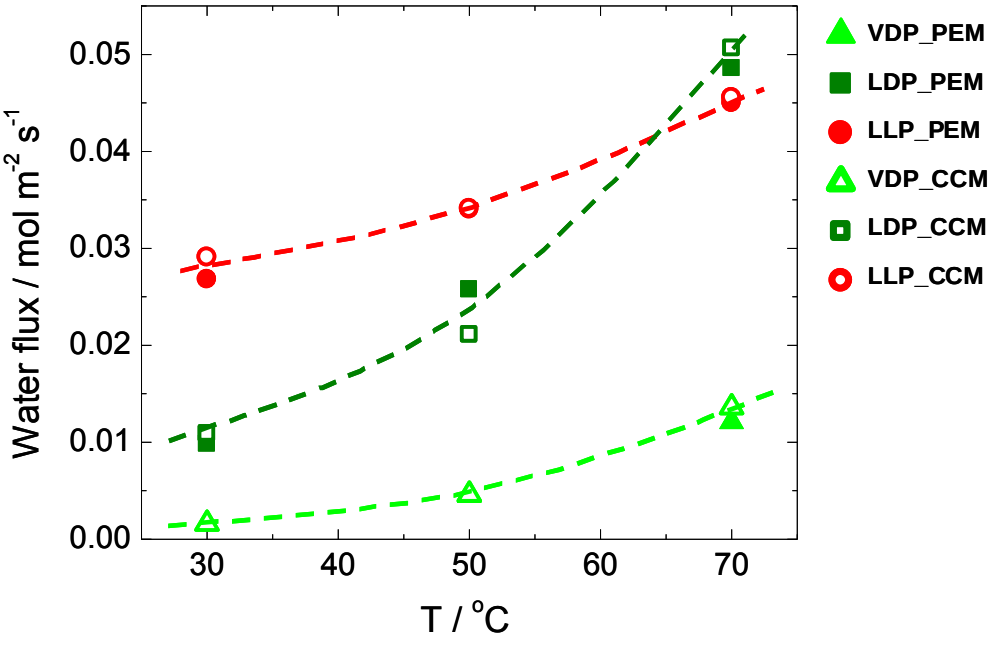

Figure C- 1 Representative VDP, LDP and LLP fluxes at 30, 50 and 70°C. VDP(▲, △), LDP(■, □) and LLP(●, ○). Open symbols correspond to PEM; closed symbols correspond to CCM.

Significant increases in water fluxes were seen for all three types of water permeation. For VDP and LDP, fluxes increased ~2.2 and ~2.8 times, respectively, at every temperature increase of 20°C between 30 to 70°C; for LLP, fluxes increased ~1.4 and ~2.2 times, when the temperature was increased from 30 to 50°C and from 50 to 70°C, respectively.

These water fluxes of VDP, LDP and LLP were normalized with the driving force that lead to water permeation, in order to determine the effective water permeation coefficients. The differential chemical potential across the membrane during water permeation is estimated as described in section 3.2.1.3. The effective permeation coefficients, k_{eff}, with the unit of $mol^2\ m^{-2}\ s^{-1}\ kJ^{-1}$, are fitted in

the Arrhenius equation (Equation C-1) to determine the activation energies of water permeation.

$$k_{eff} = Ae^{-\frac{E_a}{RT}} \quad \text{Equation C-1}$$

where A, E_a, R and T represents Arrhenius constant, activation energy, gas constant and temperature. This could be rewritten as:

$$\ln k^{eff} = \frac{-E_a}{R}\frac{1}{T} - \ln A \quad \text{Equation C-2}$$

The Arrhenius plot (ln k_{eff} - T^{-1} plot) shown in Figure C- 2, which the activation energy (E_a) is derived from the slope.

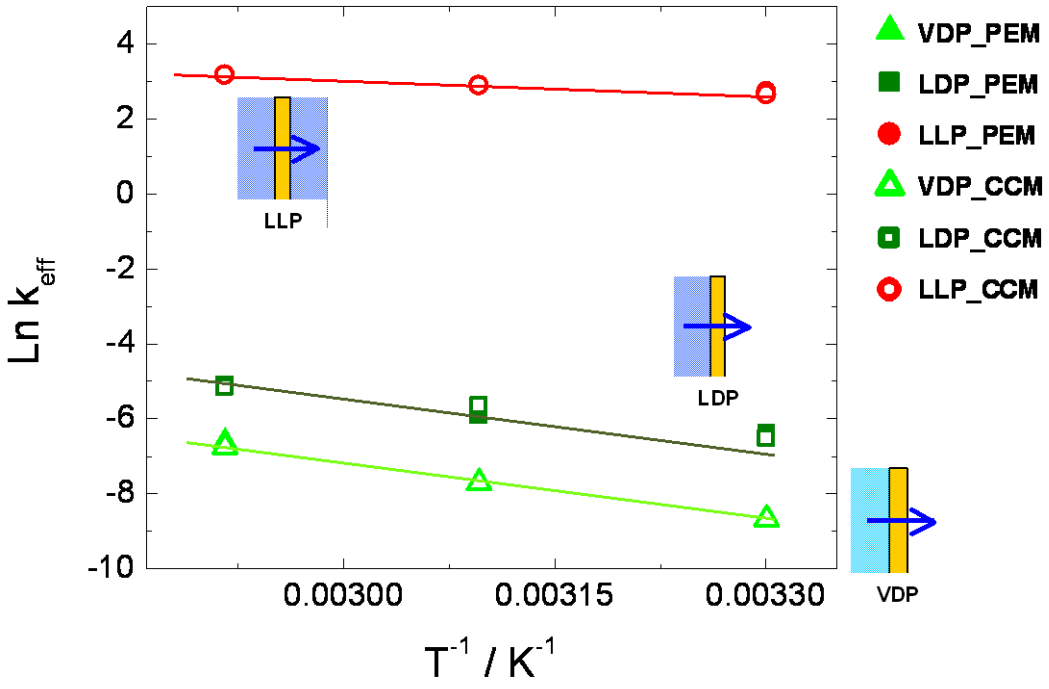

Figure C- 2 Arrhenius plot of the effective water permeation coefficients, k_{eff} ($mol^2\ m^{-2}\ s^{-1}\ kJ^{-1}$). VDP(▲, △), LDP(■, □) and LLP(●, ○). Open symbols correspond to PEM. Closed symbols correspond to CCM.

The activation energies (E_a) of vapour-dry permeation (VDP), liquid-dry permeation (LDP) and liquid-liquid permeation (LLP) were found to be 44.4, 27.4 and 9.6 kJ mol^{-1}, respectively for PEM; and 41.4, 29.5 and 11.2 kJ mol^{-1}, respectively for CCM, and are summarized in Table C- 1. The activation energies obtained for each modes of water permeation (*i.e.*, VDP, LDP and LLP), were similar for both PEM and CCM.

Table C- 1 Activation energies obtained for vapour-dry permeation, liquid-dry permeation and liquid-liquid permeation through Nafion® NRE211 membranes and catalyst-coated membranes.

		E_a (kJ mol^{-1})
PEM	VDP	44.4 ± 3.0
	LDP	27.4 ± 5.2
	LLP	9.6 ± 2.0
CCM	VDP	41.4 ± 1.4
	LDP	29.5 ± 3.9
	LLP	11.2 ± 0.9

APPENDIX D DERIVATION OF THE WATER TRANSPORT COEFFICIENTS

D.1 Interfacial and internal water transport coefficients: $k_{internal}$ and $k_{interface}$

Water transport coefficients within, and, at the interfaces of the membrane can be estimated based on the deconvoluted water transport resistances obtained in section 4.3.1. The internal and interfacial water transport coefficients of VVP, LVP and LLP of Nafion® at 70°C are presented in Figure D- 1(a) and (b).

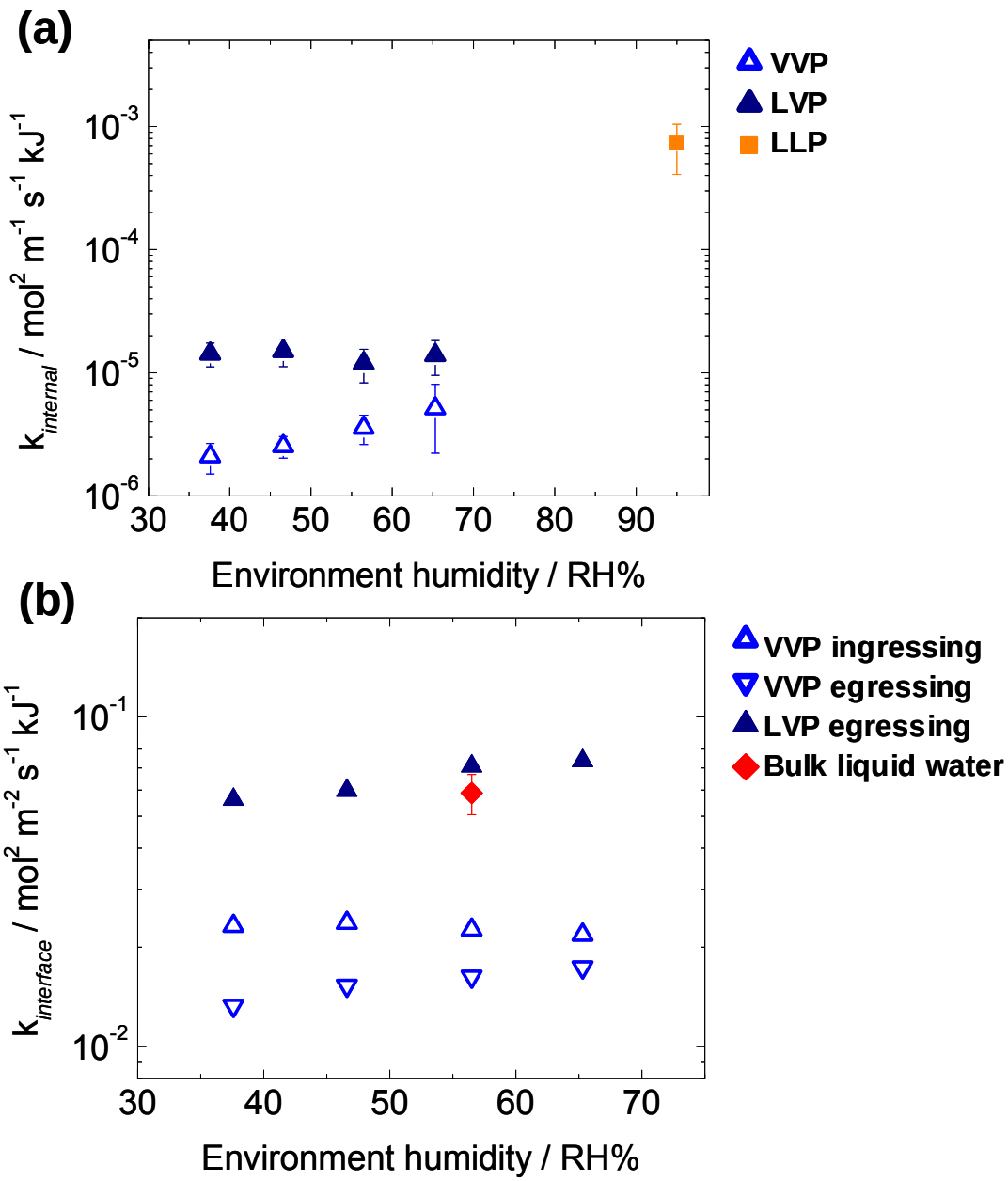

Figure D- 1 **(a) Internal water transport coefficients ($k_{internal}$) of Nafion® at 70°C. VVP (△), LVP (▲) and LLP (■). (b) Interfacial water transport coefficients ($k_{interface}$) of: the ingressing surface during VVP (△), at the egressing surface during VVP (▽), and at the egressing surface during LVP (▲) at 70°C. Effective phase transition coefficient of bulk liquid water (◆) at 70°C is also shown in the figure.**

Derivation of the coefficients:

In the case of liquid-liquid permeation (LLP), *interfacial* water transport resistance is negligible and the *internal* water transport coefficient ($k_{internal}^{LLP}$) can be described as:

$$k_{eff}^{LLP} = k_{internal}^{LLP} = \frac{J_{LLP} t(\lambda)}{\Delta\mu_{LLP}} = \frac{1}{R_{LLP}} \quad \text{Equation D-1}$$

where k_{eff}^{LLP}, J_{LLP}, $\Delta\mu_{LLP}$ and R_{LLP} represent the effective water permeance value of the membrane, water permeation flux, differential chemical potential and water transport resistance, respectively, for LLP. t(λ) represents the thickness of the membrane, which is a function of the water content, and λ is the number of water molecules per sulfonic acid group. In the fully hydrated case, *e.g.*, when the membrane is exposed to liquid water on both sides (*i.e.*, LLP condition), λ is measured to be 22 and wet membrane thicknesses (t_{wet}) are used in the calculation.

$$t(22) = t_{wet} \quad \text{Equation D-2}$$

The water transport coefficients for liquid-liquid permeation (LLP) are listed in Table 4-1 and plotted in Figure 4-1 of section 4.2.1. The average hydraulic permeability of Nafion® membrane - the *internal* water transport coefficient of LLP (k^{LLP}) - is 7.3±3.2 x10^{-4} mol m^{-1} s^{-1} kJ^{-1}.

In the case of LVP, the water transport coefficients within, and, at the membrane interfaces ($k_{internal}^{LVP}$ and k_{egress}^{LVP}) can be calculated from the $R_{LVP\_internal}$ and $R_{LVP\_interface}$:

$$k_{internal}^{LVP} = \frac{J_{LVP} t(\lambda)}{\Delta\mu_{internal}} = \frac{t(\lambda)}{R_{LVP\_internal}} \quad \text{Equation D-3}$$

$$k_{egress}^{LVP} = \frac{J_{LVP}}{\Delta\mu_{interface}} = \frac{1}{R_{LVP\_interface}} \quad \text{Equation D-4}$$

where J_{LVP}, $\Delta\mu_{internal}$, $\Delta\mu_{interface}$ and $t(\lambda)$ represent the water permeation flux, chemical potential driving forces and the membrane thickness. Water content of the membrane (λ) at given RH (*i.e.*, vapour pressure (p_{vp})) was estimated with a fitted equation (Equation D-5) according to Burnett et al.'s results.[80]

$$\lambda = -3298.4 p_{vp}^{\ 4} + 2069.5 p_{vp}^{\ 3} - 394.88 p_{vp}^{\ 2} + 66.71 p_{vp} \quad \text{Equation D-5}$$

As mentioned above, λ is 22 for membrane in contact with liquid water on both sides. Under LVP conditions (liq./PEM/vap.), the water content of the bulk membrane ($\lambda_{average}$) is defined as the average of the water contents at the two membrane interfaces, which are 22 and the corresponding λ, calculated. The thickness of the membrane was assumed to increase linearly with the water content:[78]

$$t(\lambda) = t_{dry} + (t_{wet} - t_{dry}) \frac{\lambda_{average}}{22} \quad \text{Equation D-6}$$

where, t_{dry} and t_{wet} represent the dry and wet membrane thicknesses, respectively.

In the case of VVP, the *internal* and *interfacial* water transport coefficients are described by Equations D-7 and D-8.

$$k_{internal}^{VVP} = \frac{J_{VVP} t(\lambda)}{\Delta\mu_{internal}} = \frac{t(\lambda)}{R_{VVP\_internal}} \quad \text{Equation D-7}$$

$$k_{interface}^{VVP} = \frac{J_{VVP}}{\Delta\mu_{interface}} = \frac{1}{R_{VVP\_interface}} \quad \text{Equation D-8}$$

where J_{VVP}, $k_{internal}^{VVP}$, $k_{interface}^{VVP}$, $\Delta\mu_{internal}$, and $\Delta\mu_{interface}$ represent the water permeation flux, *internal* and *interfacial* water transport coefficients and the chemical potential driving forces, respectively. $k_{interface}^{VVP}$ encompasses the water transport rates at both the ingressing and egressing interfaces. As previously alluded to the hydrophilic domain sizes at the membrane surface increase with RH,[133,146-148] the *interfacial* transport resistance ($R_{interface}$) thus increases with decreasing the water content (λ), and in the absence of definitive data, a linear correlation is assumed. The *interfacial* water transport resistance at each interface can therefore be described as:

$$R_{ingress} = R_{interface} \frac{\lambda_{egress}}{\lambda_{egress} + \lambda_{ingress}} \quad \text{Equation D-9}$$

$$R_{egress} = R_{interface} \frac{\lambda_{ingress}}{\lambda_{egress} + \lambda_{ingress}} \quad \text{Equation D-10}$$

where $R_{ingress}$ and R_{egress} represent *interfacial* water transport resistances; $\lambda_{ingress}$ and λ_{egress} represent the water contents at the ingressing and egressing vapour/membrane interfaces, respectively. The water content at the membrane interface is derived from the RHs set by the VVP measurement and according to Equation D-5. Thus, the $k_{interface}^{VVP}$ is deconvoluted into *interfacial* transport coefficients of water at the ingressing and egressing interfaces ($k_{ingress}^{VVP}$ and k_{egress}^{VVP}) and are described according to Equations D-11 and D-12.

$$k_{ingress}^{VVP} = \frac{1}{R_{VVP\_ingress}} \quad \text{Equation D-11}$$

$$k_{egress}^{VVP} = \frac{1}{R_{VVP\_egress}} \quad \text{Equation D-12}$$

Additionally, the evaporation rate of bulk water, was measured by omitting the membrane using the LVP setup under the condition of 70^{o}C, 57% RH. The effective phase transition coefficient of bulk water is obtained and also presented in Figure D- 1(b).

D.2 Comparison with other reported transport coefficients

The *internal* and *interfacial* water transport coefficients defined by chemical potential gradient are converted to concentration gradient driven coefficients, which are widely reported in literature *i.e.*, diffusion and mass transfer coefficients of water.

The obtained diffusion coefficients and the averaged water transfer coefficients of Nafion® surface under VVP and LVP conditions are plotted versus the averaged water content within the membrane in Figure D- 2(a) and (b), respectively.

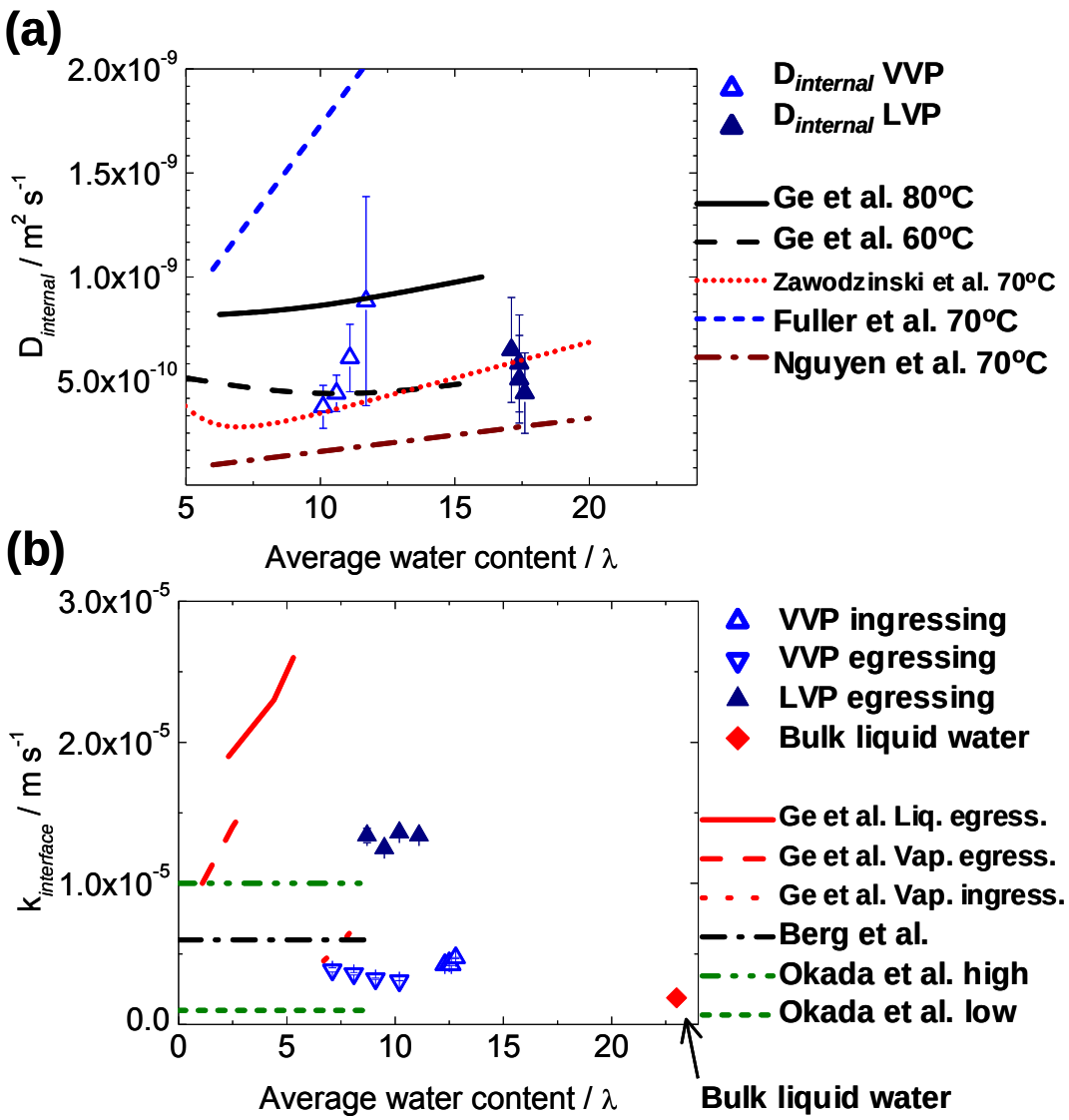

Figure D- 2 (a) Internal diffusion coefficient of water in Nafion® versus averaged water content (λ) at 70°C. VVP (△) and LVP (▲). (b) Mass transfer coefficients of water at Nafion® surface versus apparent averaged water content (λ) of the surface. Interfacial transport coefficients for: ingressing surface during VVP (△), egressing surface during VVP (▽) and egressing surface during LVP (▲). Effective phase transition coefficient of bulk liquid water (◆) at 70°C is also shown in the figure. The corresponding reported values at 80°C, are presented for comparison.[84,84,107,114,152-155]

The values are found to be similar to the reported coefficients of self-diffusion coefficients[107,114,152,153] and effective diffusion coefficients[84] of water for Nafion® at similar temperature and hydration states. The water transfer coefficients are also found in the same range as the other reported values.[84,154,155]

Derivation of the coefficients:

Firstly, the defined chemical potentials at the interfaces and within the membrane are converted to equivalent vapour pressure (p_{vp}).

$$p_{vp} = p_{tot} e^{\frac{\mu_{H_2O}}{RT}} \quad \text{.....Equation D-13}$$

where p_{tot}, μ_{H_2O}, R and T represent the total gas pressure, the chemical potential of water vapour, the universal gas constant and the temperature, respectively. The obtained vapour pressure is then converted to membrane water content, λ, according to Equation D-5. The concentration of water (c_{H_2O}) within and at the interface of the membrane can be described according to Equation D-14.[69]

$$c_{H_2O} = \lambda \frac{\rho}{EW} \quad \text{.....Equation D-14}$$

where c_{H_2O}, ρ and EW represent the water concentration, dry density and the equivalent weight of Nafion.[31,32] The differential water concentration within the membrane was used to estimate the diffusion coefficient:

$$D_{internal} = J_{WP} \frac{t(\lambda)}{\Delta c_{H_2O}^{internal}} \quad \text{.....Equation D-15}$$

where $D_{internal}$, J_{WP}, t(λ) and $\Delta c_{H_2O}^{internal}$ represent the *internal* diffusion coefficient, the water permeation flux, the membrane thickness as a function of the water content and the differential water concentration within the membrane.

The water transfer coefficients are estimated in a similar manner. The water permeation flux (J_{WP}) and the apparent water concentration difference ($\Delta c_{H_2O}^{interface}$) at the membrane surface are used in the calculation.

$$k_{interface} = \frac{J_{WP}}{\Delta c_{H_2O}^{interface}} \quad \text{Equation D-16}$$

REFERENCES:

1. C. Spiegel S, *Designing & Building Fuel Cells*, The McGraw-Hill Companies, New York (2007).

2. J. Larminie and A. Dicks, *Fuel Cell Systems Explained*, p. 75, John Wiley & Sons Ltd, New York (2003).

3. B. Hoehlein, G. Isenberg, R. Edinger and T. Grube, in *Handbook of Fuel Cells*, W. Vielstich, A. Lamm and H. A. Gasteiger, Editors, p. 245, John Wiley & Sons Ltd, West Sussex (2003).

4. General Motors Corporation, Argonne National Laboratory, BP, Exxon Mobil and Shell, Well-to-wheel Energy Use and Greenhouse Gas Emissions of Advanced Fuel/Vehicle Systems -North American Analysis- Executive Summary Report (2001).

5. N. L. Garland, US Department of Energy - Fuel cells sub-program overview (2008).

6. D. R. Lide, *Handbook of Chemistry and Physics*, CRC press, New York (1997).

7. P. W. Atkins, *Physical chemistry*, Oxford University Press, Oxford (1994).

8. A. J. Bard and L. R. Faulkner, *Electrochemical methods (Fundamentals and applications)*, John Wiley & Sons, Inc (2001).

9. H. A. Gasteiger, W. Gu, R. Makihara, M. F. Mathias and B. Sompalli, in *Handbook of Fuel Cells*, W. Vielstich, A. Lamm and H. A. Gasteiger, Editors, p. 593, John Wiley & Sons Ltd, West Sussex (2003).

10. J. Lipkowski and P. N. Ross, *Electrocatalysis*, Wiley, New York (1998).

11. D. P. Wilkinson and O. Vanderleeden, in *Handbook of fuel cells*, W. Vielstich, A. Lamm and H. A. Gasteiger, Editors, p. 315, John Wiley & Sons, West Sussex (2003).

12. E. Antolini, *J. Appl. Electrochem.,* 34, 6 (2004).

13. S. S. Kocha, in *Handbook of Fuel Cells*, W. Vielstich, A. Lamm and H. A. Gasteiger, Editors, p. 539, John Wiley & Sons Ltd, West Sussex (2003).

14. J. Roller, *Low Platinum Electrodes For Proton Exchange Fuel Cells Manufactured By Reactive Spray Deposition Technology,* M.A.Sc. Thesis, University of British Columbia (2008).

15. Z. Xie, X. Zhao, M. Adachi, Z. Shi, T. Mashio, A. Ohma, K. Shinohara, S. Holdcroft and T. Navessin, *Energy Environ. Sci.,* 1 (2008).

16. S. Litster and G. McLean, *J. Power Sources,* 130, 1-2 (2004).

17. T. Frey and M. Linardi, *Electrochim. Acta,* 50, 1 (2004).

18. E. Gulzow, M. Schulze, N. Wagner, T. Kaz, R. Reissner, G. Steinhilber and A. Schneider, *J. Power Sources,* 86, 1-2 (2000).

19. M. Eikerling, *J. Electrochem. Soc.,* 153, 3 (2006).

20. K. Malek, M. Eikerling, Q. Wang, T. Navessin and Z. Liu, *J. Phys. Chem. C,* 111, 36 (2007).

21. J. Liu and M. Eikerling, *Electrochim. Acta,* 53, 13 (2008).

22. H. M. Yu, C. Ziegler, M. Oszcipok, M. Zobel and C. Hebling, *Electrochim. Acta,* 51, 7 (2006).

23. T. Navessin, M. Eikerling, Q. Wang, D. Song, Z. Liu, J. Horsfall, K. V. Lovell and S. Holdcroft, *J. Electrochem. Soc.,* 152, 4 (2005).

24. Z. Xie, T. Navessin, K. Shi, R. Chow, Q. Wang, D. Song, B. Andreaus, M. Eikerling, Z. Liu and S. Holdcroft, *J. Electrochem. Soc.,* 152, 6 (2005).

25. M. Adachi, T. Navessin, Z. Xie, B. Frisken and S. Holdcroft, *J. Electrochem. Soc.,* 156, 6 (2009).

26. T. D. Astill, *Factors Influencing Electrochemical Properties of Hydrocarbon-based PEMFC Catalyst Layers,* Ph.D. Dissertation, Simon Fraser University (2008).

27. E. B. Easton, T. D. Astill and S. Holdcroft, *J. Electrochem. Soc.,* 152, 4 (2005).

28. S. Litster and N. Djilali, *Electrochim. Acta,* 52, 11 (2007).

29. M. Uchida, Y. Fukuoka, Y. Sugawara, N. Eda and A. Ohta, *J. Electrochem. Soc.,* 143, 7 (1996).

30. T. D. Gierke, G. E. Munn and F. C. Wilson, *J. Polym. Sci. Part B,* 19, 11 (1981).

31. DuPont, Nafion® PFSA Membranes NRE-211 and NRE-212 (2007).

32. DuPont, Nafion® PFSA Membranes N-112, NE1135, N-115, N-117 and NE1110 (2002).

33. Z.Shi and S.Holdcroft, *Macromolecules,* 38 (2005).

34. K. A. Mauritz and R. B. Moore, *Chem. Rev.,* 104, 10 (2004).

35. J. Peron, A. Mani, X. Zhao, D. Edwards, M. Adachi, T. Soboleva, Z. Shi, Z. Xie, T. Navessin and S. Holdcroft, *J. Membr. Sci.,* (Accepted).

36. K. D. Kreuer, S. J. Paddison, E. Spohr and M. Schuster, *Chem. Rev.,* 104, 10 (2004).

37. G. Gebel, *Polymer,* 41, 15 (2000).

38. A. -. Rollet, G. Gebel, J. -. Simonin and P. Turq, *J. Polym. Sci. Part B,* 39, 5 (2001).

39. L. Rubatat, A. L. Rollet, G. Gebel and O. Diat, *Macromolecules,* 35, 10 (2002).

40. A. -. Rollet, O. Diat and G. Gebel, *J. Phys. Chem. B,* 106, 12 (2002).

41. L.Rubatat, G.Gebel and O.Diat, *Macromolecules,* 37 (2004).

42. K. Schmidt-Rohr and Q. Chen, *Nat. Mat.,* 7, 1 (2008).

43. G. Gebel and J. Lambard, *Macromolecules,* 30, 25 (1997).

44. S. Slade, S. A. Campbell, T. R. Ralph and F. C. Walsh, *J. Electrochem. Soc.,* 149, 12 (2002).

45. M. N. Tsampas, A. Pikos, S. Brosda, A. Katsaounis and C. G. Vayenas, *Electrochim. Acta,* 51, 13 (2006).

46. T. J. Peckham, J. Schmeisser, M. Rodgers and S. Holdcroft, *J. Mater. Chem.,* 17, 30 (2007).

47. A. Siu, *Influence of water and membrane morphology on the transport properties of polymers for proton exchange membrane fuel cells,* Ph.D. Dissertation, Simon Fraser University (2007).

48. P. Choi, N. H. Jalani and R. Datta, *J. Electrochem. Soc.,* 152, 3 (2005).

49. K. D. Kreuer, *Solid State Ionics,* 136-137 (2000).

50. S. J. Paddison, *Annu. Rev. Mater. Res.,* 33 (2003).

51. S. J. Paddison and R. Paul, *Phys. Chem. Chem. Phys.,* 4, 7 (2002).

52. T. J. Peckham, Z. Xie, S. Holdcroft and Y. Yang, in *Proton Exchange Membranes Fuel Cells - Materials properties and performance*, D. P. Wilkinson, J. Zhang, R. Hui, J. Fergus and X. Li, Editors, p. 107, CRC press, Boca Raton, FL (2009).

53. N. Agmon, *Chem. Phys. Lett.,* 244, 5-6 (1995).

54. B. S. Pivovar, *Electrochemical Selectivity and Electro-osmosis in Direct Methanol Fuel Cell Electrolytes,* Ph.D. Dissertation, University of Minnesota (2000).

55. B. S. Pivovar, W. H. Smyrl and E. L. Cussler, *J. Electrochem. Soc.,* 152, 1 (2005).

56. K. Mayer and D. Woermann, *J. Membr. Sci.,* 127, 1 (1997).

57. X. Ren and S. Gottesfeld, *J. Electrochem. Soc.,* 148, 1 (2001).

58. J. Zawodzinski, T. E. Springer, F. Uribe and S. Gottesfeld, *Solid State Ionics,* 60, 1-3 (1993).

59. T. F. Fuller and J. Newman, *J. Electrochem. Soc.,* 139, 5 (1992).

60. M. Ise, K. D. Kreuer and J. Maier, *Solid State Ionics,* 125 (1999).

61. G. Xie and T. Okada, *J. Electrochem. Soc.,* 142, 9 (1995).

62. S. Ge, B. Yi and P. Ming, *J. Electrochem. Soc.,* 153, 8 (2006).

63. K. Aotani, S. Miyazaki, N. Kubo and M. Katsuta, *ECS Trans.,* 16, 2 (2008).

64. X. Ye and C. Y. Wang, *J. Electrochem. Soc.,* 154, 7 (2007).

65. N. G. C. Astrath, J. Shen, D. Song, J. H. Rohling, F. B. G. Astrath, J. Zhou, T. Navessin, Z. S. Liu, C. E. Gu and X. Zhao, *J. Phys. Chem. B,* 113, 24 (2009).

66. M. Eikerling, Y. Kharkats, A. A. Kornyshev and Y. Volfkovich, *J. Electrochem. Soc.,* 145, 8 (1998).

67. A. Z. Weber and J. Newman, *J. Electrochem. Soc.,* 151, 2 (2004).

68. A. Z. Weber and J. Newman, *Chem. Rev.,* 104, 10 (2004).

69. T. E. Springer, T. A. Zawodzinski and S. Gottesfeld, *J. Electrochem. Soc.,* 138 (1991).

70. A. Z. Weber, *Modelling water management in polymer-electrolyte fuel cells,* Ph.D. Dissertation, University of California, Berkeley (2004).

71. G. J. M. Janssen and M. L. J. Overvelde, *J. Power Sources,* 101, 1 (2001).

72. Q. Yan, H. Toghiani and J. Wu, *J. Power Sources,* 158, 1 (2006).

73. Y. Cai, J. Hu, H. Ma, B. Yi and H. Zhang, *Electrochim. Acta,* 51, 28 (2006).

74. F. Liu, G. Lu and C. Y. Wang, *J. Membr. Sci.,* 287, 1 (2007).

75. W. R. Vieth, *Diffusion In and Through Polymers*, Oxford University Press, New York (1979).

76. J. Comyn, *Polymer Permeability*, Springer, London (1985).

77. D. Rivin, C. E. Kendrick, P. W. Gibson and N. S. Schneider, *Polymer,* 42, 2 (2000).

78. D. R. Morris and X. Sun, *J. Appl. Polym. Sci.,* 50 (1993).

79. K. K. Pushpa, D. Nandan and R. M. Iyer, *J. Chem. Soc., Faraday Trans.,* 84, 6 (1998).

80. D. J. Burnett, A. R. Armando and F. Thielmann, *J.Power Sources,* 160 (2006).

81. P. Krtil, A. Trojanek and Z. Samec, *J. Phys. Chem. B,* 105 (2001).

82. M. Adachi, T. Romero, T. Navessin, Z. Xie, Z. Shi, W. Mérida and S. Holdcroft, *Electrochem.and Solid-State Lett.,* (Submitted).

83. M. Adachi, T. Navessin, Z. Xie, N. Li and S. Holdcroft, *J. Memb. Sci.,* (to be submitted).

84. S. Ge, X. Li, B. Li and I. M. Hsing, *J. Electrochem. Soc.,* 152, 6 (2005).

85. J. P. G. Villaluenga, B. Seoane, V. M. Barragan and C. Ruiz-Bauza, *J. Colloid Interface Sci.,* 268, 2 (2003).

86. T. Romero and W. Mérida, *J. Membr. Sci.,* 338, 1-2 (2009).

87. T. Romero, *Water transport in Proton exchange membranes,* Ph.D. Dissertation, University of British Columbia (2008).

88. P. W. Majsztrik, M. W. Satterfield, A. B. Bocarsly and J. B. Benzinger, *J. Membr. Sci.,* 301, 1-2 (2007).

89. T. A. Zawodzinski, C. Derouin, S. Radzinski, R. J. Sherman, V. T. Smith, T. E. Springer and S. Gottesfeld, *J. Electrochem. Soc.,* 140, 4 (1993).

90. X. Ren, T. E. Springer, T. A. Zawodzinski and S. Gottesfeld, *J. Electrochem. Soc.,* 147, 2 (2000).

91. K. H. Choi, D. H. Peck, C. S. Kim, D. R. Shin and T. H. Lee, *J. Power Sources,* 86, 1-2 (2000).

92. T. Murahashi, M. Naiki and E. Nishiyama, *J. Power Sources,* 162, 2 (2006).

93. H. Nakajima, T. Konomi and T. Kitahara, *J. Power Sources,* 171, 2 (2007).

94. K. Karan, H. Atiyeh, A. Phoenix, E. Halliop, J. Pharoah and B. Peppley, *Electrochem. Solid-State Lett.,* 10, 2 (2007).

95. S. Park, J. W. Lee and B. N. Popov, *J. Power Sources,* 163, 1 (2006).

96. S. Tsushima, K. Teranishi and S. Hirai, *Energy,* 30, 2-4 (2005).

97. K. Teranishi, S. Tsushima and S. Hirai, *J. Electrochem. Soc.,* 153, 4 (2006).

98. Z. Zhang, A. E. Marble, B. MacMillan, K. Promislow, J. Martin, H. Wang and B. J. Balcom, *J. Magn. Reson.,* 194, 2 (2008).

99. B. Andreaus and G. G. Scherer, *Solid State Ionics,* 168, 3-4 (2004).

100. T. E. Springer, T. A. Zawodzinski, M. S. Wilson and S. Gottesfeld, *J. Electrochem. Soc.,* 143, 2 (1996).

101. I. A. Schneider, H. Kuhn, A. Wokaun and G. G. Scherer, *J. Electrochem. Soc.,* 152, 12 (2005).

102. A. Takaichi, H. Uchida and A. Watanabe, *J. Electrochem. Soc.,* 154, 12 (2007).

103. F. N. Buchi and G. G. Scherer, *J. Electrochem. Soc.,* 148, 3 (2001).

104. M. M. Mench, Q. L. Dong and C. Y. Wang, *J.Power Sources,* 124, 1 (2003).

105. M. A. Hickner, N. P. Siegel, K. S. Chen, D. N. McBrayer, D. S. Hussey, D. L. Jacobsen and M. Arif, *J. Electrochem. Soc.,* 153, 5 (2006).

106. D. S. Hussey, D. L. Jacobsen, M. Arif, J. P. Owejan, J. J. Gagliardo and T. A. Trabold, *J.Power Sources,* 172, 1 (2007).

107. M. Saito, K. Hayamizu and T. Okada, *J. Phys. Chem. B,* 109, 8 (2005).

108. T. A. Zawodzinski, M.Neeman, L.O.Sillerud and S. Gottesfeld, *J. Phys. Chem.,* 95 (1991).

109. J. Kawamura, K. Hattori, T. Hongo, R. Asanuma, N. Kuwata, T. Hattori and J. Mizusaki, *Solid State Ionics,* 176, 31-34 (2005).

110. K. W. Feindel, S. H. Bergens and R. E. Wasylishen, *Chem. Phys. Chem.,* 7, 1 (2006).

111. F. Barbir, in *Handbook of Fuel Cells - Fundamentals Technology and Applications*, W. Vielstich, A. Lamm and H. A. Gasteiger, Editors, p. 683, John Wiley & Sons Ltd, West Sussex (2004).

112. G. Konrad, M. Sommer, B. Loschko, A. Schell and A. Docter, in *Handbook of Fuel Cells - Fundamentals Technology and Applications*, W. Vielstich, A. Lamm and H. A. Gasteiger, Editors, p. 693, John Wiley & Sons Ltd, West Sussex (2004).

113. D. A. Masten and A. D. Bosco, in *Handbook of Fuel Cells - Fundamentals Technology and Applications*, W. Vielstich, A. Lamm and H. A. Gasteiger, Editors, p. 714, John Wiley & Sons Ltd, West Sussex (2004).

114. S. Motupally, A. J. Becker and J. W. Weidner, *J. Electrochem. Soc.,* 147, 9 (2000).

115. P. W. Majsztrik, *Mechanical and transport properties of Nafion for PEM fuel cells; Temperature and hydration effects,* Ph.D. Dissertation, Princeton University (2008).

116. K. Hisatake, S. Tanaka and Y. Aizawa, *J. Appl. Phys.,* 73, 11 (1993).

117. K. Hisatake, M. Fukuda, J. Kimura, M. Maeda and Y. Fukuda, *J. Appl. Phys.,* 77, 12 (1995).

118. R. W. Hyland and A. Wexler, *ASHRAE Transactions,* 89, pt 2A 2B500 (1983).

119. Vaisala Oyi, User's Guide Vaisala HUMICAP Temperature and Humidity Transmitter Series HMT330 (2009).

120. F. N. Buchi, A. Marek and G. G. Scherer, *J. Electrochem. Soc.,* 142, 6 (1995).

121. *1994 Annual book of ASTM standards*, p. 696, ASTM, Philadelphia (1994).

122. C. E. Evans, R. D. Noble, S. Nazeri-Thompson, B. Nazeri and C. A. Koval, *J. Membr. Sci.,* 279, 1-2 (2006).

123. T. Okada, H. Satou, M. Okuno and M. Yuasa, *J. Phys. Chem. B,* 106, 6 (2002).

124. G. Job and H. Herrmann, *Eur. J. Phys.,* 27 (2006).

125. H. A. J. Oonk and M. T. Calvet, *Equilibrium between phases of matter*, p. 77, Springer Netherlands (2008).

126. C. W. Monroe, T. Romero, W. Mérida and M. Eikerling, *J. Membr. Sci.,* 324, 1-2 (2008).

127. M. Eikerling, A. A. Kornyshev and A. R. Kucernak, *Phys. Today,* 59, 10 (2006).

128. S. Kato, K. Nagahama, H. Noritomi and H. Asai, *J. Membr. Sci.,* 72, 1 (1992).

129. C. J. Orme and F. F. Stewart, *J. Membr. Sci.,* 326, 2 (2009).

130. M. Thomas, M. Escoubes, P. Esnault and M. Pineri, *J. Membr. Sci.,* 46, 1 (1989).

131. E. Bode, M. Busse and K. Ruthenberg, *J. Membr. Sci.,* 77, 1 (1993).

132. N. Kubo, *Study on Performance Improvement of Polymer Electrolyte Fuel Cell for Automobile Application,* Ph.D. Dissertation, Waseda University (2006).

133. N. Takimoto, L. Wu, A. Ohira, Y. Takeoka and M. Rikukawa, *Polymer,* 50, 2 (2009).

134. Q. F. Li, R. H. He, J. O. Jensen and N. J. Bjerrum, *Chem, Mater.,* 15, 26 (2003).

135. C. Yang, P. Costamagna, S. Srinivasan, J. Benziger and A. B. Bocarsly, *J.Power Sources,* 103, 1 (2001).

136. Q. Wang, M. Eikerling, D. Song and Z. S. Liu, *J. Electrochem. Soc.,* 154, 6 (2007).

137. D. Song, Q. Wang, Z. Liu, T. Navessin, M. Eikerling and S. Holdcroft, *J. Power Sources,* 126, 1-2 (2004).

138. M. Secanell, K. Karan, A. Suleman and N. Djilali, *Electrochim. Acta,* 52, 22 (2007).

139. J. J. Baschuk and X. Li, *J. Power Sources,* 86, 1-2 (2000).

140. J. J. Baschuk and X. Li, *Appl. Energy,* 86, 2 (2009).

141. M. V. Williams, E. Begg, L. Bonville, H. R. Kunz and J. M. Fenton, *J. Electrochem. Soc.,* 151, 8 (2004).

142. K. Sato, A. Ohma, K. Yamaguchi and K. Shinohara, *ECS Trans.,* 19, 17 (2009).

143. K. Sato, A. Ohma, K. Yamaguchi and K. Shinohara, *ECS Trans.,* 25, 1 (2009).

144. T. Mashio, A. Ohma, S. Yamamoto and K. Shinohara, *ECS Trans.,* 11, 1 (2007).

145. T. Mashio, A. Ohma and K. Shinohara, *ECS Trans.,* 16, 2 (2008).

146. E. Aleksandrova, R. Heisgen, K. Andreas Friedrich and E. Roduner, *Phys. Chem. Chem. Phys.,* 9 (2007).

147. D. A. Bussian, J. R. O'Dea, H. Metiu and S. K. Buratto, *Nano Lett.,* 7, 2 (2007).

148. X. Xie, O. Kwon, D. Zhu, T. V. Nguyen and G. Lin, *J. Phys. Chem. B,* 111, 22 (2007).

149. J. T. Hinatsu, M. Mizuhata and H. Takenaka, *J. Electrochem. Soc.,* 141, 6 (1994).

150. T. Soboleva, X. Zhao, K. Malek, Z. Xie, T. Navessin and S. Holdcroft, ACS *Appl. Mater. Interfaces,* 2, 2 (2010).

151. M. H. Eikerling and K. Malek, in *Proton Exchange Membranes Fuel Cells-Materials properties and performance*, D. P. Wilkinson, J. Zhang, R. Hui, J. Fergus and X. Li, Editors, p. 343, CRC press, Boca Raton, FL (2009).

152. T. V. Nguyen and R. E. White, *J. Electrochem. Soc.,* 140, 8 (1993).

153. T. F. Fuller and J. Newman, *J. Electrochem. Soc.,* 139, 5 (1992).

154. T. Okada, *J. Electroanal. Chem.,* 465, 1 (1999).

155. P. Berg, K. Promislow, J. St. Pierre, J. Stumper and B. Wetton, *J. Electrochem. Soc.,* 151, 3 (2004).